2014

Meso-Scale Analysis of Deformation Induced Heating in Granular Metalized Explosives by Piston Supported Waves

Sunada Srinath Nagamani Chakravarthy
Louisiana State University and Agricultural and Mechanical College

MESO-SCALE ANALYSIS OF DEFORMATION INDUCED HEATING IN GRANULAR METALIZED EXPLOSIVES BY PISTON SUPPORTED WAVES

A Dissertation

Submitted to the Graduate Faculty of the
Louisiana State University and
Agricultural and Mechanical College
in partial fulfillment of the
requirements for the degree of
Doctor of Philosophy

in

Mechanical Engineering

by
Sunada SN Chakravarthy
Bachelor of Engineering, Visvesvaraya Technological University, 2007
December 2014

ACKNOWLEDGMENTS

I would first like to thank my graduate advisor, Dr. Keith A. Gonthier for his guidance and assistance during my academic career. This work would not have been possible without his constant support. I would also like to thank my committee members Dr. Michael J. Martin, Dr. Ingmar Schoegl, and Dr. Ramachandran Vaidyanathan for their critiques and suggestions. I thank the U.S. Defense Threat Reduction Agency (DTRA), and U.S. Air Force Research Laboratory (AFRL/RWME) for their financial support. I would also like to acknowledge LSU High Performance Computing (HPC) and LONI for providing high-performance computational resources without which this research would have been impossible. I would also like to thank my labmates: Michael Crochet, Rohan Panchadhara, Anirban Mandal, Pratap Rao, John Gilbert, and Mark Fry for all the discussions we had over the years on various topics both technical and otherwise. Finally, I would like to thank my family and friends who have been a constant source of support for me throughout the graduate school journey.

TABLE OF CONTENTS

LIST OF TABLES

LIST OF FIGURES

ABSTRACT

Shock sensitivity of heterogeneous explosive composites is dependent on the formation of hot-spots which are small regions of elevated temperatures within the material. Changes in the initial meso-structure (i.e. packing density, composition, particle size and shapes) of the explosives can significantly alter the hot-spot fields in the material and thereby affect its shock sensitivity. In this study, an explicit, 2D, Lagrangian finite and discrete element technique is used to numerically simulate the deformation induced heating of granular mixtures of explosive (HMX), and metal (Al) particles due to piston supported uniaxial deformation waves ($400 \leq U_p \leq 800$ m/s). A number of simulations are performed by systematically varying the effective initial packing densities ϕ_s, metal mass fractions λ_m, and particle size distributions. Emphasis is placed on charactering how the inclusion of metal (Al) affects both the effective wave end states (Hugoniots) and the hot-spot fields within the explosive (HMX) component relative to neat HMX. Variations in hot-spot volumetric quantities such as number density and volume fraction are characterized since these quantities can be used in the ignition and growth models to describe macro-scale material sensitivity. Predictions indicate that porosity has a leading order effect on the shock sensitivity of the material due to enhanced dissipation resulting from plastic pore collapse. For a fixed porosity and piston speed, inclusion of metal is found to enhance the effective plasticity in the material due to higher pressures. This leads to larger hot-spots within the metalized formulations. However, due to the high thermal conductivity of the metal, frictional induced hot-spots are suppressed within the material since most of the frictional dissipation at the Al-HMX interfaces is absorbed by the metal. Additionally, hot-spot formation is found to have a highly non-linear dependence on Al particle size with a substantial decrease in hot-spot number density and volume fraction predicted with increasing metal particle size. Meso-structural stochasticity arising due to random seeding of particles, and/or large particle clustering were found to affect the hot-spot statistics minimally.

CHAPTER 1
INTRODUCTION

Solid high explosives (HEs) are widely used in defense related applications. Typically, they are made up of explosive particles held together within a polymeric binder. Due to their high rates of energy release, relative insensitivity to heat, and shock impact, some of the commonly used explosive materials are HMX ($C_4H_8N_8O_8$), RDX ($C_3H_6N_6O_6$), and PETN ($C_5H_8N_4O_{12}$). Historically, metal powders such as aluminum and boron have been added to explosive materials to enhance the post-detonation blast. However, the effect of metal addition on impact/shock sensitivity of granular (or porous) HEs remains fundamentally unclear. Quantifying how the inclusion of metal affects the shock sensitivity of HEs represents a significant part of this research. The HEs are generally manufactured by pressing explosive and metal particles into a high density powder, or by mixing the explosive and metal grains with a polymeric binder to produce a plastic bonded explosive (PBX). Figure 1.1 shows the complex morphology of various conventionally used high explosive crystals.

During reaction, these materials produce high temperature and high pressure gases which can affect combustion rates. Of particular importance is the Deflagration to Detonation Transition (DDT) [33, 53] or Shock to Detonation Transition (SDT) of these materials. Deflagration refers to low speed, low pressure subsonic combustion of the material (0.3-0.5 km/s, 0.1-1 GPa), whereas detonation refers to self sustained supersonic combustion (3-9 km/s, 1-10 GPa). Even mild impact (impact speeds = 50-100 m/s) scenarios that can occur during transportation of these materials can lead to a macro-scale detonation event [72] under proper confinement. Therefore, a fundamental understanding of impact/shock induced heating and the subsequent ignition of energetic solids is essential from a safety perspective.

The solid HEs exhibit shock sensitivity due to their heterogeneous meso-strucure. In granular explosives, applied mechanical loads are transmitted by particle contacts resulting

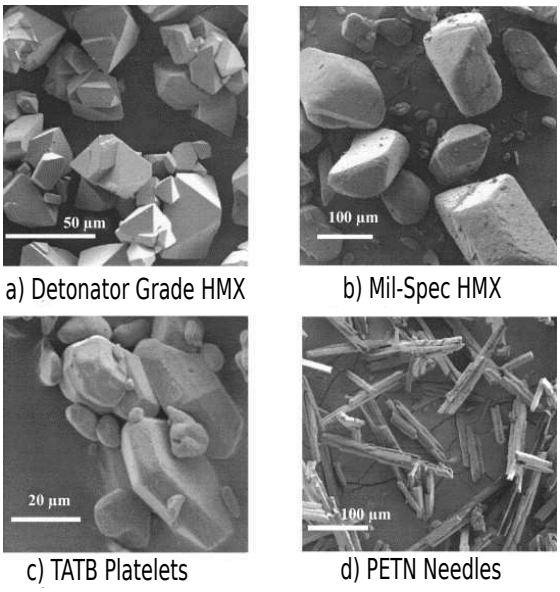

Figure 1.1: Variations in crystal morphology for typical high energetic materials. Reprinted from Thermochimica Acta, Vol. 384/Issues 1-2, M.R.Baer, Modeling heterogeneous energetic materials at the mesoscale, 351-357, 2002, with permission from Elsevier [2]

in highly localized stresses at the contact interfaces. Various dissipative mechanisms associated with stress localization can result in small regions with high temperatures within the explosive particles. These high temperature regions are commonly referred to as *hot-spots*. Hot spots can be sub-particle scale in size (1-10 μm [28]) and can have temperatures which are much higher than the ignition temperature of the material. Some hot-spots have sufficient thermal inertia to overcome conductive and acoustic expansion losses and as such constitute potential ignition sites behind the deformation or shock wave. If the conditions are conducive, these discrete reactive hot-spots can thermally interact, and coalesce into bigger, more intense hot-spots resulting in large amounts of exothermic energy release. The exothermic energy release may further enhance the pressure and temperature of product gases eventually leading to material detonation. Possible dissipative mechanisms for hot-spot formation include plastic deformation [1, 10, 18, 35], fracture [8, 22], frictional sliding [18, 26], shear banding [8], and micro-jetting [52, 54, 79].

Though hot-spots are important in establishing impact/shock sensitivity of HEs, it remains unresolved as to how variations in the initial meso-structure and component thermo-

mechanical properties affect both the bulk deformation wave properties, and the hot-spot fields. Characterizing the effects of the initial meso-structure on the bulk and particle scale thermo-mechanical fields constitutes the main objective of this study. A comprehensive description of a heterogeneous meso-structure is not a trivial task due to the vast number of variables that would be required to formulate a proper mathematical description [78]. In this work, the initial meso-structure is characterized by its effective packing density $\bar{\phi}_s$, effective metal mass fraction λ_m, particle size distributions, and particle shape distributions since experiments have shown significant dependency of explosive shock sensitivity on these parameters [32, 72, 73, 76, 77]. It is important to note that materials with identical effective packing densities, metal mass fraction, particle size and shape distributions, may exhibit different impact/shock response if they have varying spatial fluctuations in these quantities at the particle scale. In principle it is possible to use N-point radial distributions, cluster distribution functions to reasonably characterize material stochasticity [78]. For tractability, the main purpose of this study is to capture only the leading order effects of porosity, composition, particle size, and shape distributions on shock sensitivity of granular explosives. In the remainder of this chapter, relevant literature is reviewed, followed by the problem description and objectives of this study.

1.1 Literature Review

1.1.1 Experimental

In this section, the relevant experiments that highlight the effects of the initial meso-structure on the impact and/or shock sensitivity of HEs are discussed. Here impact sensitivity refers to low-speed impacts ($\approx U_p \leq 200$ m/s), whereas shock sensitivity refers to high speed impacts ($U_p > 200$ m/s). A number of experiments have been performed to investigate the relations between the initial meso-structure and the corresponding shock sensitivity. The section below provides a brief overview of some of the experiments that have investigated the effects of porosity, composition, particle size and shape on material impact/shock sensitivity, as these parameters characterize the changes in the meso-strucutre within the context of our

study. It is important to point out at this juncture, that the main drawbacks of experiments is that they can only resolve the macro-scale features, such as effective wave pressures, temperatures or macro-scale detonation parameters such as time to detonation or run distance to detonation. No experimental technique currently exists that can explicitly resolve the resulting hot-spot fields and correlate the observation to the macro-scale material sensitivity. As such, meso-scale models must be used in conjunction with macro-scale models and experiments to develop a basic understanding of impact/shock sensitivity of heterogeneous HEs.

1.1.2 Effects of Porosity

There are two types of porosity, namely intra and inter-particle porosity. Intra-particle porosity refers to pores within the explosive particles, whereas inter-particle porosity refers to pores between particles. Few systematic studies have been conducted to quantify the effects of each type of porosity [13, 24, 36, 72]. Borne et al. [13] investigated the effects of both intra and inter-particle pores on the shock sensitivity of RS-RDX where RS stands for reduced sensitivity. Their studies indicated that intra-particle pores were more important in establishing shock sensitivity. The reason for this observation was due to the fact that there was very little inter-granular porosity in their materials since they were compacted to theoretical maximum densities of around 99.2%. Gustavsen et al. [36] conducted low pressure shock initiation experiments on porous HMX with packing densities of 65% and 73%. Their experiments indicated higher density material to be less sensitive to shock loading. Most experiments indicate that an increase in porosity typically leads to an increase in shock sensitivity of the explosive [72]. The observed positive correlation between porosity and sensitivity is because of complicated dissipative processes such as viscoplastic pore collapse that result in an increased formation of reactive hot-spots within the material. It is possible that materials with the same effective porosity may exhibit different variations in impact/shock sensitivity due to variations in the pore size distributions. Controlling the pore size distribution within materials is impossible, and therefore meso-scale models such as the

one considered in this study, can be used to investigate the effects of stochastic fluctuations in porosity within materials on its impact/shock sensitivity.

1.1.3 Effects of Composition

Historically, metals such as aluminum and boron have been used in explosive formulations to enhance the post-detonation blast effect. However, very little literature exists on how the inclusion of metal particles can affect the shock sensitivity of the explosive mixture. There are two primary features of metal inclusion that most of the experiments have tried to address. First, the amount of metal content within the explosive mixture and its effect on the macro-scale detonation response. Second, the effects of metal particle size on shock sensitivity of the material. Studies performed by Price and Clairmont [65] showed that increasing the Al content slowed down the DDT process in HMX-Al mixtures, and that fine Al (5 μm) was more effective in delaying DDT than coarse aluminum (95 μm). Other experiments have also shown that an increase in Al content decreases the detonation velocity due to compressive work performed on the metal grains [32]. Nano aluminum particles have been theorized to provide better post-detonation blast performance due to their larger surface area to volume ratio. Shock sensitivity experiments performed by Teselkin [77] showed that HMX explosive composites with nano aluminum particles were more sensitive compared to formulations containing micron sized aluminum particles. Teselkin postulated that the increase in sensitivity is due to additional heat release by nano aluminum particles during chemical interaction of components at mechanically induced hot-spots. However, other experiments measuring the performance of such mixtures have been inconclusive [14, 47]. Most of these experiments have looked at the shock sensitivity of metalized explosives at high shock pressures of over 10 GPa. However, to our knowledge, little experimental effort has been made to investigate sensitivity of aluminized HMX for relatively weaker shock waves of $P \leq 5$ GPa associated with low speed impacts ($U_p \leq 800$ m/s) which could also result in material detonation. In this study, meso-scale models are used to predict the impact sensitivity of metalized explosives for relatively weaker shock waves of $P < 5$ GPa.

As mentioned earlier, under proper confinement even mild impacts $U_p \leq 100$ m/s, may lead to detonation.

1.1.4 Effects of Particle Size and Shape

Numerous experiments have explored the effects of particle size on shock sensitivity [19, 57, 64, 66, 67, 70, 73, 76]. Taylor and Ervin [76] found for pressed TNT samples with similar porosity, coarse particles showed enhanced sensitivity at low pressures, while fine particles were more sensitive at high pressures due to rapid post-ignition reaction in these particles because of their larger burn surface area. Song et al. [73] performed small scale drop weight tests (impact sensitivity) on porous HMX samples with varying particle sizes and shapes. The authors concluded the HMX sensitivity was not just a function of the particle size but also the particle shape. While a monotonic decrease in impact sensitivity was observed with an increase in average particle size for needle, and spherical shaped HMX particles, a non-monotonic variation in sensitivity with particle size was observed for polyhedron shaped HMX particles. However, little physical justification was given for the observed effects. Gustavsen et al. [36], found that reaction initiated in coarse HMX particles ($\approx$150 μm) at pressures as low as 0.5 GPa (impact sensitivity), whereas the finer HMX particles ($\approx$ 10 μm) did not react below pressures of 0.9 GPa (shock sensitivity). They speculated that coarse HMX particles had a lower initiation threshold since the hot-spot size and temperature were larger. Though particle sizes have been found to affect material sensitivity, a fundamental understanding of the effects of particle size and shape on hot-spot fields is required to explain the macro-scale material response.

1.1.5 Theoretical and Computational Work

Researchers have taken different modeling approaches such as, macro-scale and meso-scale models to investigate deformation induced heating in HEs due to vastly different length and time scales involved in describing the impact response. Macro-scale models have conventionally been used to model engineering scale systems that consist of a large number of particles (10^{10} $particles/m^3$). These models are computationally inexpensive, and can

provide predictions that can be validated against experiments. However, by construction the bulk models are cast in terms of spatially averaged variables, and therefore cannot account for dissipation occurring at particle scales (hot-spots) which are important for combustion initiation. This modeling deficiency has motivated energy localization strategies to implicitly account for the effects of hot-spots within the context of macro-scale models [4, 15, 41] though these methods have only been marginally succesful in predicting experimentally observed detonation parameters. Baer and Nunziato [4] developed a widely used two-phase mixture theory for explosive DDT modeling. The two phase approach is based on principles of phase separation, where the thermodynamic properties of each phase are assumed to be independent of the others. The interaction between each phase is accounted for by source terms which describe mass, momentum and energy transfer between the phases. Bdzil et al. [9] extended the two phase model developed by Baer and Nunziato to account for more physically appropriate forms of interphase source terms in order to better predict the energy associated with dynamic compaction. Recently, Gonthier and Rumchik [34], and Crochet and Gonthier [23] have extended the two phase mixture theory initially formulated by [4] and later improved by [9] to account for an arbitrary number of solid phases, and a gas phase. One of the main drawbacks of these multiphase macro-scale models lies in the specification of source terms which are non-unique. Additionally, since the multiphase modeling approach is based on principles of phase separation, these models require experiments to provide phase-specific information to calibrate their empirical constants. However, for explosive mixtures containing multiple phases, no robust experimental technique currently exists that can provide phase-specific information to compute the parameter values in each phase. In this case, meso-scale models predictions can help guide the development of the macro-scale constitutive models by providing information on phase-specific quantities.

Due to the shortcomings of bulk models in describing particle scale fluctuations, mesoscale models have been used to provide detailed descriptions of the DDT process in porous explosives [2, 5, 27]. Several meso-scale models have tried to address the inert impact response of

HEs with an emphasis on characterizing various dissipative mechanisms that lead to the formation of hot-spots [8, 10, 61, 62]. Only a brief description of the relevant meso-scale models is provided here since a comprehensive discussion can be found in [61]. Though meso-scale models are computationally expensive, advancements in computing have enabled the study of large scale systems involving thousands of particles. Several computational techniques such as Eulerian hydrocodes [2, 11, 12, 45], Lagrangian FEM codes [8, 61, 62], and smooth particle hydrodynamics (SPH) [48, 56], have been used to describe compaction of granular materials at the particle scale. Each modeling approach has its own advantages and disadvantages. For example Eulerian schemes can account for much larger material deformation compared to Lagrangian models wherein large deformation of particles typically leads to mesh-distortion issues. However, unlike Lagrangian techniques, Eulerian techniques require more complex algorithms such as level-set techniques to accurately describe the particle boundaries in time, which can lead to numerical instabilities and an increase in computational time.

Menikoff et al. [54] used a 2D Eulerian code to investigate deformation induced heating in granular HMX by simulating piston driven compaction waves. The predictions from this work suggested that viscoplasticity may be an important heating mechanism in granular HMX. Panchadhara and Gonthier [61, 62] developed a combined finite element-discrete element technique to model inert impact/shock response of granular HMX. The study addressed quasi-steady uniaxial deformation waves in large particle ensembles (2000-4000 particles). The key focus of this work was to characterize the relative importance of viscoplastic and frictional dissipation as hot-spot formation mechanisms. Their analysis indicated that visoplastic dissipation affected bulk temperature rise in the material, but frictional heating was responsible for high intensity hot-spots with temperatures in the range of 800-1500 K. However, the study was limited to a single mesostructure and a single component (Neat HMX). Additionally, in their study, the resulting hot-spot fields were not characterized in detail to obtain relevant hot-spot properties such as size, intensity, shape, and proximity, all of which may be important in establishing material sensitivity. Recently, Barua et al. [6, 8]

have employed a cohesive finite element method (CFEM) to model particle scale response of PBX and granular HMX. The CFEM allows for efficient modeling of fracture and frictional dissipation along the failed surface. Their studies showed that viscoelastic dissipation of the binder, and frictional heating along the fractured surface were the primary mechanisms for hot-spot formation. Most of meso-scale models have addressed issues concerning the impact/shock sensitivity of PBX compositions consisting of an explosive such as HMX embedded in a polymeric binder, or of a single granular component (HMX). To our knowledge no meso-scale model has tried to explore the impact/shock sensitivity of metalized explosives.

1.1.6 Reactive Models

Historically, reactive burn models have been employed to investigate shock sensitivity of explosives. Most of the reactive burn models contain many free parameters that can be varied to fit experimentally observed detonation parameters such as velocity of detonation, run distance to detonation or time to detonation. Reactive models that account for hot-spot formation and the subsequent reaction and growth of these hot-spots have been observed to predict experimentally obtained detonation parameters well [38, 46, 55]. Models developed by Mader and Forest [50] and Lee and Tarver [46] are the most common empirical models in use. Lee and Tarver modeled shock initiation of explosives by assuming that a small fraction of the explosive is ignited by the passage of the shock front, and that the reaction rate is primarily controlled by the pressure within the material, and the surface area of the hot-spots. Their model was able to reasonably predict run to detonation for a variety of commonly used explosives. Menikoff and Shaw [55] argued that the burn rate of ignition and growth models should incorporate three meso-scale features namely: (1) the density of reactive hot-spots; (2) the growth of these reactive hot-spots which are dependent on the local deflagration speeds; (3) the proximity of these burn centers that allow for the overlap of the deflagration wavelets from the neighboring burn centers. More detailed ignition models have been employed to describe various hot-spot formation mechanisms [38, 41, 43, 49]. Khasainov et al. [43] suggested viscoplastic pore collapse to be the primary mechanism responsible

for the formation of hot-spots. Similar predictions have also been made by Kang et al. [41]. Massoni et al. [52] introduced a mechanistic model to couple the microscopic hot-spot formation mechanism with bulk DDT phenomena. Several other models have been suggested to account for dissipative mechanisms other than viscoplasticity [29, 44]. Depending on the type of external stimuli, different dissipative mechanisms can play a dominate role in establishing the sensitivity of the explosive material. Therefore, recently, Horie and Hamate [38] incorporated a wide variety of hot-spot formation mechanisms into modeling shock initiation in HEs. Their model assumes exponential hot-spot size distributions based on the distributions of stress fields in the material. However, it is highly improbable that the stress fields are always exponentially distributed within the meso-structures. Additionally, the Horie and Hamate model does not account for the effects of hot-spot temperatures, which are also significantly important in establishing the shock sensitivity of explosives. Tarver et al. [75] have tried to address this issue by providing a thermal explosion manifold based on the combination of hot-spot size and temperature. However, their analysis was restricted to ideal hot-spot shapes such as cylindrical, spherical and planar with uniform hot-spot temperatures. In reality hot-spot shapes and the temperature distributions within hot-spots are rather complex. From the discussions above, it is clear that most of these models use simple hot-spot descriptions to describe the ignition and growth process because they do not account for the effects of the initial meso-structure on the hot-spot fields. Therefore, their application is rather limited to materials which have hot-spot distributions which are similar to their assumed form. As such, much of the discussion in this dissertation is devoted to describing the statistical distribution of various hot-spot features and their dependency on the initial meso-structure. It is plausible that the predicted hot-spot distributions from meso-scale simulations can be incorporated in the ignition and growth models to better predict the macro-scale material sensitivity.

Shock sensitivity of HEs is an inherently stochastic process due to variations in the material morphology. Materials with similar macro-scale packing density, composition, particle

size and shape distributions can exhibit different impact/shock sensitivity due to variations in the meso-structure. Therefore, a number of studies [3, 20, 39, 60] have tried to use probabilistic models to explain shock sensitivity of explosives. Nichols and Tarver, developed a probabilistic reactive flow model based on the number density of potential reactive hot-spot sites. Their model was able to reasonably replicate the detonation times for HMX-based PBX. Though their model incorporated the effects of both hot-spot size and intensity on reaction rates, the hot-spot shape distributions were assumed to be spherical. Barua et al. [7], performed a detailed computational study to characterize the effects of material stochasticity on the impact sensitivity of an HMX based PBX by creating a number of statistically similar materials. In their analysis, the authors observed that variations in time to criticality (time for the material to initiate) followed a Weibull distribution. However, their analysis was limited to a narrow range of piston speeds $100 \leq U_p \leq 250$. Gilbert et al. [31] provided a methodology to statistically characterize hot-spot fields obtained from inert meso-scale simulations for granular HMX. In their analysis, probability density functions (PDFs) were used to characterize hot-spot morphology (size and shape), intensity, and spatial proximity. However, the analysis was restricted to just a single component (HMX) with similar particle sizes and a narrow range of piston speeds (300-500 m/s). In this study, the analysis by Gilbert et al. is extended to account for effects of metal on HMX hot-spots fields. Additionally our study also tries to address the effects of particle size on the inert hot-spot fields since most explosive materials exhibit sensitivity to variations in particle size.

1.2 Problem Description

The primary focus of this study is to computationally characterize the deformation induced heating of granular HEs by piston supported uniaxial deformation waves at various spatial and temporal scales as shown in Figure 1.2. In this work, the original model formulated by Panchadhara and Gonthier [61] for a single explosive component (HMX) is extended to account for metal (Al) and explosive (HMX) components. The choice of aluminum and HMX as two components of the explosive mixture is motivated by the fact that these are

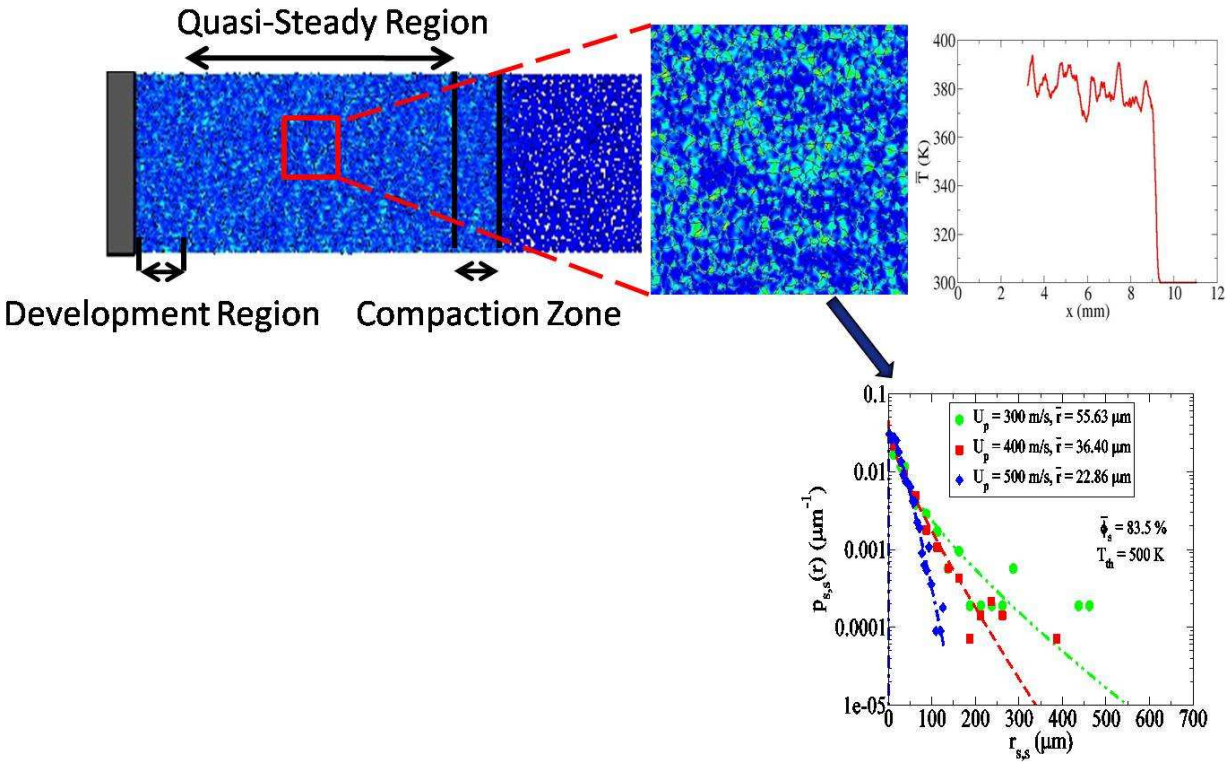

Figure 1.2: Schematic of the deformation induced heating in granular HEs due to piston supported uniaxial waves at various length scales.

commonly used materials within the energetics community due to their high energy output. Further, the analysis performed by Panchadhara and Gonthier was restricted to a fixed meso-structure with an initial packing density of $\bar{\phi}_s = 83.5\%$, and a uniform particle size distribution with a narrow range of particle sizes (r = 20-40 μm). In this study, a more comprehensive analysis of the effects of the initial meso-structure on shock sensitivity of HEs is performed by varying the effective packing density, composition, particle size significantly. Only minor variations in particle shape (hexagonal or circular) were considered. Because the modeling approach is similar to the one performed by Panchadhara and Gonthier, only a brief description of the modeling assumptions are summarized here, and a comprehensive discussion can be found in their work [61].

As seen in Figure 1.1, a real micro-structure consists of particles with complex geometries, packing arrangements and intra-particle defects. However, for simplicity, ideal particle shapes (circular and hexagonal) are considered in this study, and intra-particle defects are

ignored. Also, the effects of soft binder material are ignored since the harder explosive particles typically carry much of the load when subjected to impact for meso-structures with high packing densities such as the ones considered in this study. Accurate descriptions of deformation heating require that temperature dependent material properties be used. However, using temperature dependent properties can result in a stiff system of non-linear equations which can lead to numerical instabilities. Therefore, for simplicity, temperature independent properties are used throughout our simulations. Though the resulting temperatures may be larger than the melting temperature of HMX (T_{melt} = 520 K), melting and phase change are ignored. In reality, melting may suppress the magnitude of hot-spot temperatures. Such a problem if properly posed would be difficult to computationally solve over large particle ensembles (4000 particles) used in this study due to numerical stiffness. Further, the analysis is restricted to 2-D plane strain conditions. The 2-D assumption can affect the results since greater stress concentration and frictional dissipation might arise in 3-D particle ensembles due to different packing arrangements. For example, for equally sized circular particles, a face centered cubic packing in 2-D results in a maximum of 6 contacts per particle, whereas 3-D spherical particles may have 12 contacts per particle plausibly leading to higher dissipation. The study ignores combustion, since the main focus here is to characterize the bulk and particle scale fluctuations that might create regions within the material where combustion is likely to begin. Though fracture may be an important dissipative mechanism as suggested by [8], its effects are not considered in this study for simplicity.

Several other simplifications are made in this analysis. Interstitial gas might significantly affect the DDT of HEs, however the void space between particles (inter-particle voids) are assumed to be massless. This is a reasonable assumption since in the absence of combustion, interstitial gas plays a secondary role in determining the impact response. Though large strain rates can lead to significant strain hardening in the materials, perfect plasticity is assumed in this analysis. A rate dependent Von Mises yield criterion with a temperature independent yield surface is used to describe material plasticity. With all the assumptions, the

model still enables us to capture leading order effects of visco-plastic and friction dissipation as potential hot-spot formation mechanisms.

Figure 1.3 shows the schematic of the problem addressed in this study. A rigid planar piston having a constant speed U_p impacts an initially stress-free granular HE. The motion of the piston drives a stress wave (inter-particle contacts) referred to as the deformation/compaction wave into the HE with an initial transience in the material response close to the piston surface followed by a quasi-steady uniaxial deformation wave having a speed D within the material. Most of the dissipation that results in the formation of hot-spots occurs within the deformation wave referred to as the compaction zone. Typically the thickness of the deformation wave reduces with an increase in U_p. The computational domain is chosen so that reasonably well-resolved simulations can be performed within a short amount of time while being sufficiently large enough to enable development of quasi-steady deformation waves. Quasi-steady deformation waves form during sustained loading conditions which occur in many practical situations, and therefore, this work is dedicated to exploring material sensitivity due to sustained loading.

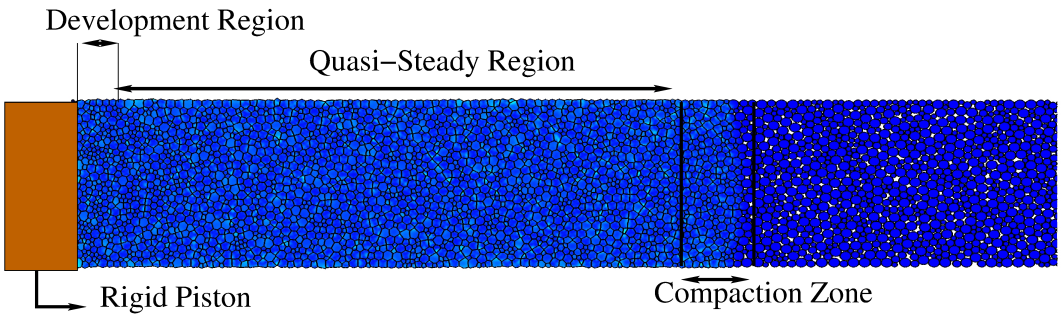

Figure 1.3: Schematic of the computational problem addressed in this study.

1.3 Objectives

The main focus of this study is to quantify the effects of the initial meso-structure on the shock heating of granular HEs. As mentioned, by initial meso-structure, we refer to variations in packing density ϕ_s or porosity $1 - \phi_s$, composition λ_m, and particle size and

shape. Emphasis is placed on characterizing the effects of Al on both the bulk and particle-scale (hot-spots) thermo-mechanical fields. Specific objectives of the study include:

1. Characterize the effects of porosity and composition on spatial wave structures and hot-spot fields.

Packing density and metal mass fraction are varied between $0.68 \leq \bar{\phi}_s \leq 0.83$, and $0.0 \leq \lambda_m \leq 0.2$ respectively. Quasi 1D spatial wave profiles are obtained by transverse averaging the particle scale thermo-mechanical fields over suitable averaging volumes. Importance is placed on obtaining phase/component specific averages for HMX and Al in metalized explosive formulations. Since hot-spots are important in establishing impact/shock sensitivity of HEs variations in hot-spot fields due to changes in porosity and composition are investigated. Emphasis is placed on identifying how inclusion of metal affects the explosive component hot-spot field since the ignition is likely to begin within the explosive particle. Hot-spot number densities, size, shape, intensity and proximity distributions may be used to estimate parameter values in ignition and growth models that are routinely used to model detonation in a variety of HEs. As such a detailed methodology is outlined to statistically characterize the variations in hot-spot fields with changes in porosity and/or composition.

2. To study the effects of component particle size ratios and distributions on shock sensitivity.

Numerous experiments have indicated that component particle sizes, and their corresponding size distributions are important in determining the impact/shock sensitivity of the HEs. To this end, meso-structures consisting of different component particle size ratios and size distributions (uniform, and bimodal) are considered. The initial packing densities between the meso-structures varies minimally ($0.83 \leq \phi_s \leq 0.86$), and metal fractions are varied between $0.0 \leq \lambda_m \leq 0.56$. Effects of the metal (Al) particle size on explosive component heating are investigated.

3. To investigate the effect of material stochasticity on shock sensitivity.

Random variations in the initial particle morphology (shape and size), and component distribution can make the shock sensitivity of granular HEs inherently stochastic. Explosive materials with similar macro-scopic properties such as effective packing density, composition, particle size and shape distributions can exhibit different sensitivity to impact/shock. Therefore, emphasis is placed on quantifying the effects of material stochasticity on the bulk wave profiles (Hugoniots) and the hot-spot fields by creating a set of 10 meso-structures with similar effective packing density, but varying spatial fluctuations about the effective value.

The outline of the dissertation is as follows. Chapter 2 discusses the mathematical model used to describe the impact response of granular HE, including a brief description of the finite deformation theory, and the relevant initial and boundary conditions. The combined FEM-DEM method employed to numerically solve the multi-particle impact problem is discussed in Chapter 3. In this chapter, the discrete/weak formulation of the governing equations is presented, and a discussion of the penalty based approach which is used to estimate the external forces arising due to particle contact is provided. Chapter 4 gives predictions for the variations in spatial wave structure and hot-spot fields due to changes in the initial packing density $\bar{\phi}_s$ and composition λ_m. Chapter 5 highlights the effects of particle size on hot-spot fields by performing impact studies on meso-structures consisting of different component size ratios and particle size distributions (uniform and bimodal). Material stochasticity effects are considered in Chapter 6 by varying the spatial fluctuations in porosity for meso-structures consisting of similar effective packing densities, composition, particle size and shape. Finally conclusions and recommendations are discussed in Chapter 7.

CHAPTER 2
MATHEMATICAL MODELING

In this study, the deformation induced heating of granular explosive is modeled as a multi-particle contact problem, where the contact constraints of each particle Ω is formulated as an initial-boundary-value problem (IBVP) for the displacement u and temperature T field, which are described by mass, momentum, and energy conservation equations. The summary of the chapter is as follows, First, the governing equations for mass, momentum, and energy are presented, followed by a brief discussion on the finite deformation theory. Second, the thermo-hyperelastic viscoplastic constitutive relations that are used to close the system of equations are discussed. Finally, the relevant initial and boundary conditions are summarized. A comprehensive discussion on the mathematical model can be found in [61] and only the most relevant aspects of the model are presented here for brevity.

The evolution equations for mass, momentum, and energy are given by

$$\oint_{\Omega} \rho dv = 0, \tag{2.1}$$

$$\rho \frac{dv}{dt} = \nabla \cdot \sigma, \tag{2.2}$$

$$\rho C_v \frac{dT}{dt} = \sigma : d - \nabla \cdot q. \tag{2.3}$$

Here ρ corresponds to the density of the particle, σ is the Cauchy stress tensor, ∇_x is the spatial gradient operation, d is the Eulerian deformation rate tensor, q is the heat flux, and C_v is the specific heat at constant volume. In this study, the effects of body forces are neglected since they have negligible influence on compaction dynamics compared to deformation induced forces. The Eulerian deformation rate tensor d in Eq. 2.3 is given by

$$d = \frac{1}{2}(\nabla_x v + (\nabla_x v)^T), \tag{2.4}$$

where v corresponds to the velocity of the particle, and T denotes the transpose operation. In addition to satisfying the conservation laws, each particle also has to satisfy the second law of thermodynamics. The second law is expressed by the local Clausius-Duhem inequality as

$$\rho\frac{d\eta}{dt} - T^{-1}(\rho r - \nabla_x \cdot q) + q \cdot \nabla_x T^{-1} \geq 0, \tag{2.5}$$

where η is the entropy density.

2.1 Finite Deformation Theory

High speed impact problems ($U_p \geq 100$ m/s) considered in this study result in large strains $O \approx (10^{-2}\text{-}10^{0})$ and strain rates $O \approx 10^{6}\ s^{-1}$. Therefore a linear description of stress-strain behavior does not provide accurate predictions; therefore, a finite deformation theory is required. For a particle Ω, relevant properties such as density, stress, and strain can be described in terms of *material/initial* configuration Ω_o or in terms of *spatial/current* configuration Ω_t. Here, material configuration corresponds to the locations of material points within the particle before deformation, whereas current configuration corresponds to locations of material points within the particle during deformation. The coordinates of material points in the initial configuration are given by X whereas its current position is prescribed by x. An important quantity in this theory is the deformation gradient tensor F which relates the relative positions of two points before and after deformation. The deformation gradient is mathematically defined as $F = 1 + \nabla_0 u$, where 1 is the second order unit tensor. Here, u is defined as

$$u(X,t) = x - X. \tag{2.6}$$

The determinant of the deformation gradient, $J = det[F]$ gives the total volumetric deformation of the material. Hence, if the initial density of the particle is given as ρ_o, then the density after deformation is given by $\rho = \rho_o/J$. Like any second order tensor, F can be expressed as a product of two second order tensor $F = RU = VR$, where R is an

orthogonal rotation tensor, and U and V are positive symmetric right and left stretch tensors respectively. Though not illustrated here for brevity, it can be shown that $V = R.U.R^T$ so that U and V have the same eigenvalues (principal stretches), but different principal directions (eigenvectors) N_i and n_i respectively. This polar decomposition of F is unique since F is non-symmetric.

Further, F can be expressed as a product of elastic and plastic components $F = F_e F_p$, where the plastic component F_p leads to a stress free intermediate configuration Ω_{int}, and the elastic component F_e deforms this configuration into the current configuration Ω_t based on equilibrium constraints. The decomposition process of the deformation gradient tensor is illustrated in Figure 2.1. It is important to note that the deformation gradients F_e and

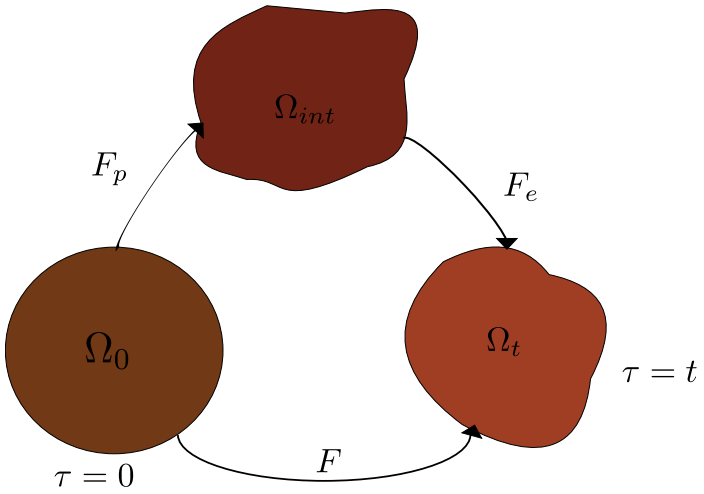

Figure 2.1: Schematic for multiplicative decomposition of deformation gradient tensor.

F_p are not uniquely defined. However, in this study the intermediate configuration is fixed by requiring that the inelastic deformation have the same principal directions as the elastic deformation. This is a reasonable assumptions for isotropic materials, and details regarding this simplification can be found in [61]. Conventionally, rotation independent deformation tensors are used in solid mechanics because pure rotation should not result in any stress within the material. Commonly, right and left Cauchy-Green deformation tensors are used to describe the rotation-independent deformation of the material. The elastic left Cauchy-

Green tensor and plastic right Cauchy-Green tensor are defined as

$$b_e = F_e F_e^T = \sum_{i=1}^{3} (\lambda_{e,i}^2) n_i \otimes n_i, \qquad C_p = F_p^T F_p = \sum_{i=1}^{3} (\lambda_{p,i}^2) N_i \otimes N_i, \tag{2.7}$$

where $\lambda_{e,i}^2$, and $\lambda_{p,i}^2$ are the eigenvalues of b_e and C_p; and n_i and N_i are the corresponding eigenvectors.

Stress in finite deformation theory can be described in current configuration using the Cauchy stress tensor σ. However, the second Piola-Kirchhoff stress tensor S is used to represent the force per unit area in the initial configuration. It is related to the Cauchy stress tensor as $S = JF^{-1}\sigma F^{-T}$. It is convenient to define another stress tensor in the current configuration which is the Kirchhoff stress tensor $\tau = J\sigma$. The Kirchhoff stress tensor is related to to second Piola-Kirchhoff tensor as $\tau = \phi_*[S]$, where for a material object such as S, the operation $\phi_*[S] = F^{-T}SF^{-1}$ represents a push forward of S from the initial configuration to the current configuration. The push forward and pull back operations are frequently used to move between the current and initial configuration.

2.2 Hyperelasticity

Hyperelastic formulation of the stress strain relationship is based on estimating stress from the Helmholtz free energy density ψ using strain. For brevity only key aspects of the formulation are discussed in this section, and a comprehensive discussion can be found in [59]. In finite strain hyperthermoelastic-viscoplasticity, ψ is defined as a function of the state variables b_e, effective plastic strain ϵ_p, temperature T, and it can be expressed in terms of u and η using Maxwell relation:

$$\psi(b_e, \epsilon_p, T) = u - T\eta, \tag{2.8}$$

where the entropy density is given by $\eta = -\frac{\partial \psi}{\partial T}$. Using the above equation, the time derivative of ψ can be expressed as

$$\dot{\psi} = \dot{u} - T\dot{\eta} - \eta\dot{T}, \tag{2.9}$$

where a *dot* above the variable represents the time derivative. Further, by applying the chain rule, the time derivative of ψ can be written as

$$\dot{\psi} = \frac{\partial \psi}{\partial b_e}\dot{b}_e + \frac{\partial \psi}{\partial T}\dot{T} + \frac{\partial \psi}{\partial \epsilon_p}\dot{\epsilon}_p. \tag{2.10}$$

A more restrictive form can be derived for the entropy inequality in Eq. 2.5 by replacing the terms within the parenthesis using Eq. 2.3, and by recognizing that $q.\nabla_x T^{-1} \geq 0$ which leads to

$$D = \rho T\dot{\eta} + \sigma : d - \rho\dot{u} \geq 0, \tag{2.11}$$

where D is the total dissipation. Substituting for $\dot{u}$ in Eq. 2.11 using Eq. 2.9, and using Eq. 2.10 for $\dot{\psi}$ gives the total dissipation as

$$D = (\sigma - 2\rho\frac{\partial \psi}{\partial b_e}b_e) : d + 2\rho\frac{\partial \psi}{\partial b_e} : d_p - \rho\frac{\partial \psi}{\partial \epsilon_p}\dot{\epsilon}_p \geq 0, \tag{2.12}$$

where d_p is the plastic rate of deformation. For purely elastic process $d_p = 0$, and this gives the constitutive relation for the Cauchy stress tensor as

$$\sigma = 2\rho\frac{\partial \psi}{\partial b_e}b_e. \tag{2.13}$$

Also, assuming that the same constitutive equation is valid for plastic deformation, and substituting it in the dissipation equation gives the final form of second law that is used in this study as

$$D = \sigma : d_p - \rho\frac{\partial \psi}{\partial \epsilon_p}\dot{\epsilon}_p \geq 0. \tag{2.14}$$

In this study the granular particles are modeled as isotropic materials. Therefore, the eigenvectors of the Cauchy stress tensor are collinear with the eigenvectors of b_e. Hence σ can be decomposed as

$$\sigma = \sum_{i=1}^{3}(\sigma_{ii})n_i \otimes n_i, \tag{2.15}$$

where σ_{ii} are the eigenvalues of the Cauchy stress tensor. Similarly, the expression for the Kirchhoff stress tensor can be obtained as

$$\tau = \sum_{i=1}^{3} (\tau_{ii}) n_i \otimes n_i, \tag{2.16}$$

where τ_{ii} are the eigenvalues of τ defined as

$$\tau_{ii} = \frac{\partial \psi}{\partial ln(\lambda_{e,i})}. \tag{2.17}$$

2.3 Plastic Flow

To model plastic deformation of particles, a viscoplastic overshoot model is used to estimate the stress fields within a particle. A Von Mises type yield criterion and an associative flow rule is used to solve for the evolution of plastic variables. Though isotropic hardening is discussed in the model formulation, for simplicity it is not considered in our simulations. Von Mises yield criterion is defined by a temperature independent yield surface ϕ which is a function of τ, and a hardening parameter q

$$\phi(\tau, q) = \sqrt{\bar{\tau} : \bar{\tau}} - \sqrt{\frac{2}{3}}(\tau_o - q) \leq 0, \tag{2.18}$$

where $\bar{\tau}$ is the deviatoric component of Kirchhoff stress, and τ_o is the yield strength of the material. It is important to note that the values of τ, and q that satisfy the yield criterion are not unique. Therefore the principle of maximum plastic dissipation is used, which states that of all the possible values of τ and q that satisfy the yield criteria, optimal values are those which maximize the total dissipation given in Eq. 2.14. This constraint is solved as a constrained minimization problem by using the Lagrangian multiplier procedure. Based on the assumptions listed above, the plastic evolution equations can be written as

$$d_p = \dot{\epsilon} \frac{\bar{\tau}}{\sqrt{\bar{\tau} : \bar{\tau}}}, \quad \dot{\epsilon}_p = \sqrt{\frac{2}{3}} \dot{\epsilon}. \tag{2.19}$$

The Von Mises plastic model is also called the $J2$ plasticity model since it is volume preserving. Therefore, the Kirchhoff stress can be decomposed into purely volumetric and deviatoric components where, p represents the volumetric component (pressure), and the principal deviatoric component is given by $\bar{\tau}_{ii}$. These stress components can be expressed in terms of stored potential energy function $\tilde{\psi} = \rho_0 \psi$ as

$$p = \frac{1}{J}\frac{\partial \tilde{\psi}}{\partial ln(J)}, \qquad \bar{\tau}_{ii} = \frac{\partial \tilde{\psi}}{\partial ln(\lambda_{e,i})}. \tag{2.20}$$

The Perzyna type viscoplastic flow allows for the effective stress defined by

$$\tau_e = \sqrt{\frac{3}{2}\bar{\tau} : \bar{\tau}}, \tag{2.21}$$

to exceed the yield value τ_0. The overstress is defined as $d = \bar{\tau}_e - (\tau_0 - q)$. For Perzyna type overstress model, the effective plastic strain rate is given by $\dot{\epsilon}_p =< d/\gamma >$, where γ is the plastic viscosity parameter, and $< . >$ is the Macaulay bracket.

In this work, a stretch based stored potential is used to model the material response. The assumed form of the potential is given by

$$\tilde{\psi}(\lambda_e, \epsilon_p, T) = \tilde{\psi}^{ed}(\lambda_e) + \tilde{\psi}^{ev}(J) + \tilde{\psi}^{et}(J, T) + \tilde{\psi}^{T}(T), \tag{2.22}$$

where $\tilde{\psi}^{ed}(\lambda_e)$ represents the isochoric component of $\tilde{\psi}$ formulated as

$$\tilde{\psi}^{ed}(\lambda_e) = G\sum_{i}^{3}(ln(\lambda_{e,i}))^2. \tag{2.23}$$

Here G is the shear modulus. $\tilde{\psi}^{ev}$ is the volumetric component given by

$$\tilde{\psi}^{ev}(J) = \frac{k}{2}(ln(J))^2, \tag{2.24}$$

where k is the bulk modulus. $\tilde{\psi}^{et}$ is the thermoelastic component given by

$$\tilde{\psi}^{et}(J,T) = (T - T_0)(-3\alpha(\frac{\partial \tilde{\psi}^{ev}}{\partial J})), \tag{2.25}$$

where α is the linear coefficient of thermal dilation, and T_0 is the ambient temperature. Finally, $\tilde{\psi}^{T}(T)$ is purely a temperature dependent component given by

$$\tilde{\psi}^{T}(T) = \rho_o C_v((T - T_o) - T(ln(\frac{T}{T_0})). \tag{2.26}$$

Using the above mentioned form for the stored potential energy it can be shown that the volumetric stress p, and deviatoric stress $\bar{\tau}_{ii}$ is given by

$$p = \frac{1}{J}(kln(J) - 3k\alpha(T - T_0)\frac{(1 - ln(J))}{J}), \quad \bar{\tau}_{ii} = 2Gln(\lambda_{e,i})). \tag{2.27}$$

2.4 Energetics

The main focus of this study is to characterize the dissipation occurring due to the deformation of granular energetic particles subjected to high speed impacts. Emphasis is placed on characterizing plastic and frictional dissipation since they are the significant dissipation mechanisms within the context of this model.

Conventionally, the total energy of a particle can be expressed as a sum of its internal and kinetic energies. The internal energy given in Eq. 2.3 changes due to heat and work contributions. In this study, the changes in internal energy are solely due to impact induced deformation. We define a term called the deformation power given by

$$\mathcal{P} = \frac{1}{\rho_0}\tau : d, \tag{2.28}$$

where ρ_0 is the initial density, and d is the deformation rate tensor. Deformation rate tensor can be further partitioned into elastic d_e and plastic d_p components as $d = d_e + d_p$. By partitioning τ into its volumetric and deviatoric components as $\tau = Jp + \bar{\tau}$ and using it in

Eq. 2.28, the deformation power can be written as

$$\mathcal{P} = \frac{1}{\rho_0}(\bar{\tau} : d_e) + \frac{1}{\rho_0}(\tau : d) + \frac{Jp}{\rho_0}(1 : d_e). \tag{2.29}$$

The first term on the right hand side represents the non-thermal increase in the shear strain energy, whereas the remaining terms account for deformation induced heating due to plastic work and compression work. Based on the expression for $\mathcal{P}$ the total instantaneous deformation work for a particle Ω can be expressed as

$$W_d(t) = \int_m \int_0^t \frac{1}{\rho_0}(\tau : d) dt dm. \tag{2.30}$$

Also the expressions for instantaneous elastic shear strain energy, plastic and compression work are given by

$$W_s(t) = \int_m \int_0^t \frac{1}{\rho_0}(\bar{\tau} : (d_e)) dt dm, \tag{2.31}$$

$$W_c(t) = \int_m \int_0^t \frac{JP}{\rho_0}(1 : (d_e)) dt dm, \tag{2.32}$$

$$W_p(t) = \int_m \int_0^t \frac{1}{\rho_0}(\tau : (d_p)) dt dm. \tag{2.33}$$

Another form of important work contribution which influences material heating is friction work. In this study, friction is imposed at the contact interface as a boundary condition, and will be discussed in the following section. The instantaneous friction work is given by

$$W_f(t) = \int_{\cup\Gamma_c} \int_0^t t_c \cdot v_r dt ds, \tag{2.34}$$

where t_c is the traction force due to contact, v_r is the relative velocity between the contact surfaces, and $\cup\Gamma_c$ is the summation over all the contact surfaces.

2.5 Initial and Boundary Conditions

In this section, the relevant initial and boundary conditions on the displacement and thermal fields used in this study are summarized. A comprehensive discussion on the boundary conditions can be found in [61].

Here, discussions are restricted to two deformable particles, however they can be easily extended to multi-particle contacts. For convenience, in the remainder of this section these particles would be referred to as Ω^1 and Ω^2. The material points within Ω^1 are denoted by x, and points within Ω^2 by y. The boundary of each particle Γ can be divided into three regions based on the type of boundary condition prescribed. Γ_σ to prescribe tractions, Γ_u to prescribe displacements, and Γ_c which is the contact boundary. The initial and boundary conditions are prescribed as follows (Figure 2.2)

$$\sigma \cdot n_\sigma = \bar{t}_\sigma \quad \text{on} \quad \Gamma_\sigma \quad \forall t, \tag{2.35}$$

$$u = \bar{u} \quad \text{on} \quad \Gamma_u \quad \forall t, \tag{2.36}$$

$$\dot{u} = 0 \quad \text{on} \quad \Omega \quad \text{at} \quad t = 0, \tag{2.37}$$

$$u = 0 \quad \text{on} \quad \Omega \quad \text{at} \quad t = 0, \tag{2.38}$$

where $\bar{t}_\sigma$ and $\bar{u}$ are the prescribed traction and displacement vectors, n_σ is the unit outward normal vector to Γ_σ. In this study the initial velocity and displacement fields are set to zero. Also no initial traction and displacement boundary conditions are prescribed which means that the IBVP for each particle is due to the contact forces arising due to piston impact. Similarly, the temperature boundary conditions can be divided into three regions; Γ_T where temperature is prescribed, Γ_q where the flux is described, and Γ_c is the contact boundary.

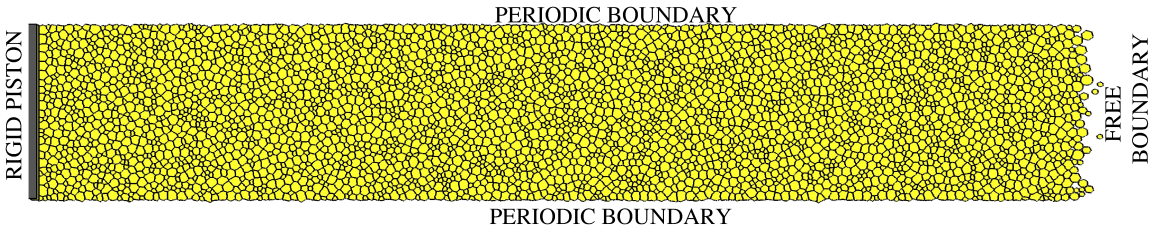

Figure 2.2: Schematic of the relevant boundary conditions

The corresponding conditions are given by

$$T = \bar{T} \quad \text{on} \quad \Gamma_T \quad \forall t, \tag{2.39}$$

$$-k\nabla_x T \cdot n_q = \bar{q} \quad \text{on} \quad \Gamma_q \quad \forall t, \tag{2.40}$$

$$T = T_0 \quad \text{on} \quad \Omega \quad \text{at} \quad t = 0. \tag{2.41}$$

Here n_q is the unit outward normal vector to Γ_q, and T_0 is the initial temperature. In this analysis no temperature boundary condition is prescribed, and also adiabatic assumption is made at the contact interface which means $\bar{q} = 0$.

The contact boundary conditions in this analysis are estimated using a 2D conservative potential based penalty method. Penalty methods are typically used in numerical algorithms for solving constrained optimization problems [58]. Penalty methods represent a soft particle approach wherein the contacting particles are allowed to penetrate each other while penalizing their penetration subject to kinematic and thermal constraints. To quantify the extend of inter particle penetration at the boundaries between the two particles Γ_c^1 and Γ_c^2, a gap function is introduced which is mathematically defined as

$$g(x) = (x - \bar{y}(x)) \cdot n_c^1(x), \tag{2.42}$$

where $g(x)$ is the gap function, n_c^1 is the outward normal to Γ_c^1, $\bar{y}(x)$ is the closest point project of x onto Γ_c^2. The local compressive normal traction is given by $t_N^1(x) = (-\sigma^1(x).n_c^1(x)).n_c^1(x)$, which is positive in compression, with the contact constraints given by the Kuhn-Tucker op-

timality conditions : $g \geq 0$, $t_N \geq 0$, and $t_N g = 0$. The inequalities impose the constraints that the particles be impenetrable, the interaction be compressive, and that compressive normal tractions should arise only due to contact.

To estimate the frictional tractions, a frictional traction vector t_t^1 is estimated based on Amontons-Coulomb law of friction wherein; a contact is assumed to stick if $\phi_t = |t_t^1| - \mu t_N^1 \leq 0$, where μ is the friction coefficient. Tangential contact conditions arising due to friction are imposed by introducing a slip function u_t which is a local measure of relative tangential displacement between the contacting surfaces

$$u_t(x) = (u^1(x) - u^2(\bar{y}(x))) - [u^1(x) - u^2(\bar{y}(x))) \cdot n_c^1(x)]n_c^1(x). \tag{2.43}$$

Similar to the displacement contact condition, the thermal contact condition can be defined by introducing a thermal gap function g_{th} defined as

$$g_{th}(x) = T^1(x) - T^2(\bar{y}(x)). \tag{2.44}$$

Contact boundary condition for the temperature field can be summarized as,

$$(-K_T \nabla_x T) \cdot n_c^i = q_f^i + q_c^i, \quad \text{on} \quad \Gamma_c^i, \tag{2.45}$$

where q_f^i is the heat flux due to frictional dissipation, and q_c^i is the heat flux necessary to impose ideal thermal contact. The heat flux is partitioned between the contacting surfaces based on the relation

$$q_f^1 = \omega q_f, \qquad q_f^2 = (1 - \omega) q_f, \tag{2.46}$$

where the partition function ω is given by

$$\omega = (1 + \sqrt{\frac{K_T^2 c_v^2 \rho^2}{K_T^1 c_v^1 \rho^1}}) \tag{2.47}$$

Also, ideal thermal contact is enforced between the contacting particles since thermal resistance is ignored for both stick and slip conditions, and this can be defined as

$$T^1(x,t) = T^2(\bar{y}(x),t) \quad \text{on} \quad \Gamma_c^1, \Gamma_c^2 \quad \forall t. \tag{2.48}$$

The resulting heat flux required to enforce this condition across the interface is given by

$$q_c^1 = -q_c^2 = R(T^1(x,t) - T^2(\bar{y}(x),t)), \tag{2.49}$$

where R is the contact conductance which for ideal thermal contact is $R = \infty$. This constraint is numerically implemented similar to the displacement contact constraints by assuming R to be the thermal penalty parameter pe^{th}. The numerical implementation of the mathematical model is described in the following chapter.

CHAPTER 3
NUMERICAL METHOD

This chapter briefly describes the numerical technique used in solving the governing equations discussed in the previous chapter. A comprehensive analysis of the same can be found in [58, 61]. In this study, a combined 2D finite element (FEM) and discrete element method (DEM) is used to simulate the impact response of granular explosives. FEM is used to numerically integrate the conservation equations and viscoplastic flow rule governing particle deformation. DEM is used to estimate contact forces due to particle (discrete element) interactions. The outline of the chapter is as follows. First, weak form of the governing equations are presented. Second, numerical estimates of the internal and external forces arising due to impact are presented. Finally, a brief description of pseudo gravity settling algorithm used to create the initial meso-structures and some computational issues associated with high performance computing (HPC) are discussed.

Each particle Ω is discretized into a number of three noded constant strain triangular (CST) finite elements. Displacement, velocity, and temperature are obtained at the nodes, and can be estimated at non-nodal locations using the interpolation functions for CST finite elements. Material state variables such as density, and stress are estimated at interpolation points within the elements. The initial position of any material point within the particle can be estimated by using the interpolation functions for CST elements given by

$$X = \sum_{k=1}^{3} N_k X_k, \tag{3.1}$$

where N_k is the standard shape function associated with node k. During subsequent motion and deformation, the elements and nodes are attached to the material points with which they were initially associated. The motion of these particles can be described based on the

current position x and the displacement of nodes u as

$$x = \sum_{k=1}^{3} N_k x_k, \qquad u = \sum_{k=1}^{3} N_k u_k, \tag{3.2}$$

In Cartesian coordinates, the shape function for CST in the current configuration is given by

$$\begin{bmatrix} N_1 \\ N_2 \\ N_3 \end{bmatrix} = \frac{1}{2A} \begin{bmatrix} \alpha_1 & \beta_1 & \gamma_1 \\ \alpha_2 & \beta_2 & \gamma_2 \\ \alpha_3 & \beta_3 & \gamma_3 \end{bmatrix} \begin{bmatrix} x \\ y \\ z \end{bmatrix}, \tag{3.3}$$

where

$$\begin{bmatrix} \alpha_1 & \beta_1 & \gamma_1 \\ \alpha_2 & \beta_2 & \gamma_2 \\ \alpha_3 & \beta_3 & \gamma_3 \end{bmatrix} = \begin{bmatrix} x_2y_3 - y_2x_3 & y_2 - y_3 & x_3 - x_1 \\ y_1x_3 - x_1y_3 & y_3 - y_1 & x_1 - x_3 \\ x_1y_2 - y_1x_2 & y_1 - y_2 & x_2 - x_1 \end{bmatrix}. \tag{3.4}$$

Here, A is the area in the current configuration.

3.1 Weak Formulation of Conservation Equations

In conventional finite element method, continuous governing equations are converted into a set of algebraic equations by first converting the strong form of the equations to their corresponding weak forms. To convert the strong form of momentum equation, the principal of virtual work is used in this study. If δv denotes the virtual velocity from the current position of an arbitrary particle Ω, then, in equilibrium the work done by the residual forces during the virtual displacement is given by

$$\delta\mathcal{W} - \int_{\Omega} (\nabla_x . \sigma - \rho\ddot{u}) . \delta v d\Omega = 0, \tag{3.5}$$

where $\delta\mathcal{W}$ represents the virtual work. Using the divergence theorem and simplifying, Eq. 3.5 can be written as

$$\delta\mathcal{W} = \int_{\Omega} (\sigma : \nabla_x \delta v + \rho\ddot{u} . \delta v) d\Omega - \int_{\Gamma} n . \sigma \delta v d\Gamma = 0, \tag{3.6}$$

Here, the last term of the equation corresponds to the virtual work due to contact. The virtual work can be further expressed as the summation of all the individual weak forms for multi-particle contact as

$$\delta\mathcal{W} = \sum_{i=1}^{N_p} \delta\mathcal{W}^i = \delta\mathcal{W}_m + \delta\mathcal{W}_i + \delta\mathcal{W}_e = 0, \tag{3.7}$$

where N_p is the number of particles, $\mathcal{W}_m$, $\mathcal{W}_i$, $\mathcal{W}_e$ represent the total virtual work due to inertial terms, internal stresses and contact forces respectively. The expressions for these virtual work contributions are given as

$$\delta\mathcal{W}_m = \sum_{i}^{N_p} (\int_{\Omega^i} (\rho^i \ddot{u^i}.\delta v^i) d\Omega^i), \tag{3.8}$$

$$\delta\mathcal{W}_i = \sum_{i}^{N_p} (\int_{\Omega^i} (\rho^i : \delta d^i) d\Omega^i), \tag{3.9}$$

$$\delta\mathcal{W}_e = \sum_{i}^{N_p} (\int_{\Gamma^i} (-t_c^i.\delta v^i) d\Omega^i). \tag{3.10}$$

The formulation of the weak form leads to a set of algebraic equations in the finite element form given by

$$\mathcal{M}\ddot{\mathcal{U}} - \mathcal{F}_i - \mathcal{F}_e = 0, \tag{3.11}$$

where $\mathcal{U}[N_n, 3]$ is the global nodal displacement matrix, $\mathcal{M}[N_n, N_n]$ is the global nodal mass matrix, $\mathcal{F}_e[N_n, 3]$, and $\mathcal{F}_i[N_n, 3]$ are the global nodal external and internal force vectors that represent the finite element discretizations of the virtual work contributions. Here N_n is the total number of nodes in the discretized system. For brevity only the simplified form of the mass, and force matrices are presented here. A comprehensive discussion of the analysis can be found in [61]. For an arbitrary element Δ^j connected by a pair of nodes $k, l = 1, 2, 3$, the mass, internal and external force matrices are given as

$$[\mathcal{M}]_{kl} = \int_{\Delta^j} 2\rho N_k \delta_{kl} N_l dv, \qquad [\mathcal{F}_i]_k^j = \int_{\Delta^j} \rho \nabla_x N_k dv, \qquad [\mathcal{F}_e]_k^j = \int_{\Delta^j} N_k t_c da, \tag{3.12}$$

where δ_{kl} is the Kronecker delta, and a is the area of contact. The element mass matrix considered in this study corresponds to the lumped mass matrix, where discrete element mass is allocated to the nodes that make up the element. This is done so to reduce computational time and memory requirements by eliminating the need to assemble large stiffness and mass matrices that result in computational complexities. Finally the global mass and force matrices can be obtained by the summation over all the finite elements as

$$\mathcal{M} = \sum_{i=1}^{N_p} \sum_{j=1}^{N_e(i)} [\mathcal{M}]^j, \qquad \mathcal{F}_i = \sum_{i=1}^{N_p} \sum_{j=1}^{N_e(i)} [\mathcal{F}_i]^j, \qquad \mathcal{F}_e = \sum_{i=1}^{N_p} \sum_{j=1}^{N_e(i)} [\mathcal{F}_e]^j, \tag{3.13}$$

where $N_e(i)$ is the total number of finite elements in Ω_i.

Similar to the weak form of the momentum equation, the weak form of the energy/temperature equation for an arbitrary particle Ω can be obtained by defining a virtual temperature field δT and integrating over the the volume to give

$$\int_{\Omega} (\rho c_v \frac{dT}{dt} + \nabla_x . q - \dot{Q}_e - \dot{Q}_i) \delta T d\Omega = 0. \tag{3.14}$$

Using divergence theorem, the above equation can be written as

$$\int_{\Omega} (\rho c_v \frac{dT}{dt} - \dot{Q}_e - \dot{Q}_i) \delta T d\Omega) - \int_{\Omega} (q : \nabla_x \delta_T) d\Omega = - \int_{\Gamma_c} (q_f + q_c) \delta T d\Gamma_c. \tag{3.15}$$

The finite element form of the continuous temperature evolution equation is given by

$$\mathcal{M}_c \dot{\mathcal{T}} + \mathcal{K}_c \mathcal{T} = \mathcal{F}_c, \tag{3.16}$$

where $\mathcal{M}_c[N_n, N_n]$ is the lumped thermal capacitance matrix, $\mathcal{K}_c[N_n, N_n]$ is the stiffness matrix, $\mathcal{F}_c[N_n, 1]$ is the thermal force matrix, and $\mathcal{T}[N_n, 1]$ is the nodal temperature matrix. The simplified form of the contribution of a particular node k of element Δ^j to the element

thermal capacitance, stiffness and force matrices are given by

$$[\mathcal{M}_c]^j_{kl} = \int_{\Delta^j} 2\rho c_v N_k \delta_{kl} N_l dv, \tag{3.17}$$
$$[\mathcal{K}_c]^j_{kl} = \int_{\Delta^j} k_T \nabla_x N_K : \nabla_x N_l dv,$$
$$[\mathcal{F}_c]^j_k = \int_{\Delta^j} (\dot{Q}_e + \dot{Q}_i) N_k dv - \int_{\Delta^j_c} (q_f + q_c) N_k da.$$

The global capacitance, stiffness and force matrices can be obtained by summation over all the finite elements as

$$\mathcal{M}_c = \sum_{i=1}^{N_p} \sum_{j=1}^{N_e(i)} [\mathcal{M}_c^j], \qquad \mathcal{K}_c = \sum_{i=1}^{N_p} \sum_{j=1}^{N_e(i)} [\mathcal{K}_c^j], \qquad \mathcal{F}_c = \sum_{i=1}^{N_p} \sum_{j=1}^{N_e(i)} [\mathcal{F}_c^j]. \tag{3.18}$$

Finite element equations of motion for the nodal displacements $\mathcal{U}(t)$ and nodal temperature $\mathcal{T}(t)$ are integrated using a temporally second-order accurate explicit numerical technique. The finite element equations for momentum and energy at a time n is given by

$$\mathcal{M}\ddot{\mathcal{U}}_n = \mathcal{F}_{i,n} + \mathcal{F}_{e,n}, \qquad \mathcal{M}_c \dot{\mathcal{T}}_n + \mathcal{K}_{c,n} \mathcal{T}_n = \mathcal{F}_{c,n}. \tag{3.19}$$

The main purpose of the DEM is to estimate the forces that arise due to contact. The external force vector $\mathcal{F}_e$ is known before the start of each time step whereas the internal force vector $\mathcal{F}_i$, thermal load matrix $\mathcal{F}_c$, and the stiffness matrix K_c are functions of $\mathcal{U}_n$ and $\mathcal{T}_n$ which are the known displacement and temperatures at the nodes for a given time-step n.

The velocities and temperature at $n+1$ time step are calculated as per the equations given by

$$V_{n+1} = V_{n+\frac{1}{2}} + \frac{\Delta t}{2} \ddot{\mathcal{U}}_{n+1}, \tag{3.20}$$
$$\mathcal{T}_{n+1} = \mathcal{T}_n + \Delta t \dot{\mathcal{T}}_n. \tag{3.21}$$

Since the time stepping procedure is explicit, numerical instabilities may arise. Numerical stability for this problem means that the time step Δt be less than the time needed for an elastic wave to traverse within the finite element. Since acoustic wave transmission is faster within Al particles, our Δt is estimated based on elastic wavespeeds through Al. The longitudinal elastic wave speed D_l within Al particle with a value of Young's modulus $E = 70.0$ GPa, and density $\rho_0 = 2700\ Kg/m^3$ is given by $D_l = \sqrt{E}\rho_0 = 5091.71$ m/s. For the smallest finite element size used in this study $\Delta h \approx 3\mu m$, the mininum required time step needed for stability is $\Delta t_{crit} = \Delta h / D_l = 0.58$ ns. Therefore, a value of $\Delta t = 0.01$ ns $< \Delta t_{crit}$ was used for the all the simulations in this study.

3.2 Internal Force Matrix

The internal force $\mathcal{F}_{i,n}$ is an implicit function of the nodal displacements $\mathcal{U}_n$ and the associated stress fields τ_n within the particle. To estimate $\mathcal{F}_{i,n}$, a time stepping procedure is employed to the hyperelastic viscoplastic formulation discussed earlier. At time t_{n-1}, values for the left elastic Cauchy tensor $b_{e,n-1}$ and the deformation gradient F_{n-1} are known. At time t_n, F_n is obtained from $\mathcal{U}_n$ using the definition of deformation gradient tensor as

$$F_n = \frac{1}{2A_0}\begin{bmatrix} x_1Y_{23} + x_2Y_{31} + x_3Y_{12} & x_1X_{32} + x_2X_{13} + x_3X_{21} & 0 \\ y_1Y_{23} + y_2Y_{31} + y_3Y_{12} & y_1X_{32} + y_2X_{13} + y_3X_{21} & 0 \\ 0 & 0 & 1 \end{bmatrix} \tag{3.22}$$

where $X_{kl} = X_k - X_l$, and $Y_{kl} = Y_k - Y_l$. The plane strain conditions enforced in this analysis result in the principal out of plane component of F to unity, and the deviatoric components to zero. The time stepping procedure is employed in the following way. First, the plastic variables are assumed to be constant in time during the current increment. This means that the incremental deformation is assumed to be completely elastic. Therefore, a guess/trail value for b_e and ϵ_p are computed as $b_e^{trail} = f_r b_{e,n-1} f_r^T$ and $\epsilon_p^{trail} = \epsilon_{p,n-1}$. Here $f_r = F_n F_{n-1}^{-1}$ is the incremental deformation gradient. As mentioned earlier, b_e^{trail} can be decomposed into its eigenvalues and eigenvectors λ_e^{trail} and n^{trail}. Subsequently, the volumetric and deviatoric

components of the trail Kirchhoff stress tensor can be written as

$$p^{trail} = \frac{1}{J_n}(kln(J_n) - 3k\alpha(T_n - T_0)(\frac{(1 - ln(J_n))}{J_n}), \tag{3.23}$$

$$\bar{\tau}_{ii}^{trail} = 2Gln(\frac{\lambda_{e,i}^{trail}}{J_n^{1/3}}), \tag{3.24}$$

where T_n is the elemental temperature at time t_n. J_n represents volumetric change associated with particle deformation. The plastic correlation procedure does not change its values since Von Mises yield criterion is volume preserving. The element temperature T_n is fixed during the plastic correction. Therefore, plastic correction procedure does not affect the pressure i.e., $p_n = p^{trail}$.

Based on $\bar{\tau}^{trail}$ the yield criterion ϕ^{trail} can be written as

$$\phi^{trail} = \sqrt{\bar{\tau}^{trail} : \bar{\tau}^{trail}} - \sqrt{\frac{2}{3}}(\tau_0). \tag{3.25}$$

If $\phi^{trail} \leq 0$ then the material deformation is completely elastic, and the trail values are the correct values. If $\phi^{trail} > 0$, the evolution equations for the plastic variables are integrated using an implicit forward Euler method to estimate $b_{e,n}$, and $\epsilon_{p,n}$. The true elastic stretches (eigenvalues) are obtained as $\lambda_{e,i} = exp(-\Delta\epsilon\xi_i)\lambda_{e,i}^{trail}$ where

$$\xi_i = \frac{\tau_{ii}^{trail}}{\sqrt{\bar{\tau}^{trail} : \bar{\tau}^{trail}}}. \tag{3.26}$$

Here, $\Delta\epsilon$ is the consistency parameter defined as $\Delta\epsilon = \int_{t_{n-1}}^{t_n} \dot{\epsilon} dt$. After the true elastic stretches have been updated, the elastic left Cauchy-Green tensor can be written as

$$b_{e,n} = \sum_{i=1}^{3} (\lambda_{e,i})^2 n_i \otimes n_i. \tag{3.27}$$

Further, the Von Mises equivalent plastic strain is updated as

$$\epsilon_{p,n} = \epsilon_{p,n-1} + \sqrt{\frac{2}{3}}\Delta\epsilon, \tag{3.28}$$

and the actual deviatoric stress can be written as

$$\bar{\tau}_{ii} = \bar{\tau}_{ii}^{trail} - 2G\Delta\epsilon\xi_i. \tag{3.29}$$

The closed form for the consistency parameter can be written as

$$\Delta\epsilon = \frac{1}{2G}\langle\frac{\phi^{trail}}{1 + (h + \gamma\Delta t)/3G)}\rangle. \tag{3.30}$$

After obtaining the stress states within each finite element, the nodal internal force acting on each finite element can be written as

$$[\mathcal{F}]_{i,n}^{j} = 0.5\begin{bmatrix} \sigma_{n,11}(y_2 - y_3) + \sigma_{n,12}(x_3 - x_2)) & \sigma_{n,21}(y_2 - y_3) + \sigma_{n,22}(x_3 - x_2)) & 0 \\ \sigma_{n,11}(y_3 - y_1) + \sigma_{n,12}(x_1 - x_3)) & \sigma_{n,21}(y_3 - y_1) + \sigma_{n,22}(x_1 - x_3)) & 0 \\ \sigma_{n,11}(y_1 - y_2) + \sigma_{n,12}(x_2 - x_1)) & \sigma_{n,21}(y_1 - y_2) + \sigma_{n,22}(x_2 - x_1)) & 0 \end{bmatrix}, \tag{3.31}$$

where $\sigma_n = \tau_n/J_n$

3.3 Contact Force Matrix

The penalty method used in this analysis works by penalizing the violations of the kinematic constraints. This is done by formulating a suitable measure of particle penetration at the boundaries, and then multiplying it with a penalty parameter. The advantage of the penalty method over variational formulation such as Lagrangian multiplier technique is that the problem can be cast in terms of only the displacement field u. This simple description of boundary interaction, results in a system of equations which can be easily integrated. A comprehensive discussion of the penalty method used in this study can be found in [58], and only the final forms of the equations that are used in the numerical implementation of the

problem are presented here. The normal and tangential tractions arising due to contact are given by

$$t_N = pe^n \langle g \rangle, \qquad t_t = pe^t u_t, \tag{3.32}$$

where pe^n and pe^t are the normal and tangential penalty parameters respectively, and u_t is the slip function which defines the measure of tangential displacement between contacting particles. To estimate the normal component of the contact/external force matrix $\mathcal{F}_e$ arising due to contact, a modified gap potential is used instead of the conventional gap potential given by Eq. 2.42. The modified gap potential is defined for all the points located within the penetration region. This is done in order to handle contact between contacting elements on an edge to edge or edge to node manner, rather than node to node manner which leads to artificially high strains at the contact interface. Consider contact between two particles (discrete elements), where one of the particles in contact is termed as the contactor particle Ω_c while the other is considered as the target particle Ω_t. Since the particles penetrate each other, an overlap area can be defined between the two as Ω_{ct} with a boundary defined by Γ_{ct}. For a small elemental area dA within the region of overlap, the differential normal contact force described by the 2-D penalty method is given by

$$df_N = pe^n(\nabla_x \Phi_c(p_c) - \nabla_x \Phi_t(p_t))da, \tag{3.33}$$

where Φ_c and Φ_t are the modified conservative gap potential fields of the contactor and target elements respectively, and p_c and p_t are the global position vectors of the contactor and target element within dA. The differential contact force can also be expressed as $df_N = df_t + df_c$ where df_c and df_t are the components of the target penetrating the contactor and the contactor penetrating the target respectively. Mathematically, df_c, and df_t are expressed as

$$df_c = -pe^n \nabla_x \Phi_t(p_t) dA, \qquad df_t = -pe^n \nabla_x \Phi_c(p_c) dA. \tag{3.34}$$

The net force can be obtained by integrating the differential forces over the entire overlapping area. The discrete finite element force of the total force is given by

$$f_N = pe^n \sum_{i=1}^{n} \sum_{j=1}^{m} \int_{\Gamma_{\Delta_c^i \cap \Delta_t^j}} n_{\Delta_c^i \cap \Delta_t^j} [\Phi_c^i - \Phi_t^j] d\Gamma_{\Delta_c^i \cap \Delta_t^j}, \tag{3.35}$$

where the limits of summation n, and m represents the total number of finite elements in the contactor and target particle. Also Φ_c^i and Φ_t^j are the potentials of the i^{th} and j^{th} finite element of the contactor and target particle respectively. Here $n_{\Delta_c^i \cap \Delta_t^j}$ represents the outward unit normal vector to $\Gamma_{\Delta_c^i \cap \Delta_t^j}$ which is the boundary of interaction region between the two contacting finite elements. It is obvious that the choice of the penalty parameter pe^n influences the magnitude of the contact forces. However, to avoid numerical stiffness that may arise due to large values of the penalty parameter, a suitable value of the penalty parameter has to be chosen. In this analysis the magnitude of the normal penalty parameter is chosen as $pe^n = 10^9$ since it is of the same order of magnitude as the Youngs modulus of both HMX and Al. This value of the penalty parameter was guided by numerical experiments on stability analysis performed by [61].

To estimate the tangential tractions arising due to friction, a penalty regularized Amontons-Coulomb law, also known as plasticity theory of friction is implemented. Though the regularized friction law does not enforce frictional constraints exactly, it is computationally easier to implement. The main idea is to split the tangential slip defined by u_t into stick/adhesion part $u_{t,e}$ and a plastic slip part $u_{t,p}$ i.e., $u_t = u_{t,e} + u_{t,p}$. Similar to the Von Mises yield criterion, a slip surface ϕ_t is introduced in the contact stress areas where slip is likely to occur. Mathematically the slip surface is defined as

$$\phi_t = |t_t| - \mu t_N. \tag{3.36}$$

As defined earlier, the tangential traction can be defined similar to the normal traction as

$$\dot{t}_t = pe^t(\dot{u}_t - \dot{u}_{t,p}), \tag{3.37}$$

where pe^t is the tangential penalty parameter. For a penalty parameter of $pe^t = \infty$ the classical Amontons-Coulomb law is obtained. However, the tangential penalty parameters are assumed to scale as inverse of the time increment Δt for numerical stability. Finally, the system of equations are closed by assuming the evolution equation for $\dot{u}_{t,p}$ as

$$\dot{u}_{t,p} = \dot{\epsilon}_t \frac{\partial \phi_t}{\partial t_t}, \tag{3.38}$$

where $\dot{\epsilon}_t$ is the frictional multiplier similar to the plastic multiplier in the rate independent formulation of perfect plasticity. Finally, the total external force matrix is given by the matrix sum of its normal and tangential components.

Thermal contact constraints are similar to the kinematic contact constraints wherein the violations are penalized by defining a thermal gap potential. A comprehensive discussion can be found in [61], and only the final results of the mathematical formulation are presented here. The potential field at a point p on the boundary of a contactor finite element Δ^j that is in contact with a target element Δ^i is given by

$$\Phi_T(p) = T_n^j(p) - T_n^i(p), \tag{3.39}$$

where $T_n^j(p)$ and $T_n^i(p)$ are the interpolated temperatures at point p corresponding to the contactor and target finite elements respectively. Like the method outlined in estimating the kinematic potential, the net potential for Δ^j is obtained by summation of potential at all points p on the boundary of the contactor element. To maintain, ideal thermal contact

constraints, the contact flux between the contacting edges is given by

$$q_c = pe^{th}\Phi_{T,c}. \tag{3.40}$$

For $pe^{th} = \infty$ perfect thermal contact is observed. However, in this analysis a thermal penalty parameter of $pe^{th} = 10^9$ is used for numerical stability. A summary of the relevant penalty parameters is given in Table 3.1. To detect contact between the particles, a conventional nearest neighbor contact detection algorithm was implemented. The static cell detection algorithm used in this study is numerical easy to implement, and is also memory efficient while modeling granular materials with reasonably high packing densities. The details of the contact detection algorithm can be found in [58, 61]. The numerical technique has been verified against both known analytical solutions for simple problems and predictions given by the well-established impact mechanics software Ls-Dyna for more complex problems. The technique was shown to be convergent, and its spatial (≈ 2.0) and temporal (≈ 1.5) convergence rates were established. A comprehensive discussion of verification results for this algorithm are given in Ref. [61]. Validation comparing predictions to experimental values is discussed in chapter 4.

Table 3.1: Values for the numerical parameters.

Parameter	Value	Units
Penalty Parameter Normal, pe^n	50×10^9	—
Penalty Parameter Tangential, pe^t	1×10^{11}	—
Penalty Parameter Thermal, pe^{th}	1×10^9	—
Time Increment, Δt	0.01	ns

3.4 Preprocessing

In this study a pseudo gravity settling algorithm is used to generate the initial meso-structures. Brief overview of the gravity settling algorithm is as follows. First, particles are placed within the domain with the constraint that the center of one particle cannot lie within the boundary of another; however the particles can overlap. Second, the magnitude of overlap

is used to calculate the forces needed to move the particles to a zero overlap position while continuously being acted by gravity. The magnitude of the force is directly proportional to the amount of overlap. While it is easier to compute the overlap between circular particles, it is harder to compute the magnitude of overlap between randomly shaped convex particles. To estimate the overlap between such particles, separating axis theorem (SAT) was numerically implemented within the pseudo gravity settling algorithm. Separating axis theorem states that two convex particles do not overlap if there exists a line/axis on which the projection of two particles results in distinct lines. The disadvantage of SAT algorithm is that it is only applicable to convex particles, and the computational time increases linearly with the number of sides of the polygonal particles under consideration.

As mentioned, the discrete elements were meshed using CST elements. For the ensembles considered in this study, the smallest particles ($d = 40\ \mu m$) are composed of around 300 CST, while the largest particles ($d = 260\ \mu m$) are made up of around 2800 finite elements. The total number of finite elements in the domain for all the the ensembles is around $N_{ele} =$ 2-3 million. The choice of our resolution was motivated by the available computational resource for the problem. The unstructured mesh generation for the discrete elements was achieved using an open source matlab program Distmesh2D [63]. The numerical algorithm was implemented using Fortran 90 programming language. Parallelization was achieved using standard MPI libraries for Fortran. The average run time for our simulations was around 5 days on 64 Intel Xeon processors with a computing speed of 2.4 GHz.

3.5 Computational Issues

The system of governing equations along with the numerical method employed to solve the multi-body contact problem results in a number of coupled non-linear system of equations. For such non-linear systems, it is well established that perturbations occurring due to computational errors can result in different end states even if identical initial conditions are enforced in the beginning of the simulations [69]. These variations in end states are often encountered in numerical modeling of turbulent fluid flows [16, 74]. In complex parallel

codes such as the one used in this study, several computational errors can contribute to perturbations such as rounding errors, parallelization errors, and compiler optimization errors. Round off errors are generally the primary source of noise generation in most finite precision computation. Machine epsilon ϵ which in essence represents the least count of the machine is a major source of round of error which depends on the computer architecture/platform [69].

In codes requiring domain partitioning, the handling of interfaces can also be a source of numerical error. The main source of error due to parallelization comes from variations in order of operation due to non-deterministic message arrival at the domain interface. For example, $m = (a - b/c) + d$ and $m = a + (d - b/c)$ may result in different values of m due to round of errors though the analytical solution is identical. One way to mitigate this issue is by inserting MPI-BARRIER calls which stalls mathematical operations until all of the required inputs are received at the call location. However, MPI-BARRIER calls can significantly increase the computational time. Finally, compiler options, in particular those concerning code optimizations and/or those affecting truncation errors can be an additional source of numerical error. In this study, Intel Fortran compilers were used in all our simulations though the versions of these compilers and the corresponding MPI libraries varied due to different processor architecture.

The above mentioned computer architecture issues were largely mitigated by using proper MPI-BARRIER calls within the parallel code, and using certain compiler options/flags. Testing was done on three available clusters within the LSU HPC and LONI systems, and the results were reproducible across the clusters.

CHAPTER 4
EFFECTS OF POROSITY AND COMPOSITION

It was mentioned in Chapter 1, that variations in the initial meso-structures are characterized by changes in packing densities $\bar{\phi}_s$ and/or compositions λ_m, particle sizes and shapes. This chapter primarily focuses on characterizing the effects $\bar{\phi}_s$, and λ_m on shock sensitivity of granular HE. For simplicity, only minor variations in particle shapes (hexagonal or circular) are considered. The effects of particle size are characterized in Chapter 5. Variations in explosive sensitivity arising due to material stochasticity are addressed in Chapter 6. The details of the meso-structures used in this chapter are summarized in Table 4.1, and Figure 4.1 shows these meso-structures, where the yellow particles represent HMX, and red particles represent Al. The meso-structures consist of hexagonal and/or circular particles having particle diameters of either 40 μm, 60 μm, or 80 μm. Each of these particle sizes constitute about 1/3 the total number of particles (4000) within the meso-structures. With respect to the hexagonal particles, diameter represents the length of the line connecting opposite vertices. The effective packing density ranges from $0.678 \leq \bar{\phi}_s \leq 0.835$, however the packing densities can spatially vary within each meso-structures as shown in Figure 4.1. An increase in $\bar{\phi}_s$ is found to create more spatially homogeneous meso-structures due to the limitations of the pseudo-gravity settling algorithm. In this chapter, an effective metal mass fraction of $\lambda_m = 0.2$ is used in all the metalized explosive formulations. This amount of metal is commonly used in explosive formulations since it has been observed to provide optimal blast effect [32]. Meso-structures consisting of just the HMX particles ($\lambda_m = 0$), serve as baseline cases, and are referred to as *Neat HMX* meso-structures.

The plan of this chapter is as follows. First, the relevant aspects of the 1-D spatial averaging technique used in this analysis are presented. A comprehensive discussion on the spatial averaging technique can be found in [61]. For brevity, a brief discussion on the

Table 4.1: Summary of the initial meso-structures used to study the effects of packing density $\bar{\phi}_s$ and composition λ_m. Here, particle size refers to its diameter.

Meso-Structure	$\bar{\phi}_s$	σ_ϕ	Particle Shape	Avg. Size (μm)	Particle Size Distribution
A	0.678	0.031	6:1 Hexagonal: Circular	60	40-60-80 (33.33% each)
B	0.76	0.008	6:1 Hexagonal: Circular	60	40-60-80 (33.33% each)
C	0.835	0.005	Circular	60	40-60-80 (33.33% each)

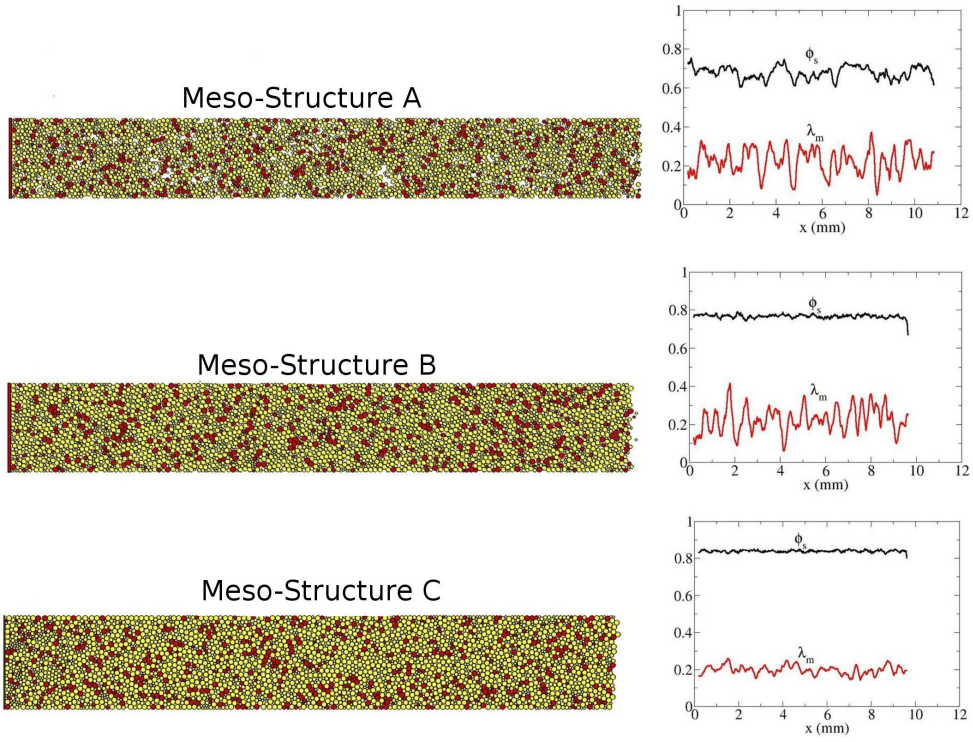

Figure 4.1: Meso-structures with varying packing densities $\bar{\phi}_s$ and composition λ_m. Here, red particles represent metal, and yellow particles represent explosive.

influence of metal on the 1-D spatial wave profiles of the explosive is presented. A detailed discussion on the same can be found in our published work [17]. Emphasis is placed on quantifying the effective wave end states commonly referred to as *Hugoniots* and the wave rise times. The wave rise times quantify the deformation wave thickness. Hugoniots and wave rise times are useful in determining the macro-scale shock response of explosives, and

therefore are routinely measured in compaction experiments, and are also used in macro-scale compaction models. Additionally, the meso-scale model predictions can be compared to experimentally obtained Hugoniots and wave rise times to validate the model. The final section of this chapter provides a comprehensive discussion on the statistical characterization of the resulting hot-spot fields in the explosive component since the material sensitivity is largely influenced by the onset of chemical activity within the explosive particles.

4.1 Spatial Wave Structure

4.1.1 Averaging Technique

To estimate the effective value of a generic variable Φ_i associated with component i at an axial location $x = \overline{x}$, an averaging area A is locally defined centered about $\overline{x}$ which represents a rectangle of length δx and width H. The appropriate effective value is computed based on all finite elements of that component contained within the averaging area (Figure 4.2). Mass weighted averages are performed for variables that represent mass specific quantities, such as temperature (based on mass specific thermal energy), plastic and friction work (mass specific energy), and velocity (mass specific momentum). Variables that represent volume specific quantities, such as mass density (volume specific mass) and stress (volume specific energy), are obtained using area weighted averages. For a variable Φ_i, at an axial position $x = \overline{x}$, mass and area weighted averages are respectively defined by

$$\text{Mass: } \overline{\Phi}_i(\overline{x}) = \frac{\sum_{j=1}^{\mathcal{N}_{a,i}} \hat{\Phi}_i^{(j)} \rho_i^{(j)} A_i^{(j)}}{\sum_{j=1}^{\mathcal{N}_{a,i}} \rho_i^{(j)} A_i^{(j)}}, \qquad \text{Area: } \overline{\Phi}_i(\bar{x}) = \frac{\sum_{j=1}^{\mathcal{N}_{a,i}} \hat{\Phi}_i^{(j)} A_i^{(j)}}{\sum_{j=1}^{\mathcal{N}_{a,i}} A_i^{(j)}}, \tag{4.1}$$

where $\hat{\Phi}_i^{(j)}$ is the value of the variable at the centroid of finite element $\Delta_i^{(j)}$, $A_i^{(j)}$ is its current area, $\rho_i^{(j)}$ is its current density, and $\mathcal{N}_{a,i}$ is the number of finite elements within the averaging area. The smoothness of the effective profiles depends on both the number of axial positions n at which averages are locally computed and the length of the averaging area δx, and is more sensitive to the choice of δx than n. All transverse averages shown in this study were computed using $n = 399$ and $\delta x = 200\ \mu m$. Minimal variation in the effective profiles were

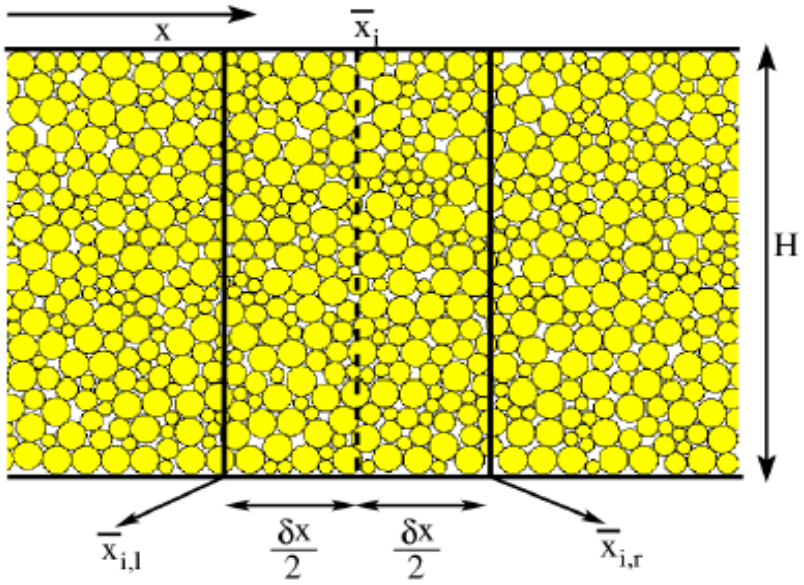

Figure 4.2: Schematic illustrating the 1-D averaging technique used to obtain the spatial wave profiles [61]

predicted for modest variations in n and δ_x about these values. The root mean square (RMS) fluctuations of this variable are estimated in the standard way:

$$\text{Mass:} \quad \widetilde{\Phi}_i(\bar{x}) = \sqrt{\frac{1}{\mathcal{N}_{a,i}} \sum_{j=1}^{\mathcal{N}_{a,i}} \left(\hat{\Phi}_i^{(j)} \rho_i^{(j)} A_i^{(j)} - \overline{\Phi}_i(\bar{x}) \right)^2}, \tag{4.2}$$

and

$$\text{Area:} \quad \widetilde{\Phi}_i(\overline{x}) = \sqrt{\frac{1}{\mathcal{N}_{a,i}} \sum_{j=1}^{\mathcal{N}_{a,i}} \left(\hat{\Phi}_i^{(j)} A_i^{(j)} - \overline{\Phi}_i(\overline{x}) \right)^2}. \tag{4.3}$$

The effective solid volume fraction of component i at axial position $\overline{x}$ is given by

$$\phi_i(\overline{x}) = \frac{1}{H \delta x} \sum_{j=1}^{\mathcal{N}_{a,i}} A_i^{(j)}, \tag{4.4}$$

where the total solid volume fraction is given by $\phi_s(\overline{x}) = \sum \phi_i(\overline{x})/n$.

Table 4.2 provides values for the thermo-mechanical properties of the explosive and metal used in the simulations. Differences exist in several of these component-specific properties that may influence the deformation response of the metalized explosive formulations. First,

Table 4.2: Material properties for the explosive and metal components.The explosive properties are representative of the HMX and the metal properties are representative of aluminum.

Parameter	Explosive	Metal	Units
Young's Modulus, E	24.0	70.0	GPa
Bulk Modulus, K	13.3	77.7	GPa
Poisson's Ratio, ν	0.2	0.35	—
Initial Density, ρ_0	1903.0	2700.0	kg/m^3
Initial Temperature, T_0	300	300	K
Initial Yield Strength, τ_o	0.37	0.25	GPa
Longitudinal Sound Speed, C_l	2750	6470	m/s
Acoustic Impedance, Z	7.1	16.29	MPa.s/m
Friction Coefficient, μ	0.25	0.25	—
Viscosity, γ	100	100	Pa-s
Hardening Modulus, h	0.0	0.0	—
Thermal Conductivity, k_T	0.5	237.0	W/m-K
Specific Heat, c_v	1500.0	900.0	J/kg-K
Thermal Expansion Coefficient, α	1.0×10^{-5}	2.22×10^{-5}	1/K

the acoustic impedance which is given by $Z = \rho_o C_l$, where ρ_o and C_l are the ambient material density and longitudinal acoustic speed, is significantly higher for the metal ($Z_{Al}/Z_{hmx} = 2.3$). Since the acoustic pressure scales with the acoustic impedance, it is reasonable to expect that the overall pressure within the ensemble increases with the inclusion of the metal. Second, the yield strength of the metal is lower than that of the explosive ($\tau_{o,m} = 0.25$, $\tau_{o,e} = 0.37$), therefore for a given impact speed, the metal may undergo more plastic deformation. Finally, the thermal conductivity in metal is significantly higher than that of the explosive ($K_{T,Al}/K_{T,hmx} = 474$), and this affects the partitioning of frictionally dissipated energy at explosive-metal contacts with surfaces. Based on Eq. 2.47, approximately 95% of frictionally dissipated energy at metal-explosive contacts will be absorbed by the metal which may lead to the suppression of hot-spot formation.

4.1.2 Validation

Figures 4.3(a) and (b) summarize the predicted Hugoniot curves for meso-structures A, B, and C in $\bar{P}$-U_p and D-U_p planes. Here U_p, and D correspond to the piston speed and the wave speeds respectively, and $\bar{P} = (\bar{P}_e\bar{\phi}_e + \bar{P}_m\bar{\phi}_m)/(\bar{\phi}_e + \bar{\phi}_m)$ represents the ef-

fective equilibrium mixture pressure behind the deformation wave. Here $\bar{P}_e$, $\bar{P}_m$ represent the effective explosive (HMX) and metal (Al) pressures respectively, and $\bar{\phi}_e$, $\bar{\phi}_m$ represent the effective explosive and metal volume fractions behind the deformation wave. For neat HMX, $\bar{P} = \bar{P}_e$. Also shown in these plots are the experimentally measured Hugoniots for neat HMX [51, 71]. Although the data are unavailable for the packing densities used in

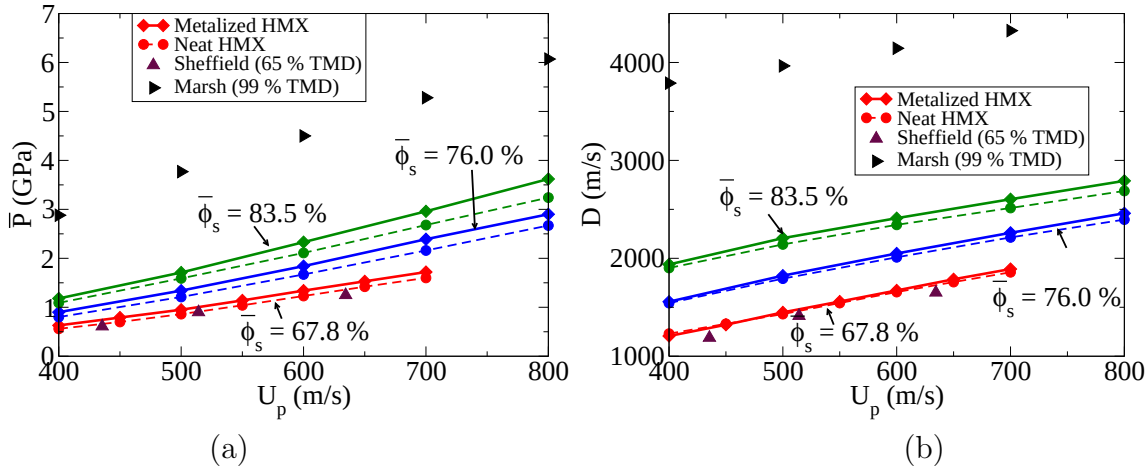

Figure 4.3: Predicted variations in effective wave end states (Hugoniot) as function of $\bar{\phi}_s$ and λ_m: (a)D-U_p; (b) $\bar{P}$-U_p.

this study, they provide a qualitative estimate of how the wavespeed and pressure vary with packing density. The experimental Hugoniot data from Sheffield [71], is for $\bar{\phi}_s = 65.5$ %, and therefore those values can be quantitatively compared to the predicted meso-scale values for meso-structure A with a packing density of $\bar{\phi}_s = 67.8$ %. In sheffield's experiments, a gas gun driver was used to obtain sustained shock loading conditions due to projectile impact. The sustained loading condition leads to the development of quasi-steady waves within the material. The advantage of gas gun drivers is that the velocity of the projectiles can be precisely controlled. The porous HMX material ($\bar{\phi}_s = 65.5$ %) with a thickness of ≈ 4 mm, was enclosed in a cell confined between a polychlorotrifluoroethylene (Kel-F) plastic front plate (Projectile impact face) and TPX back plate which has an acoustic impedance similar to the pressed HMX enabling the capture of stress waves more accurately. A schematic of the experimental set up is shown in Figure 4.4. The particle velocity and pressure gauges are

located at the front and back surface of HMX respectively. The compaction wavespeed D, is calculated by measuring the time taken for the compaction (transmitted) wave to traverse the compact thickness. The corresponding shock pressures are measured by the pressure gauges at the back surface of HMX. Additionally, the wave rise times were also obtained using the particle velocity gauges embedded within the HMX compact. In spite of the sim-

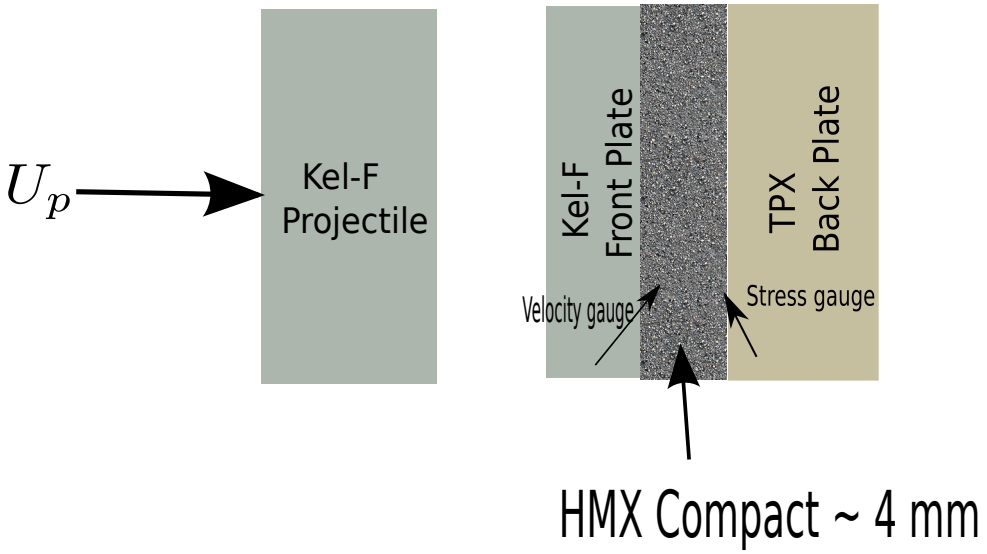

Figure 4.4: Schematic of the experiment performed by Sheffield et al. [72] to obtain Hugoniot curves and wave rise times for porous HMX with packing density of $\bar{\phi}_s = 65.5$ %.

plified physics, and differences between the ideal (2D) meso-structures used in this study, and the real (3D) meso-structures in experiments, the model predictions agree reasonably well with experiments. In Figure 4.3(a) it is observed that the inclusion of metal increases the effective pressure $\bar{P}$ within the material for all the meso-structures. As discussed before, this is due to the high bulk modulus K of the metal. The increased pressure within the material, facilitates larger deformation of explosive particles. In Figure 4.3(b), an increase in packing density and/or metal mass fraction fraction results in an increase in D within the material. Due to it's high bulk modulus, the metal particles have lower compressibility and therefore, transmit normal stresses within the material more efficiently leading to an overall increase in D. Since we use a rate dependent plasticity model in this study, variations in D can

also result in larger plastic deformation of explosive particles within the compaction wave. The functional relationship (curve fits) between $\bar{P}$ and U_p, and D and U_p can potentially be incorporated in establishing ignition manifolds for various meso-structures considered in this study. Tables A.1 and A.2 in Appendix A lists these curve fit parameters

Figures 4.5(a), (b) and (c) illustrate the variations in the effective explosive component plastic work $\bar{W}_{pe}$ as a function of U_p, $\bar{P}U_p$, and $\bar{P}$ respectively. Here, the product of $\bar{P}U_p$ is representative of the power input. An explosive mixture is considered more sensitive if most of the energy input to the explosive through external stimuli such as piston/projectile impact is converted into thermal energy within the material due to various dissipative mechanisms. Different meso-structures offer vastly different resistances to compaction due to variations in their granular bed morphologies. The variations in compaction resistance basically translates to differences in effective pressures between the materials as shown in Figure 4.3(a). Therefore, different amounts of power input is required to maintain identical piston speeds across these materials. The effective pressures within the material is an extremely important parameter since, most of the experimental observations indicate a strong correlation between the macro-scale detonation response and the shock pressure. Hence, most theoretical burn models employ a pressure dependent burn rate formulation to match experimentally observed run to detonation or time to detonation values. Details on this will be discussed in the following section. Figures 4.5(a) and (b) both indicate that an increase in porosity $(1-\bar{\phi}_s)$ and/or metal content λ_m results in increased plastic dissipation within the explosive component across the entire range of wave strengths . While an increase in porosity results in larger dissipation in explosives due to plastic pore collapse, an increase in λ_m for a fixed initial packing density results in larger plasticity within the explosive due to larger pressure within the material which facilitates compaction. Similar observations are also made in Figure 4.5(c) where $\bar{W}_{pe}$ is expressed as a function of $\bar{P}$. It is important to note that in Figure 4.5(b) and (c), the variations in $\bar{W}_{pe}$ are expressed as function of the power input and effective pressure on a log-log plot. Because the functional relationship between $\bar{W}_{pe}$, and

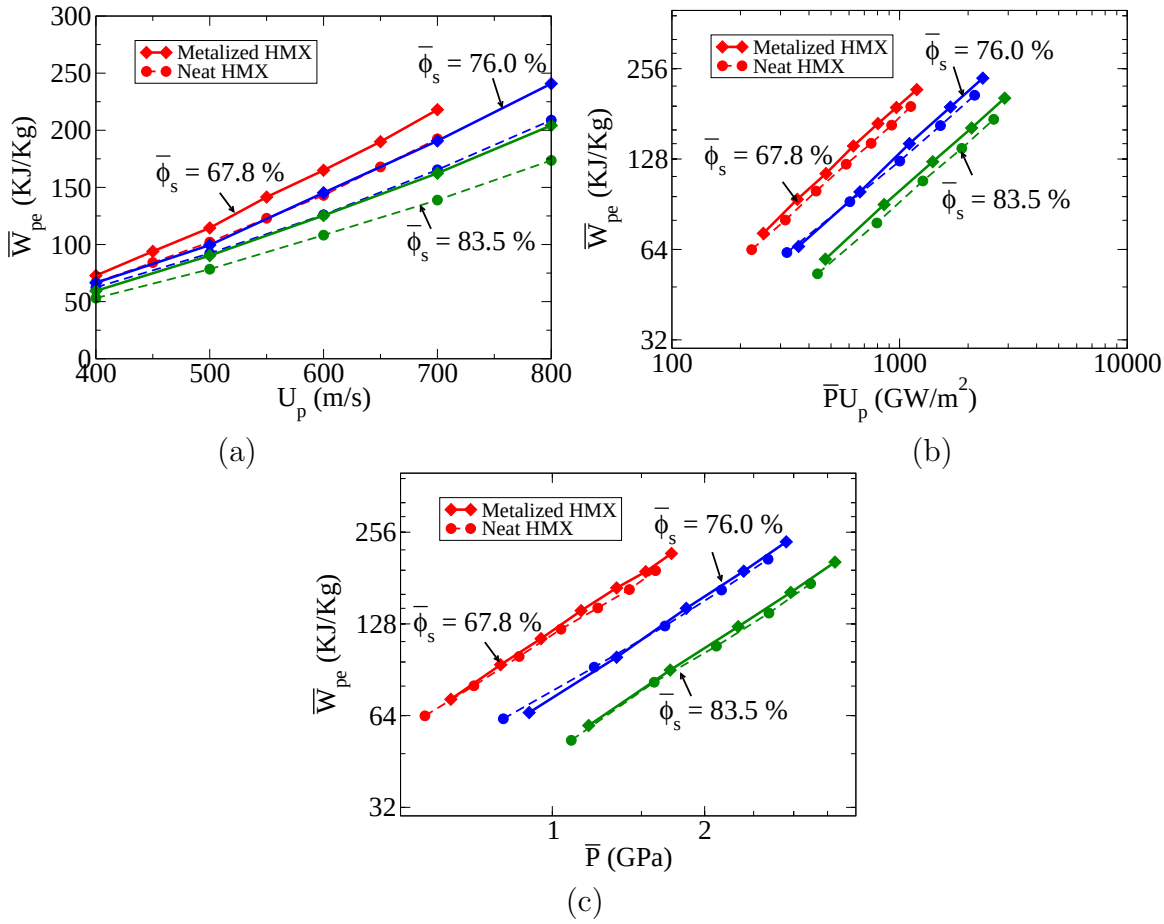

Figure 4.5: Predicted variations in the effective plastic work of the explosive component as a function of $\bar{\phi}_s$, and λ_m: (a)$\bar{W}_{pe}$-U_p; (b) $\bar{W}_{pe}$-$\bar{P}U_p$; (c) $\bar{W}_{pe}$-$\bar{P}$.

$\bar{P}U_p$, and $\bar{W}_{pe}$ and $\bar{P}$ are linear on a log-log plot, it is plausible to express their relationship using a power law. The best parameter estimates for the power law fits are shown in Table A.3 in Appendix A. Experiments show a power law relation between run to detonation or time to detonation distance and the corresponding shock pressure/energy input. Because the bulk plastic work exhibits similar qualitative trends, it may be possible to incorporate these Hugoniot relations for plastic work in macro-scale ignition and growth models.

Another important macro-scale impact/shock response variable routinely measured in experiments are the wave rise times. Wave rise times are indicative of the deformation wave thickness. Because the shock sensitivity of explosives is implicitly coupled with the spatial and/or temporal scales of shock interaction with the material heterogeneities, wave rise times are useful quantities in explaining the macro-scale shock response of the material. There is

an ambiguity in defining the meaning of the wave rise time. In this study, wave rise time is defined as the time taken for a generic variable $\bar{\Phi}_i$ within the deformation wave to vary from 5 % to 95 % of its effective equilibrium value behind the deformation wave. The wave rise times shown above are estimated based on the 1-D spatial wave profiles of the axial velocity component V_x. The equilibrium values for the axial velocity component V_x are 0 (initial state) and U_p (end state). Numerical experiments using 1-D spatial wave profiles of other important variables such as pressure, and plastic work indicated similar wave rise times. From Figure 4.6, it is evident that an increase in packing density and/or impact speed reduces the wave rise times indicating a decrease in the thickness of the deformation wave. Predictions for the wave rise times agree reasonably well with the experimentally measured values for porous HMX [72] as a function of piston impact speed for materials with comparable effective packing densities. For $U_p > 600$ m/s, the rise times are found to be minimally affected by an increase in U_p. This is again consistent with the trends predicted by Sheffield. The inclusion of metal is found to have a negligible affect on the wave thickness. Along with $\bar{\phi}_s$, the wave rise time/thickness is influenced by the choice of the plastic viscosity parameter γ. In this analysis, identical values of γ are used for both HMX and Al particles $\gamma = 100$ *Pa-s*. This value was chosen based on the work of Conley and Benson [21], who performed meso-scale simulations on neat granular HMX with packing densities in the range of $0.65 \leq \bar{\phi}_s \leq 0.75$ and compared their wave thickness to experimentally observed values. Parametric studies performed by Panchadhara [61] on neat HMX meso-structures similar to the ones used here, suggested that the wave thickness varied only marginally ($< 10\%$) by varying γ in the range of $10 \leq \gamma \leq 100$ *Pa-s*.

4.2 Hot-Spot Statistics

This section highlights the effects of initial packing density ($\bar{\phi}_s$) and composition ($0.0 \leq \lambda_m \leq 0.2$) on hot-spot fields. In this analysis, hot-spot refers to a region of the explosive (HMX) material having temperature $T \geq T_{th}$, where T_{th} is the threshold temperature with a magnitude of 500 K. In aluminized HMX formulations, hot-spots within HMX are important

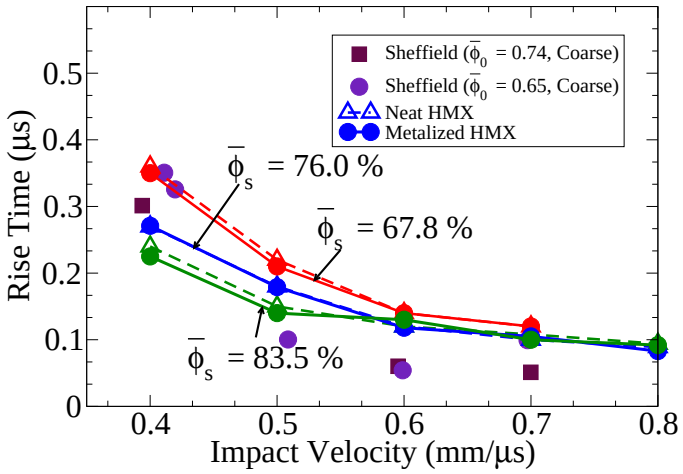

Figure 4.6: Wave rise times for meso-structures A-C as a function of piston speed.

in establishing its shock sensitivity because the rate of energy release in HMX is substantially larger compared to Al, though the overall specific energy content is higher in the metal. Therefore, explosive hot-spots that react behind the deformation wave quickly produce large amounts of high pressure gases which can further accelerate the combustion process in the unreacted material. The choice of T_{th} is motivated by the fact that this temperature is close to the β-δ phase transition temperature of HMX [42], and therefore this value reasonably indicates the onset of chemical activity. However, sustained combustion of a hot-spot is dependent on not just its intensity (temperature) but various factors such as the hot-spot size, shape, proximity, and boundary/surrounding conditions. Hot-spot size, shape are important for the onset of reaction because for a given intensity, larger hot-spots tend to possess higher thermal inertia and therefore these hot-spots are likely to react before thermal conduction can suppress the reaction. Similarly hot-spots with larger surface area are more prone to conductive losses. Hot-spot proximity is important in terms of hot-spot growth and coalescence. If a few discrete reactive hot-spots are clustered within a region, there is a higher probability that these hot-spots can thermally interact and grow into larger more intense hot-spots. This may eventually result in a global ignition event due to unsustained combustion.

The main focus of this chapter is to investigate the effects of metal ($\lambda_m = 0.2$) on hot-spot fields in meso-structures A-C with varying $\bar{\phi}_s$ (Figure 4.1). The corresponding hot-spot fields in neat granular HMX were characterized in [30, 31] for a narrow range of impact speeds (U_p = 300-500 m/s), and their analysis is extended in this study for metalized explosive formulations corresponding to piston speeds in the range of U_p = 400-900 m/s. This range of piston speed results in substantial deformation of explosive particles since the effective pressures within the material are much larger than the HMX yield strength. Because plastic dissipation is one of the dominant dissipative mechanisms in this study, the range of piston speeds considered here result in large number of hot-spots within the material, and therefore the statistical representation of these fields are more meaningful. Emphasis is placed on identifying variations in hot-spot properties that may be useful in the development of macro-scale ignition and growth models which investigate the macroscopic shock response of the explosives based on hot-spot data [46]. The layout of the section is as follows. First, a brief overview of the common macro-scale ignition and growth models used within the energetics community are presented. Second, discussions on the statistical technique used to characterize the relevant hot-spot properties are presented. A comprehensive discussion on the statistical technique and the image processing method can be found in [30, 31]. Finally, predictions for the overall and critical hot-spot fields are provided. As discussed before, critical hot-spots refers to those hot-spots that possess enough thermal inertia to overcome acoustic expansion and thermal conductive losses. In this study, critical hot-spots are identified based on the analysis by [75] using the joint distributions of the hot-spot size and intensity as discussed later in section 4.6. Critical hot-spots are the ignition sites within the material where the reaction occurs first. However whether the reaction in few critical hot-spots would eventually lead to a macro-scale detonation event is governed by hot-spot growth and coalescence rates which are dependent on the details of overall hot-spot fields.

4.3 Ignition and Growth Models

It is well established that shock initiation of heterogeneous explosives is due to the formation and subsequent reaction of hot-spots resulting from various dissipative mechanisms within the shock/deformation wave because the bulk temperatures measured in experiments are low for onset of any reaction within these materials. Many experiments [57, 72, 76] have been conducted to correlate the shock pressures/power input and time to detonation for a number of explosives with varying initial meso-structures. Typically, the run distance to detonation and the corresponding wave strength exhibit a power law relationship. Models based on the concept of hot-spot ignition and growth have been able to quantitatively match experimentally observed run distance to detonation for commonly used explosives under various loading conditions [46]. However, these ignition and growth models contain a number of parameters that explicitly and/or implicitly depend on certain aspects of the hot-spot such as its number density, volume fraction, intensity, size, shape, and proximity. Experimental measurements of hot-spot features is difficult due to the small spatial and temporal scales associated with it. The basic essence of the ignition and growth models is that while the ignition of the material occurs at localized hot-spots, occurrence of a global ignition event within a material is controlled by the growth and coalescence of these reactive hot-spots. Because it is difficult to characterize the hot-spot fields experimentally, inert meso-scale models can be used to provide statistical information on hot-spot features that control the values of the parameters used in these models.

Lee and Tarver [46] developed a theoretical framework to explain shock initiation of numerous explosives subjected to different loading conditions. Their model was based on the assumption that a small fraction of the explosive is ignited by the passage of the shock front, and that the reaction rate is primarily controlled by the pressure within the material, and the surface area of the hot-spots. Additionally they argued that the explosive material may be consumed rapidly based on the number of hot-spots formed behind the lead shock wave. Equation 4.6, provides a simple mathematical description of the ignition and growth

model used by Lee and Tarver,

$$\frac{\partial F}{\partial t} = I(1-F)^x \eta^r + G(1-F)^x F^y p^z, \tag{4.5}$$

$$\eta = \frac{V_0}{V_1} - 1. \tag{4.6}$$

In Eqn. 4.6, F represents the fraction of explosive that has reacted, t is the time, V_0 is the specific volume of the unshocked explosive, V_1 is the specific volume of the shocked explosive, and p is the pressure of the shock. I, x, r, G, y and z are empirical constants that are used to fit experimental data. Tarver and Lee argued that some of these parameters were dependent on certain features of the hot-spot fields within the explosive. For example, parameter G accounts for the ratio of the surface area to volume of the hot-spots. The hot-spot fields from the meso-scale models can provide statistical distributions of hot-spot surface area to volume ratios which can be incorporated in this model. Similarly, Lee and Tarver argued that different values of r could implicitly describe the different hot-spot formation mechanisms such as viscoplasticity, microjetting, or friction. Using this simplified physical model, they were able to match experimentally determined run distance to detonation for various explosive mixtures undergoing sustained shock loading (quasi-steady waves).

Menikoff and Shaw [55] argued that the burn rate of ignition and growth models should incorporate three meso-scale features to accurately predict macro-scale material response. These meso-scale features were: (1) the density of reactive hot-spots; (2) the growth of these reactive hot-spots which are dependent on the local deflagration speeds; (3) the proximity of these burn centers that allow for the overlap of the deflagration wavelets from the neighboring burn centers. Mathematically, they formulated the burn rate R as

$$R(t, P_s, P) = g(s(t - t_s, P_s, P)) \tag{4.7}$$

where P is the local pressure, P_s is the incident shock pressure, t is the time, t_s is the time at which shock arrives at point x. Here g represents the reaction scale function, and

s represents the scaled burn center reaction length. Burn centers in this study refers to the critical hot-spots. Menikoff and Lee argued that s is a strong function of the hot-spot proximity and number density (Number of hot-spots within a unit area). Both of these properties can be estimated from the meso-scale simulations. Using their analysis, Menikoff and Lee were able to illustrate that the average burn rate within the explosive was dependent on distribution of the burn centers within the material, and predictions made using their model agreed with shock initiation data for commonly used plastic bonded explosive PBX 9502. The work presented in this dissertation represents a preliminary step in developing a framework wherein meso-scale hot-spot features can be coupled with macro-scale ignition and growth models to better predict shock sensitivity of explosives.

4.4 Hot-Spot Statistics

Granular HEs are random heterogeneous materials in that any sample of the material is a realization of a specific random or stochastic process [78]. Statistically, an *ensemble* refers to a collection of all possible realizations of a random heterogeneous material. Mathematically, if ξ is considered to be the outcome space corresponding to an ensemble, and $\omega \in \xi$ is a specific event corresponding to a single material realization; then the temperature field for a given material realization ω can be expressed as $T = T(x, t, \omega, U_p, \bar{P})$. Here, x refers to an arbitrary location within the computational domain, while t, U_p, and $\bar{P}$ correspond to the time, piston speed, and effective pressure behind the deformation wave respectively. For a complete statistical description, it is essential to analyze the hot-spot temperature fields for every material realization $\omega \in \xi$ and subsequently average both spatially and temporally over all realizations. However, this can be computationally expensive, and therefore in their statistical characterization of hot-spot fields for neat HMX [30, 31], an assumption of ergodicity was made. Ergodicity with respect to granular materials means that all possible states/realizations will be encountered in a single realization if the spatial domain is infinite. Though, the spatial domains considered in [30, 31] were finite, it was argued that for large ensembles containing thousands of particles (4000) similar to the ones in this study, this

assumption is reasonable. However, no validation supporting the assumption was provided. Chapter 6 tries to address the validity of the ergodicity assumption. In this study, hot-spot fields are chosen to be temporally static within the explosive component because thermal conduction is negligible for the time-scales of our simulations.

In the remainder of this section, brief discussions quantifying hot-spot morphology and intensity that are important for localized ignition, and hot-spot spatial proximity measures that are important for hot-spot growth and coalescence are presented. Here, hot-spot morphology refers to its size and shape, and hot-spot intensity refers to various measures of hot-spot temperatures. Emphasis is also placed on hot-spot volumetric properties such as number density and volume fraction because they routinely appear either explicitly or implicitly in macro-scale ignition and growth models [46, 55]. Variations in hot-spot volumetric properties are expressed both as a function of piston speed and effective power which is a measure of the wave strength. Because this work represents an extension of the work performed by [31, 30] a detailed discussion on the image processing technique and the relevant statistical methods used can be found in [31, 30], and only the most relevant topics are discussed here.

4.4.1 Hot-Spot Morphology and Intensity

Hot-spot morphologies and intensities are characterized using probability density functions (PDFs) $h(\varepsilon, x)$ where ε represents various hot-spot features such as size, intensity, surface area, shape etc. The quantity $h(\varepsilon, x)d\varepsilon$ gives the probability that a hot-spot at a particular location will have an intensity/morphology in the range of ε to $d\varepsilon$ for a given piston speed. The corresponding cumulative distribution functions (CDFs) are obtained by integrating the normalized PDFs as

$$H(\varepsilon, x) = \int_0^{\varepsilon} h(\varepsilon, x)d\varepsilon, \tag{4.8}$$

where $H(\infty, x) = 1$.

The spatial temperature fields within hot-spots are complex (Figure 4.7), and therefore cannot be characterized by a single temperature. In this study, the intensity of a hot-spot is characterized by its mean temperature $\bar{T}_{HS}$, and peak temperature $\hat{T}_{HS}$. The mean hot-spot temperatures are the mass-weighted average temperatures within the hot-spot similar to mass weighted average expression in Eqn. 4.1. However, the changes in densities are assumed to be negligible within each hot-spot, and therefore the mass weighted average reduces to an area weighted average. The ignition probability of a given hot-spot will depend on its temperature field, where ignition is likely to begin at the location of peak temperature and spread outwards towards the cooler regions of the hot-spots. Hence, the peak hot-spot temperature may be critical in establishing a local ignition criterion whereas the mean temperature may influence the rate at which the hot-spot mass is consumed due to combustion since larger temperature gradients next to the reactive hot-spots may result in locally high deflagration speeds. Hot-spot size in this study refers to its area. Along with hot-spot temperature, size is an important factor in establishing the critical temperature at which sustained reaction will result [75].

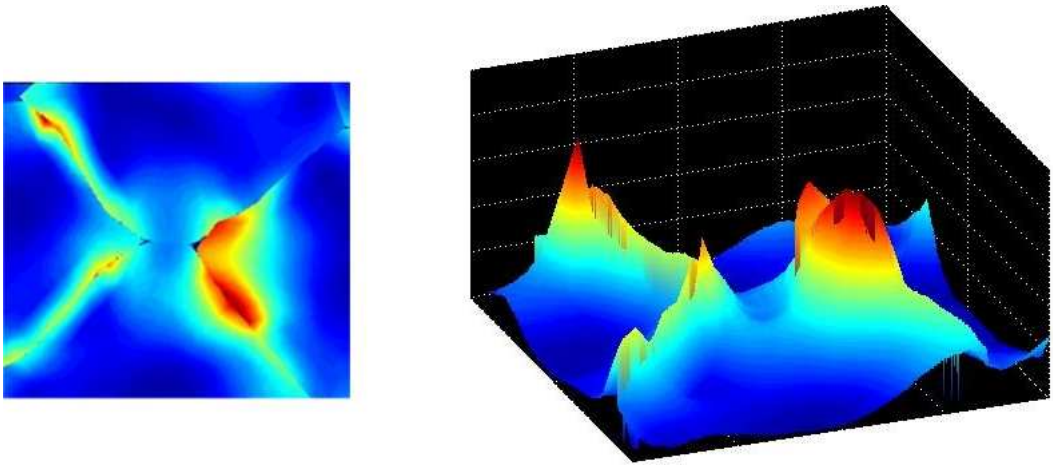

Figure 4.7: Illustration to show the spatially complex temperature fields within hot-spots [30].

Another important hot-spot feature that can affect hot-spot ignition is its shape. Hot-spots with larger surface area to volume ratios generally experience more conductive losses, however if they possess enough thermal inertia to overcome conductive losses, they may

enhance combustion within the material due to their larger burn surface area. In this study, hot-spot shapes can be characterized using eccentricity $\mu = 1 - \epsilon$ and area to perimeter ratio ζ. Eccentricity is the ratio of the distance between the foci of an ellipse having the same second moment as the hot-spot area and its major axis length. Eccentricity $\epsilon = 0$ represents a circle while $\epsilon = 1$ represents a line. Generalized Pareto Distributions (GPDs) are used to describe the marginal PDFs for hot-spot size, eccentricity and intensity. The PDFs for a GPD are given by

$$f(x) = \frac{1}{\sigma}(1 + k\frac{x-\theta}{\sigma})^{(-1-1/k)} \tag{4.9}$$

where $k \neq 0$ is the shape parameter, σ is the scale parameter, and θ is the threshold parameter. Here, x is the hot-spot feature of interest.

GPDs are generally used to fit distributions of extreme values, which are exceedances beyond the prescribed threshold. Since hot-spots in this study correspond to the tail of the temperature distribution, they may be interpreted as extreme values of a temperature threshold. Difficulty in using GPD involves specifying the threshold θ. In this analysis the threshold value for hot-spot intensity is chosen as $\theta_T = 500$ K, and the threshold for the hot-spot size is chosen as the area of approximately 3-5 finite elements because any length scale lower than 3-5 FE is likely unresolved within the context of these simulations ($\theta_A = 2.9$ μm^2). In terms of the image processing technique employed in this study, it translate to eliminating any closed hot-spot region that contains fewer than 130-180 pixels. In all of the hot-spot analysis presented in this work, identical thresholds for hot-spot temperature and area were used. Detailed discussion on the effects of GPD parameters can be found in [30, 31].

The hot-spot area to perimeter ratios ζ are described using Generalized Extreme Value (GEV) distributions. Similar to GPD, the GEV distributions are used in extreme value theory to model exceedances. The GEV distribution function is mathematically expressed as

$$f(x) = \frac{1}{\sigma}exp(-(1 + k(\frac{x-\mu}{\sigma})^{-(1/k)})(1 + k(\frac{x-\mu}{\sigma}))^{-k-1/k}. \tag{4.10}$$

Here, μ represents the location parameter, σ represents the scale parameter, and k is the shape parameter.

4.4.2 Hot-Spot Proximity

The spatial proximity of hot-spots can be characterized based on the nearest neighbor distances [30, 31]. The nearest neighbor distances are commonly used to investigate the spatial dependency between events occurring within a region. To this end, two measures for quantifying hot-spot proximity distributions are used. First, a hot-spot surface-to-surface distance $r_{s,s}$ which represents the distance between the surface of a hot-spot and its closest neighbor. Second, a point to surface distance $r_{p,s}$ which is the minimum distance between a randomly selected point in the domain and the surface of the closest hot-spot. The random point in the domain is chosen such that it does not lie within the boundaries of any hot-spots. Similar to hot-spot size and intensity, the hot-spot proximity distributions are characterized using PDFs ($P_{r,s}$, $P_{p,s}$). The PDFs for hot-spot proximity are well defined by Weibull distribution (WBL) which is given by

$$f(x) = \frac{B}{A}(\frac{x}{A})^{B-1}e^{(-x/A)^B}. \tag{4.11}$$

Here shape parameters A and B have similar interpretation as σ and k in the GPD distribution. The two measures of hot-spot proximity provide information on spatial proximity and clustering of hot-spots. Figure 4.8 shows the schematic for the $r_{s,s}$ and $r_{p,s}$ measurements. Hot-spot clustering will result in $P_{s,s}$ values increasing steeply for small values of r (distance); however on the contrary $P_{p,s}$ will plateau for small values of r and rise sharply for with an increase in r. For a homogeneous hot-spot field, the $P_{s,s}$ and $P_{p,s}$ distributions collapse into a single curve. Characterizing the spatial proximity of hot-spots is important in that they are likely to affect hot-spot growth and coalescence rates which may be crucial in establishing a global ignition event.

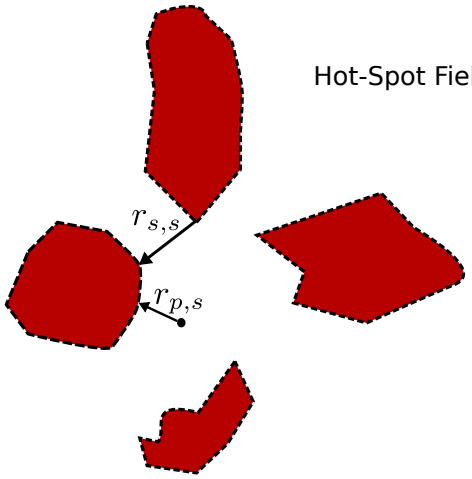

Figure 4.8: Schematic illustrating surface-surface $r_{s,s}$ and point-to-surface $r_{p,s}$ nearest neighbor distances used to quantify hot-spot proximity

4.4.3 Volumetric Quantities

Volumetric properties such as hot-spot number density, and volume fraction routinely appear as parameters in macro-scale ignition and growth models [55] which account for the fraction of explosive material initially ignited behind a deformation wave. As such it is important to characterize how these properties vary with changes in the meso-structure. In this study, the volumetric properties are primarily computed in two ways. One is by computing these properties based on the overall area of the computational domain, and the other is to compute the properties based on the explosive component area. If N is the total number of hot-spots in the domain, then the total hot-spot number density and volume fraction are given by

$$\phi_{HS} = \frac{\sum_{i=1}^{N} \hat{A}_i}{A_T}, \quad n_{HS} = \frac{N}{A_T}, \tag{4.12}$$

where A_T is the total area of the domain, and $\hat{A}_i$ is the area of the i^{th} hot-spot. Similarly the number density and volume fractions can be computed computed based on the phase/component area as

$$\tilde{\phi}_{HS} = \frac{\sum_{i=1}^{N} \hat{A}_i}{A_e}, \quad \tilde{n}_{HS} = \frac{N}{A_e}, \tag{4.13}$$

where A_e is the total area of explosive particles. The two measures of volumetric properties highlight different aspects of metal inclusion on shock sensitivity of the material. In principle

it is possible to compute these properties locally within a region δA to estimate their spatial variation; however it is likely that the computed values will be sensitive to the size and shape of δA. Once again, the hot-spot volumetric properties are expressed in this study as a function of the piston speed U_p, power input $\bar{P}U_p$, and $\bar{P}$ for all the meso-structures. Here $\bar{P}$ represents the effective explosive component pressure within the material. As mentioned earlier, the sensitivity of explosives is typically measured in experiments as a function of input energy/shock pressure. Also, as seen in section 4.3, the ignition and growth models routinely cast their effective burn rate as a function of the effective pressures. Hence, expressing the volumetric quantities as a function of U_p, $\bar{P}U_p$ and $\bar{P}$ will provide information that is useful for ignition modeling and/or estimating ignition manifolds.

4.5 Overall Hot-spot Fields

Figure 4.9 illustrates the complex hot-spot fields behind the deformation wave in meso-structures A and C corresponding to $U_p = 700$ m/s. It is evident from the contours that the resulting hot-spots fields consists of hot-spots with varying sizes, shapes, intensity, and proximity. Larger, more closely placed hot-spots are observed in meso-structure A compared to C because of significant dissipation within the more porous material resulting from plastic pore collapse. This observation is consistent with the Hugoniot plots which show larger effective plastic work within the explosive component in meso-structure A compared to meso-structures B and C.

4.5.1 Hot-spot Morphology and Intensity

Figure 4.10 shows the PDFs for hot-spot size described using GPD for meso-structures A and C as a function of U_p. From Figures. 4.10(a) and (b), the following observations are noteworthy. First, an increase in U_p and/or porosity $(1 - \bar{\phi}_s)$ produces larger hot-spots due to higher inelastic deformation within the particles. Second, at $U_p = 400$ m/s, the inclusion of metal is found to have a negligible effect on the hot-spot size distributions due to relatively weak deformation wave that results in hot-spots being confined to the particle boundaries as a consequence of localized plasticity and friction. However, at $U_p = 700$ m/s,

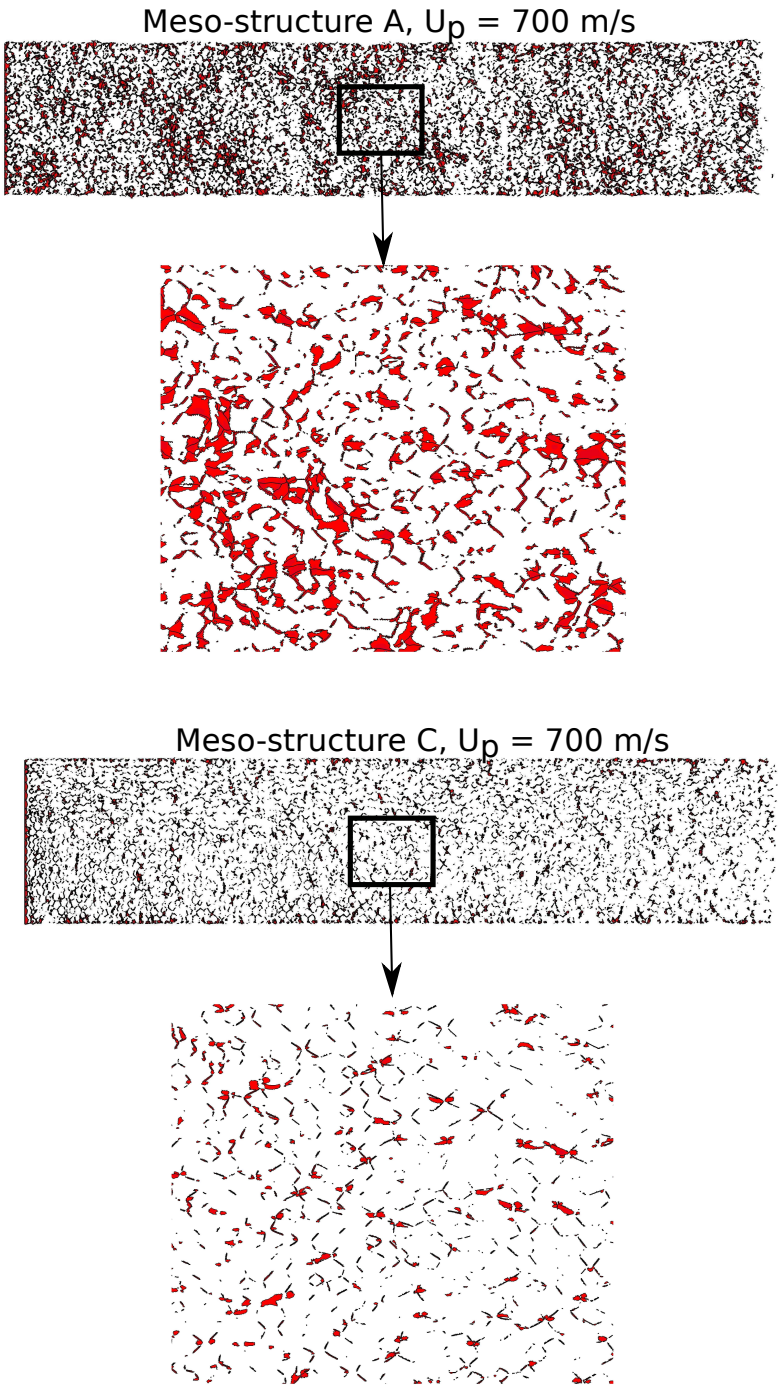

Figure 4.9: Contours of the resulting hot-spot fields in meso-structures A and C at $U_p = 700$ m/s.

the average hot-spot size $\bar{A}$ is found to increase noticeably in metalized HMX formulations. The increase in average hot-spot size is because of larger inelastic deformation of explosive particles resulting from pressure enhanced compaction. Similar observations can also be

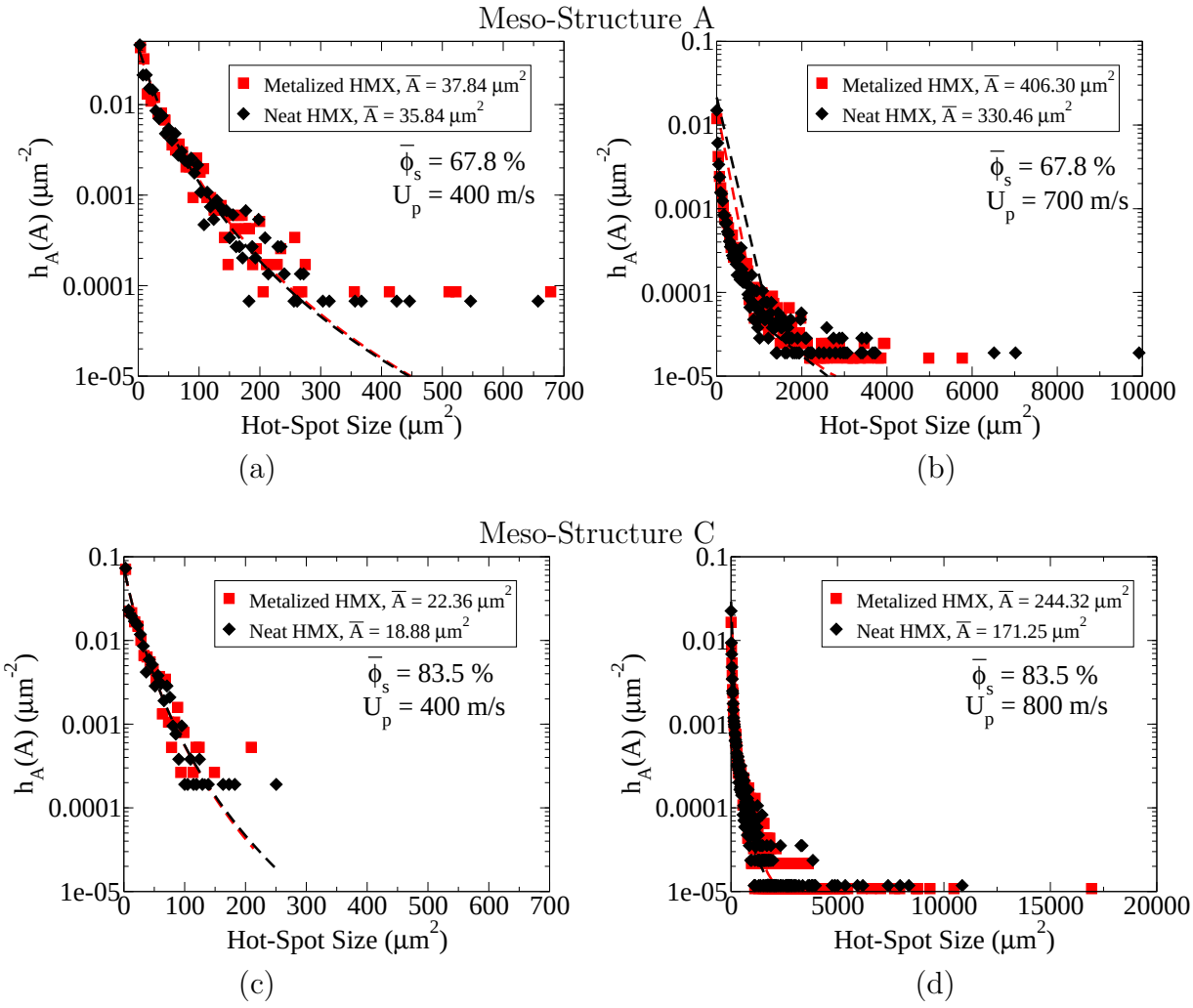

Figure 4.10: Predicted GPD PDFs for hot-spot area in explosive component for meso-structures A and C with $\lambda_m = 0.2$: (a) Meso-structure A ($U_p = 400$ m/s); (b) Meso-structure A ($U_p = 700$ m/s); (c) Meso-structure C ($U_p = 400$ m/s); (d) Meso-structure C ($U_p = 800$ m/s).

made for meso-structure C as shown in Figures. 4.10(c) and (d). In Figure 4.10(d), for $U_p = 800$ m/s, the largest hot-spot size is approximately 15000 μm^2 which is approximately 3 particle diameters indicating hot-spot agglomeration.

Figures 4.11(a) and (b) illustrate the PDFs described by GPD for mean hot-spot temperatures $\bar{T}_{HS}$ in meso-structure A corresponding to impact speeds of $U_p = 400$ and 700 m/s respectively. In Figures. 4.11(a) and (b), only marginal differences in mean hot-spot temperatures are predicted between metalized and neat explosive formulations. Typically larger inelastic deformation in the explosive due to the inclusion of metal should result in higher

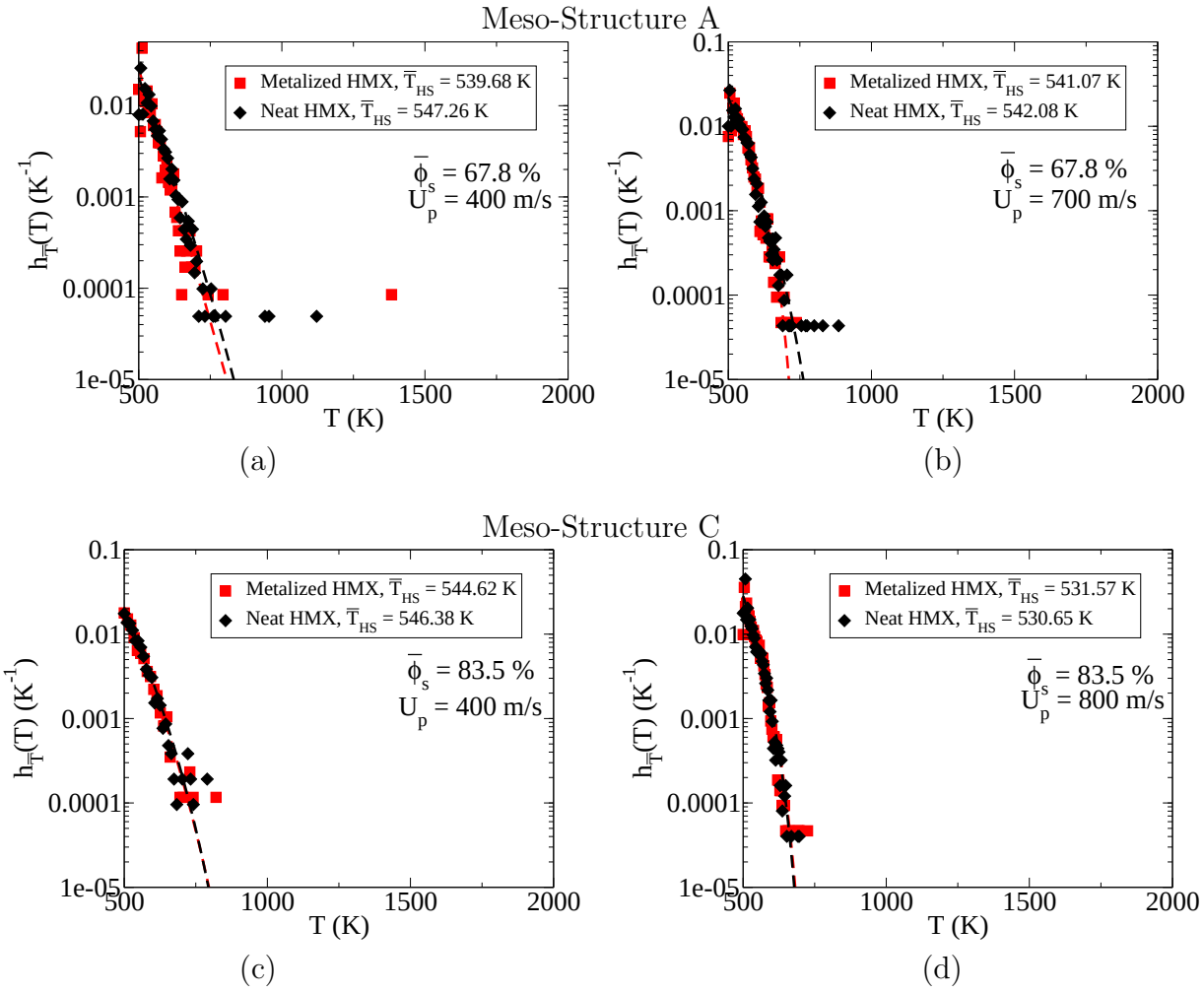

Figure 4.11: Predicted GPD PDFs for mean hot-spot temperature $\bar{T}_{HS}$ in explosive component for meso-structures A and C with $\lambda_m = 0.2$: (a) Meso-structure A ($U_p = 400$ m/s); (b) Meso-structure A ($U_p = 700$ m/s); (c) Meso-structure C ($U_p = 400$ m/s); (d) Meso-structure C ($U_p = 800$ m/s).

$\bar{T}_{HS}$. However, inclusion of metal and/or an increase in piston speed is found to influence $\bar{T}_{HS}$ marginally. The counter intuitive prediction is a consequence of more hot-spots heated to temperatures slightly above the threshold ($T_{th} = 500$ K) and therefore this results in lower mean temperature values due to the inclusion of metal and/or an increase in piston speed. Similar qualitative observations are also made for mean hot-spot temperatures in meso-structure C (Figures. 4.11(c) and (d)). It is important to note that while meso-structure A consists of a majority of hexagonal particles, meso-structure C is entirely made up of circular particles. Since, only marginal differences are predicted in the hot-spot intensities between

the meso-structures, it is reasonable to presume that minor variations in particle shape plays an insignificant role in the hot-spot statistics, and that most of the observed variations in the hot-spot morphology, intensity, and shape are due to porosity and composition. It is possible that if real meso-structures are incorporated within the model, a noticeable change in hot-spot fields could be observed due to large variations in particle shapes. However, resolving the boundaries of these particles to accurately capture the relevant dissipative mechanisms such as plastic grooving would require considerable computational resources. Additionally, for the Lagrangian technique used in this study, significant numerical instabilities may arise due to stress concentrations at the sharp corners of these particles leading to severe mesh-distortion issues which further restricts the range of wave-strengths that one could simulate.

Peak hot-spot temperature $\hat{T}_{HS}$ distributions are shown in Figure 4.12. The predictions for $\hat{T}_{HS}$ are found to be qualitatively similar to mean hot-spot temperature $\bar{T}_{HS}$ distributions. On an average, a decrease in $\bar{\phi}_s$ and/or an increase in piston speed is found to increase the peak hot-spot temperature due to enhanced dissipation at the particle contact interfaces.

Hot-spot shape is another important parameter in determining whether a local ignition event can transition to a global ignition/detonation event. Hot-spots with larger burn surface area are more likely to increase the burn rate whereas it is also possible that conductive effects can quench these hot-spots before the onset of chemical activity. In the ignition and growth model proposed by Lee and Tarver [46], reaction growth rates were found to be sensitive to the surface area/volume ratio. Figures 4.13(a) and (b) provide GEV distributions for the hot-spot area-to-perimeter ratio ζ in meso-structure A corresponding to $U_p = 400$ and 700 m/s. In Figures 4.13(a) negligible differences are predicted in the PDFs between the metalized and neat meso-structures. Also, the average magnitudes of ζ indicate highly eccentric hot-spots at $U_p = 400$ m/s due to localized plastic and frictional heating confined to the particle boundaries. In Figure 4.13(b), metal addition is found to increase the average value of ζ due to the formation of larger hot-spots. Based on the variations in predicted

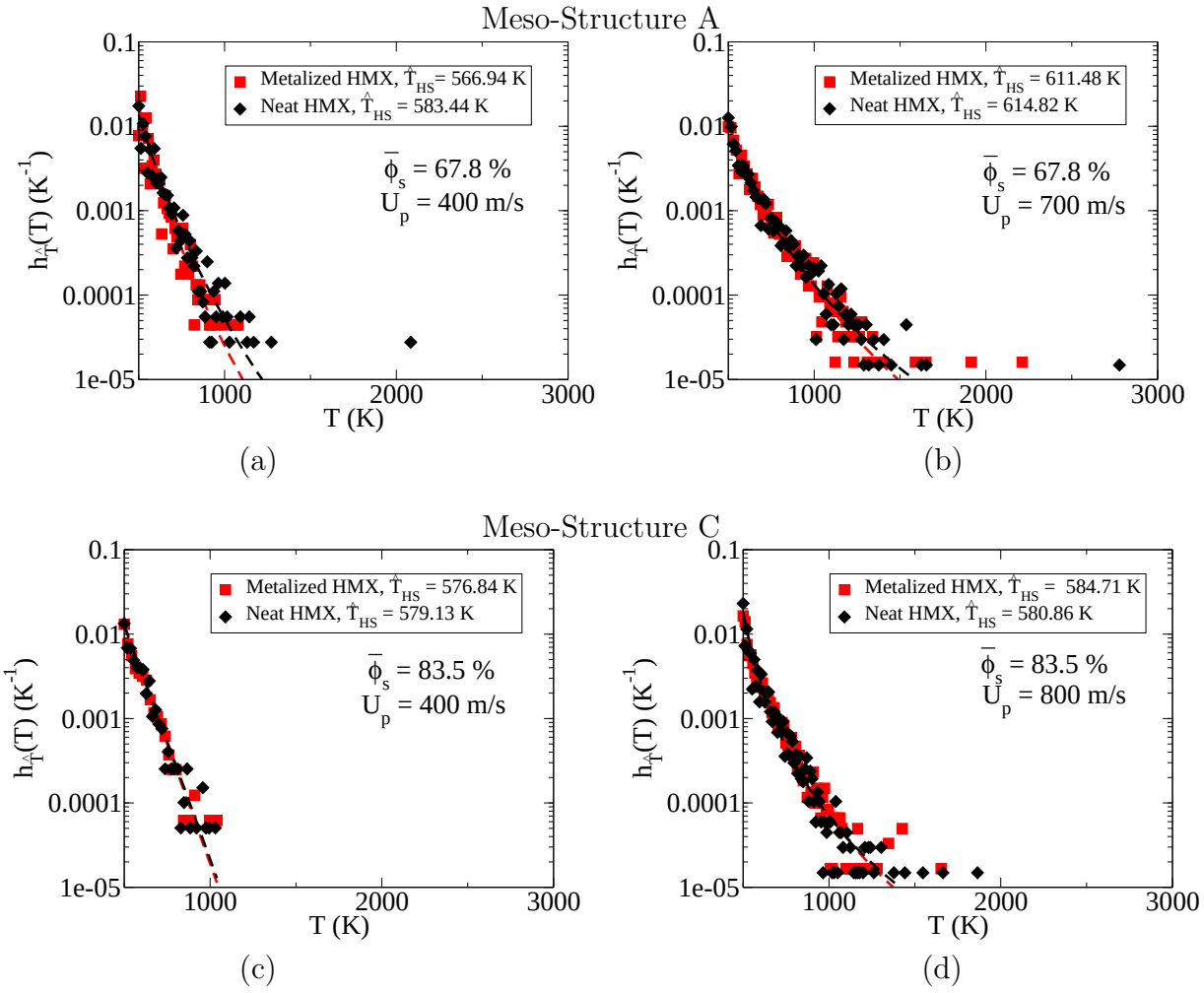

Figure 4.12: Predicted GPD PDFs for peak hot-spot temperature $\hat{T}_{HS}$ in explosive component for meso-structures A and C with $\lambda_m = 0.2$: (a) Meso-structure A ($U_p = 400$ m/s); (b) Meso-structure A ($U_p = 700$ m/s); (c) Meso-structure C ($U_p = 400$ m/s); (d) Meso-structure C ($U_p = 800$ m/s).

hot-spot shapes, it is plausible to identify the dissipative mechanism responsible for hot-spot formation with friction/localized plasticity leading to more eccentric hot-spots while significant plasticity leads to a decrease in hot-spot eccentricity. Figures 4.13(c) and (d) illustrate similar qualitative trends in meso-structure C with $U_p = 400$ m/s leading to highly eccentric hot-spots and $U_p = 800$ m/s resulting in larger hot-spots within the metalized explosive component.

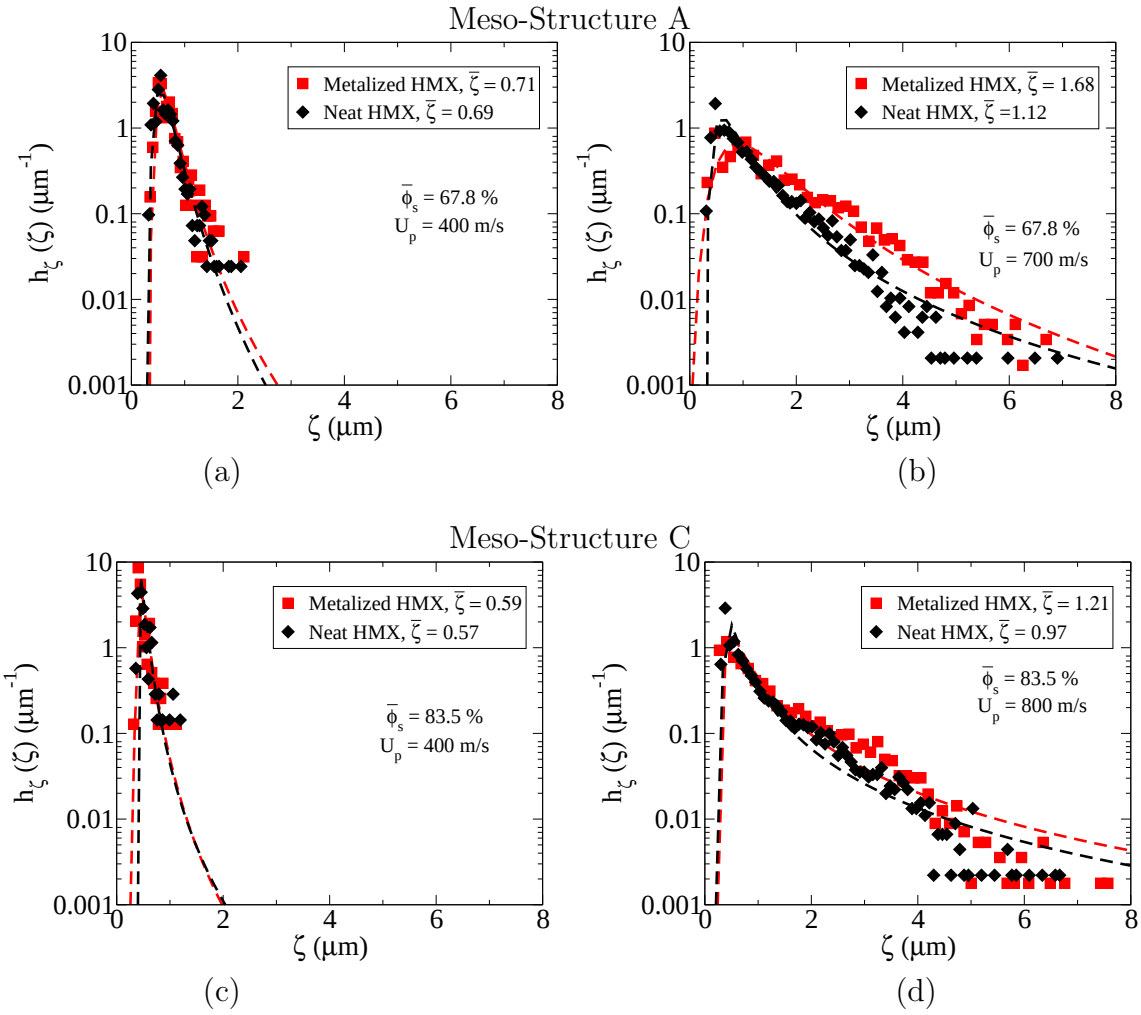

Figure 4.13: Predicted GEV PDFs for hot-spot area to perimeter ratios in explosive component for meso-structures A and C with $\lambda_m = 0.2$: (a) Meso-structure A ($U_p = 400$ m/s); (b) Meso-structure A ($U_p = 700$ m/s); (c) Meso-structure C ($U_p = 400$ m/s); (d) Meso-structure C ($U_p = 800$ m/s).

4.5.2 Volumetric Properties

Figures 4.14(a) and (b) show the hot-spot number density n_{HS} and volume fraction ϕ_{HS} based on the overall area A_T as a function of piston speed U_P for metalized meso-structures A-C. Also shown in the plots are the corresponding curves for neat HMX. Hot-spot number density curves for each of the meso-structures exhibit two distinct regions. One associated with a monotonic increase in n_{HS} due to hot-spot formation, and the other associated with a decrease in n_{HS} because of hot-spot agglomeration. Hot-spot agglomeration results from coalescence of smaller hot-spots to form large hot-spots due to the onset of significant plas-

ticity within the explosive at high impact speeds. Occurrence of hot-spot agglomeration is also possible at lower speeds, however the rate of hot-spot formation substantially exceeds the rate of hot-spot agglomeration. In Figure 4.14(a), n_{HS} is found to be sensitive to the effective packing density with an increase n_{HS} predicted for more porous meso-structures because of enhanced dissipation associated with pore collapse. The n_{HS} curves for metalized meso-structures suggests the inclusion of Al decreases the overall hot-spot number density due to dilution effect though the overall dissipation within the explosive increases due to enhanced pressures within the meso-structure. Dilution refers to a decrease in the overall number of explosive particles within the domain resulting in a fewer number of explosive-explosive contacts. In Figure 4.14(b) ϕ_{HS} increases monotonically across the entire range of piston speeds for all the meso-structures. Similar to predictions in Figure 4.14(a) an increase in porosity is found to increase the hot-spot volume fraction. A decrease in the hot-spot number density due to dilution can result in greater separation between reactive hot-spots and may suppress the process of hot-spot growth and coalescence. It is reasonable to expect that an increase n_{HS} results in hot-spots that are close to each other. During reaction, these hot-spots can thermally interact and quickly grow into larger more intense hot-spots eventually leading to a measurable global ignition event.

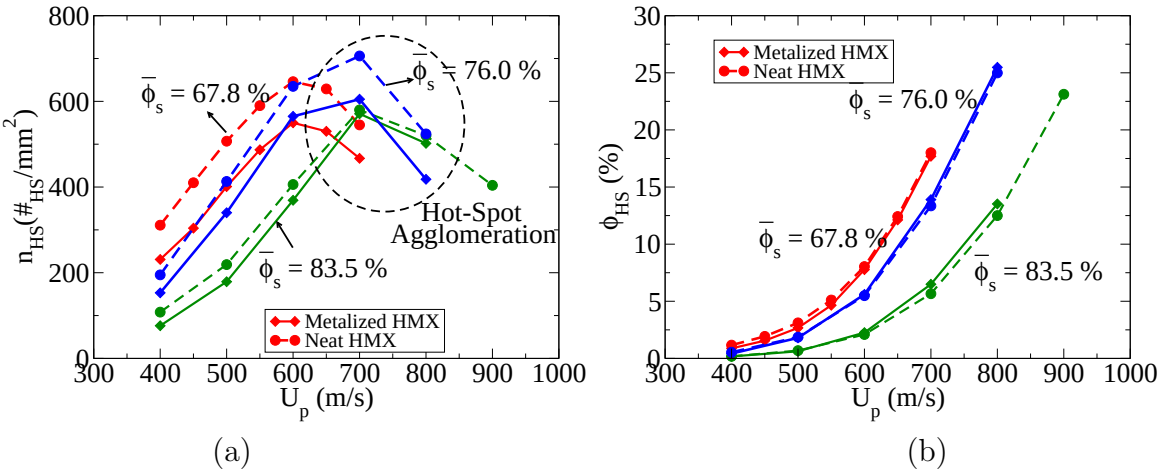

Figure 4.14: Overall hot-spot volumetric properties based on overall domain area A_T expressed as a function of piston speed for meso-structures A-C: (a)Number density n_{HS}; (b)Volume fraction ϕ_{HS}.

Figures 4.15(a) and (b) illustrate $\tilde{n}_{HS}$ and $\tilde{\phi}_{HS}$ based on explosive area as a function of U_p for meso-structures A-C. Predictions in Figure 4.15(a) are qualitatively different compared to the corresponding n_{HS} curves in Figure 4.14(a). For $U_p < 600$ m/s, a marginal decrease in $\tilde{n}_{HS}$ is predicted for metalized explosives compared to the corresponding neat explosives, whereas a marginal increase is observed for $U_p \geq 600$ m/s. At impact speeds below 600 m/s, hot-spot formation is mostly confined to particle interfaces since frictional dissipation and/or localized plasticity arising from frictionally induced surface tractions are the primary dissipative mechanisms. Hence, at lower impact speeds, HMX-Al contacts lead

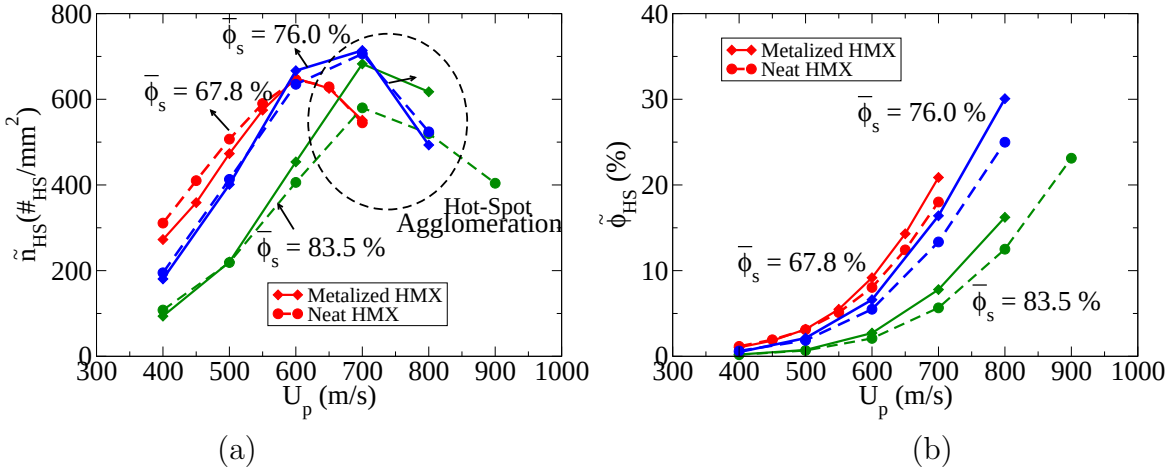

Figure 4.15: Overall hot-spot volumetric properties based explosive component area A_e expressed as a function of piston speed for meso-structures A-C: (a)Number density $\tilde{n}_{HS}$; (b)Volume fraction $\tilde{\phi}_{HS}$.

to a suppression in $\tilde{n}_{HS}$ since most of the dissipated energy at these interface is absorbed by the metal due to its high thermal conductivity. At higher speeds $U_p \geq 600$ m/s enhanced plasticity within explosive particles due to larger pressures results in an increase of $\tilde{n}_{HS}$. In Figure 4.15(b), the hot-spot volume fraction $\tilde{\phi}_{HS}$ is found to increase with the inclusion of metal due to an increase in average hot-spot size. Since the volumetric properties computed based on the overall and explosive area can be obtained based on simple scaling factors as seen in Eqn. 4.13, the following plots only provide predictions for these properties based on the explosive area.

Based on Eq. 4.12 the average hot-spot size is given by $\bar{A}_{HS} = \phi_{HS}/n_{HS}$. Figures 4.16(a) and (b) illustrate the variations in $\bar{A}_{HS}$ as a function of piston speed U_p and effective pressure $\bar{P}$ respectively. From Figure 4.16(a) it is observed that an increase in porosity leads to an increase in average hot-spot size due to enhanced dissipation resulting from plastic pore collapse. Additionally, for a fixed porosity, and piston speed, the inclusion of metal is found to increase the average hot-spot size within the material due to enhanced pressures as mentioned before. However, in Figure 4.16(b), values of A_{HS} show that for a given wave pressure, the inclusion of metal decreases the average hot-spot size marginally within the meso-structure.

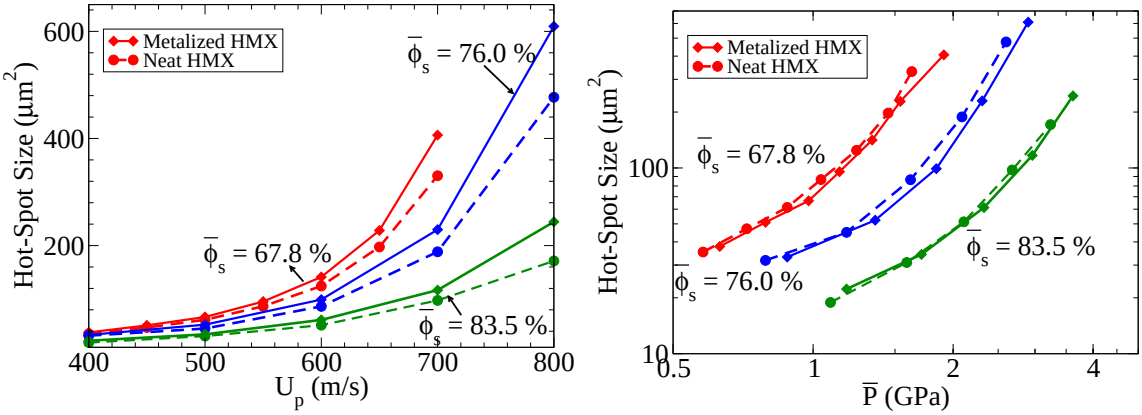

Figure 4.16: Variations in the average hot-spot size $\bar{A}_{HS}$ for meso-structures A-C as a function of piston speed and pressure: (a)$\bar{A}_{HS} = f(U_p)$; (b)$\bar{A}_{HS}$=$f(\bar{P})$.

Figures 4.17(a) and (b) illustrate the overall hot-spot number density and volume fraction for meso-structures A-C as a function of the power input $\bar{P}U_p$ on a log-log scale. From Figure 4.17(a) it is observed that $\tilde{n}_{HS}$ varies linearly with power input across all the meso-strucutres during hot-spot formation phase ($\bar{P}U_p \leq 1500\ GW/m^2$), and deviates from the linear trend due to hot-spot agglomeration. The predicted variations in $\tilde{n}_{HS}$ for each meso-structure suggests that during hot-spot formation-dominated phase, metal inclusion reduces hot-spot formation within the material for a fixed power input. Also, larger variations in $\tilde{n}_{HS}$ values of metalized and neat HMX formulations occur at lower power inputs. As

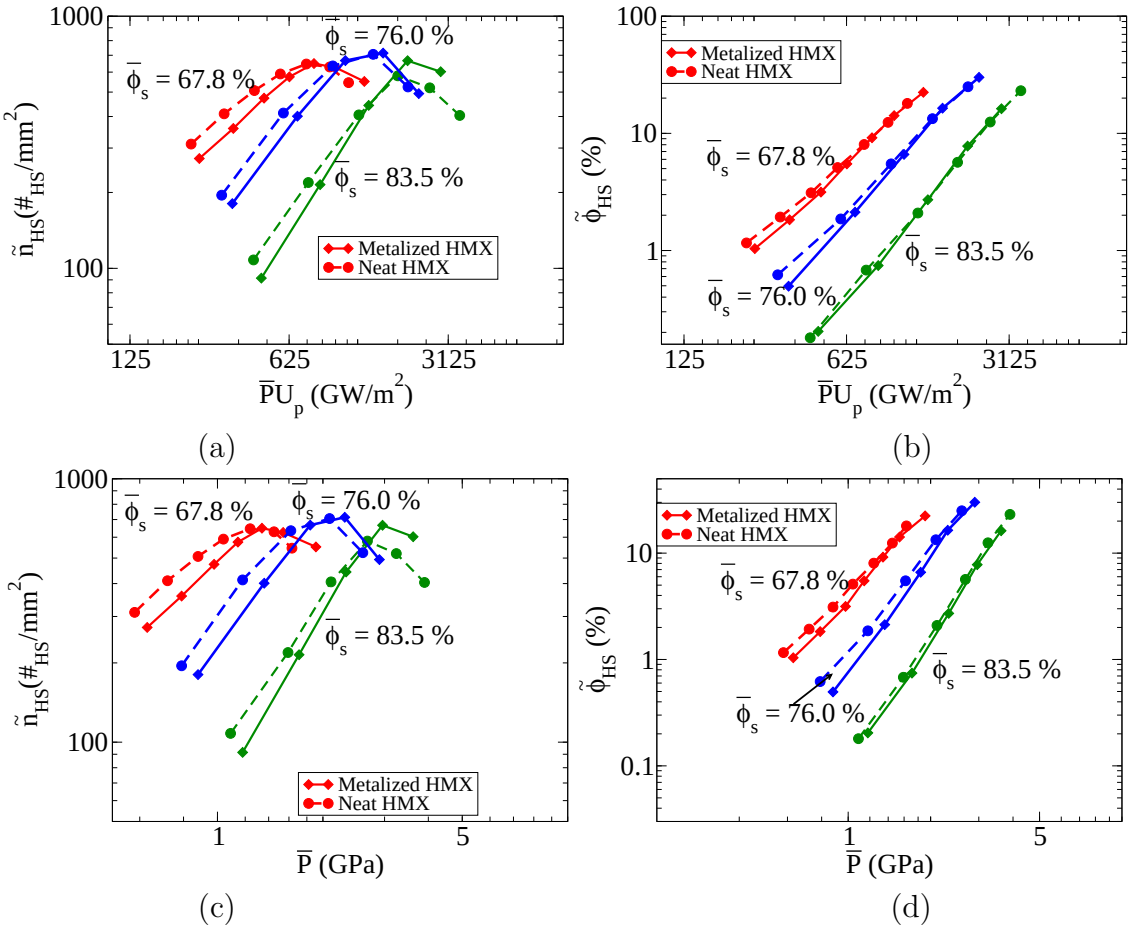

Figure 4.17: Overall hot-spot volumetric properties expressed as a function of the power input $\bar{P}U_p$ and effective pressure $\bar{P}$ for meso-structures A-C: (a)Number density $\tilde{n}_{HS} = f(\bar{P}U_p)$; (b)Volume fraction $\tilde{\phi}_{HS} = f(\bar{P}U_p)$; (c)Number density $\tilde{n}_{HS} = f(\bar{P})$; (d)Volume fraction $\tilde{\phi}_{HS} = f(\bar{P})$.

mentioned earlier, for low power inputs, a large fraction of the hot-spots are formed due to surface dissipative mechanisms (friction and/or frictionally induced plasticity), and HMX-Al interfaces contribute to a reduction in the formation of these localized hot-spots since the metal behaves as an energy sink. Similar observations can also be made for $\tilde{\phi}_{HS}$ curves in Figure 4.17(b) wherein most of the observed variations between the metalized and the neat HMX formulations occur at lower power inputs, however at higher power inputs these curves tend to collapse into a single curve. Once again, for a fixed power input, larger dissipation occurs within more porous material resulting in larger values of $\tilde{\phi}_{HS}$. Similar qualitative and

quantitative trends are also observed when the hot-spot volumetric properties are expressed as a function of the effective pressure within the material (Figures 4.17(c) and (d)).

From Figure 4.5 it is clear that compared to the neat HMX meso-structure, the effective plastic work in the explosive is marginally higher in the corresponding metalized explosive formulations for the entire range of piston speeds and/or wave pressures considered in this study. On the contrary, for impact speed impacts of $U_p < 600$ m/s, a marginal decrease in hot-spot number density, and volume fraction were observed in the metalized explosive formulations whereas above this impact speed an increase in these quantities is observed. This is counter intuitive because, an increase in plastic work leads to higher dissipation within the material, and as such it is reasonable to assume that the inclusion of metal leads to higher hot-spot number density and/or volume fraction for the entire range of U_p and/or $\bar{P}$. Figures 4.18, shows the hot-spot contours for meso-structure A and C corresponding to $U_p = 500$ m/s. Here, particles with black edges correspond to HMX, whereas particles with blue edges represent the metal particles. The red regions within the particles are the hot-spots, and the circled regions with numbers highlight identical regions in the metalized and the corresponding neat HMX meso-structures. By comparing the identical regions in the metalized and the corresponding neat HMX formulations, it is clear that there is an absence of hot-spot formation in the Al-HMX interfaces. As mentioned earlier, close to 95 % of the frictional dissipation at the Al-HMX interface is absorbed by the metal (Eq. 2.47) due to its high thermal conductivity. Because, for $U_p < 600$ m/s, a significant number of hot-spots are created due to frictional dissipation within the material, the inclusion of metal leads to a decrease in the hot-spot number density and volume fraction. However, at high impact speeds, due to enhanced pressures, the hot-spot number density and volume fraction increase within the metalized formulations due to increased plasticity. It is important to note that this qualitative behavior in the hot-spot volumetric curves is a consequence of the threshold temperature used to identify hot-spots ($T_{TH} = 500$ K). A decrease in the threshold temperature may lead to an increase in the hot-spot number density and volume fraction

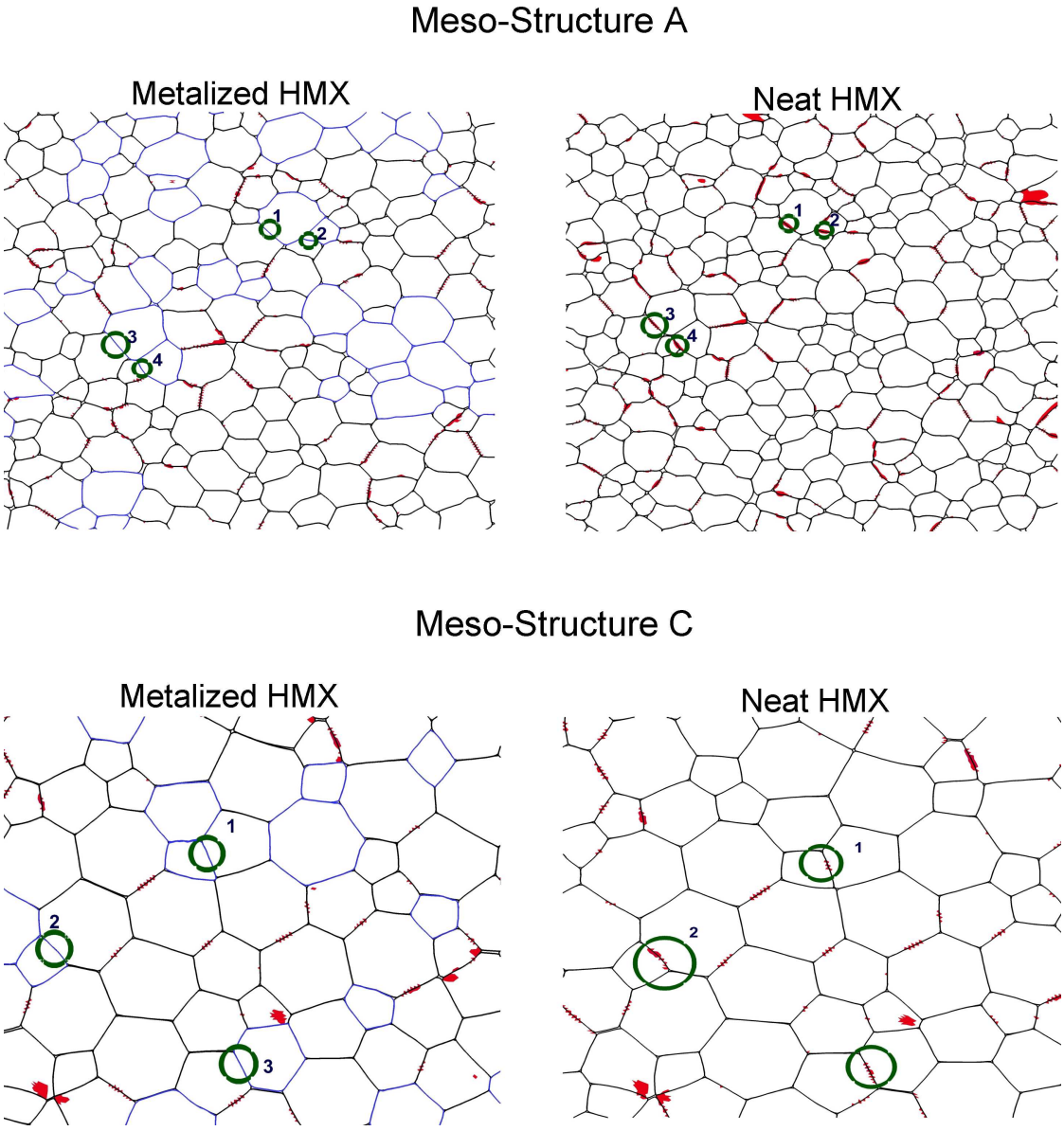

Figure 4.18: Hot-spot contours illustrating the suppression of frictionally induced hot-spots at the Al-HMX interfaces in meso-structures A and C for $U_p = 500$ m/s. Here, the particles with blue boundaries correspond to Al particles and particles with black boundaries corresponding to HMX particles.

in metalized explosive meso-structures for the entire range of piston speeds and/or wave pressures. However, marginal changes in the threshold value ($T_{th} \pm 10$ K) had little effect on the qualitative trends of these curves

The linear portion (hot-spot formation) of the volumetric curves in Figure 4.17 can be described using power a law. As mentioned earlier, pressure is an important parameter since

larger pressures within the material typically translate to faster burn rates which result in lower detonation time scales for the explosive. Mathematically, if V_{HS} represents a generic hot-spot volumetric property then it is related to the effective pressure $\bar{P}$ as

$$V_{HS} = c(\bar{P})^m, \tag{4.14}$$

where c is the prefactor, and m is the exponent. Equation 4.14 can also be written as

$$\log(V_{HS}) = \log(c(\bar{P})^m), \tag{4.15}$$

$$\log(V_{HS}) = m\log(\bar{P}) + \log(c). \tag{4.16}$$

Therefore, on a log-log plot the slope of the line is equal to m, and the intercept of the line is equal to $log(c)$. As mentioned, the ignition and growth models try to incorporate hot-spot volumetric properties and the corresponding pressures within the explosives to estimate effective burn rates. By deriving functional relationships between the hot-spot volumetric properties and pressure from the meso-scale simulations, it is possible to simplify the ignition models by eliminating a number of variables. Table A.4 in Appendix A lists the best fit values of the exponent and prefactor for meso-structures A-C. An increase in packing density $\bar{\phi}_s$ is found to increase the value of the exponent which means that for densely packed materials, marginal increase in pressure results in increased hot-spot formation. Because the particles are more geometrically constrained in densely packed systems, it is plausible that a marginal increase in wave pressure results in enhanced compaction of the particles. The compaction of the granular bed increases the average contact area between particles leading to an increase in hot-spot formation. Similar observations can also be made for ϕ_{HS} variation. For the range of piston speeds considered in this study, the pre-factor c indicates that though the rate of hot-spot formation/dissipation increases with pressure for densely packed materials, the overall dissipation is higher in more porous materials due to plastic pore collapse. The inclusion of metal $\lambda_m = 0.2$ is found to affect the exponents only marginally.

4.5.3 Hot-spot Proximity

Figures 4.19(a) and (b) illustrate the CDFs for the overall hot-spot $r_{s,s}$ distributions in meso-structures A-C corresponding to $U_p = 400$ and 700 m/s. Also shown in the plots are the corresponding distributions for neat HMX. Predicted distributions indicate a strong dependence of $r_{s,s}$ on both $\bar{\phi}_s$ and U_p. For $U_p = 400$ m/s, large variations in the nearest neighbor distances are observed between meso-structures, with closer hot-spot distances in more porous material because of the larger number of hot-spots within the material. Additionally for each meso-structure, dilution due to metal particles increases the average separation between hot-spots. In Figure 4.19(a), the average separation between the neighboring hot-spots is lower than the average particle size ($d = 60\ \mu m$) wherein the separation across meso-structures ranges from 16.87 μm in meso-structure A to 37.55 μm in meso-structure C. Hot-spot proximity measures are important in establishing the growth rates for reaction from ignition sites (critical hot-spots). At higher impact speeds $U_p = 700$ m/s, smaller scatter is observed in $r_{s,s}$ distributions across the meso-structures due to the formation of significant number of hot-spots within the material. The average separation between hot-spots is predicted to be in the range of 5.58 μm in meso-structure A to 9.05 μm in meso-structure C. Therefore, at strong shock pressures, hot-spot growth is likely to occur more rapidly. This observation is consistent with experiments which show lower run to detonation distances at higher shock pressures for a given material.

Figures 4.19(c) and (d) compare nearest neighbor CDFs ($r_{s,s}$, $r_{p,s}$) for metalized meso-structures A-C corresponding to $U_p = 400$ and 700 m/s. Greater separation between the CDFs for a given piston speed is indicates greater clustering. An increase in U_p is found to decrease the extent of clustering across all meso-structures as more hot-spots are formed within the material leading to a fairly homogeneous hot-spot fields. At $U_p = 400$ m/s, a subtle increase in clustering is predicted with an increase in $\bar{\phi}_s$. This increase in clustering for densely packed material is likely due to the formation of hot-spots within well defined stress chains of the meso-structure.

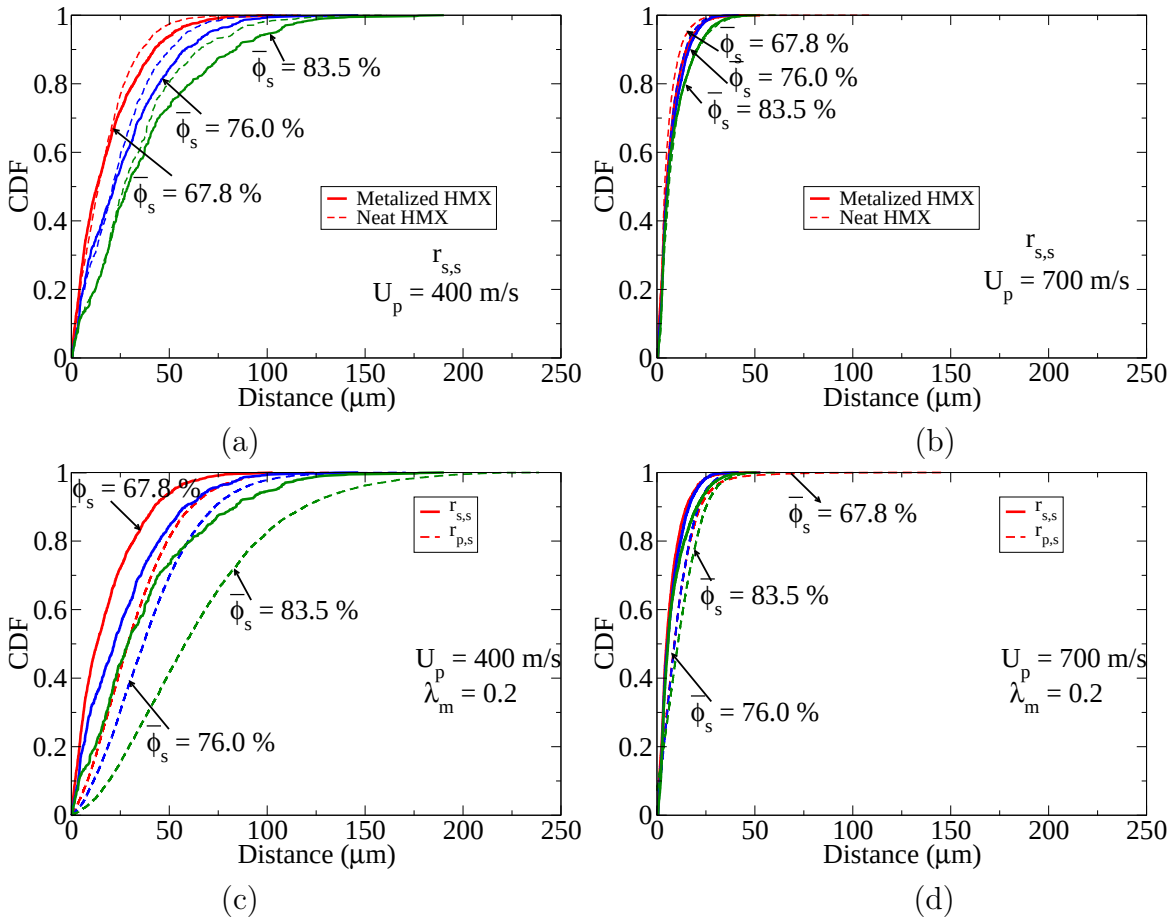

Figure 4.19: Overall hot-spot proximity CDFs ($r_{s,s}, r_{p,s}$) as a function of piston speed for meso-structures A-C: (a)$r_{s,s}$-U_p = 400 m/s; (b)$r_{s,s}$-U_p = 700 m/s; (c)($r_{s,s}, r_{p,s}$)-U_p = 400 m/s; (d) ($r_{s,s}, r_{p,s}$)-U_p = 700 m/s.

4.6 Critical Hot-Spots

Critical hot-spots refer to those hot-spots that have enough thermal inertia to overcome conductive losses. In this study, critical hot-spots are identified based on the joint distributions of hot-spot size, and the corresponding peak temperatures. The selection of peak temperature as a factor in determining the criticality of hot-spots is reasonable since the reaction is most likely to begin in the regions of high temperatures and grow outwards towards the cooler regions of the hot-spot. The combination of hot-spot size and peak intensity that qualifies a hot-spot as *critical* is based on a thermal explosion manifold similar to the one derived by Tarver et al. [75] for cylindrical hot-spots in neat HMX. The explosion manifold is represented by a solid curve as seen in Figure 4.20 where a hot-spot above the curve is

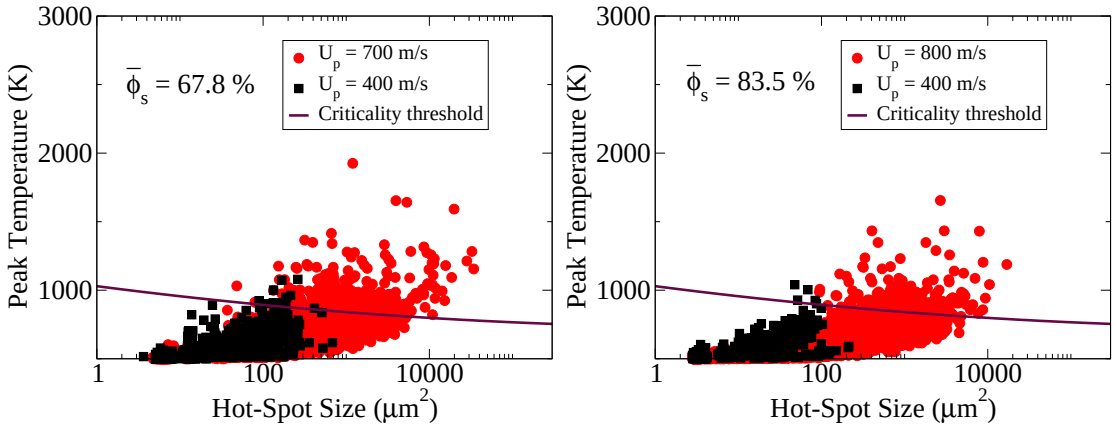

Figure 4.20: Joint distribution of hot-spot area and peak temperature. The solid curve represents a thermal explosion manifold used to identify critical hot-spots: (a) Meso-structure A ($\bar{\phi}_s = 67.8\%$); (b) Meso-structure C ($\bar{\phi}_s = 83.5\%$).

considered critical. We approximate the manifold by a curve fit to the data reported in [75]: $T_{crit} = c_2(lnA_{crit})^2 + c_1 lnA_{crit} + c_0$, where T_{crit} is the critical temperature and A_{crit} is the critical area. The constants of curve fit are given by $c_0 = 0.85 \times 10^3$, $c_1 = -33.84$, and $c_2 = 0.984$. In our analysis, Tarver's explosion manifold is relaxed by requiring lower peak temperatures ($\hat{T} = 85\ \%\ T_{crit}$) for a given hot-spot size to be considered critical. This relaxation in the explosion manifold results in larger number of critical hot-spots, and provides reasonable sample space to perform meaningful statistics on the critical hot-spot fields.

Figures 4.20(a) and (b) show the variations in hot-spot size and peak temperature for metalized meso-structures A and C with piston speed. Here, hot-spots above the threshold are termed critical and hot-spots below the threshold are sub-critical. In Figure 4.20, the following observations are noteworthy. First, a positive correlation exists between hot-spot size and peak temperature. Second, an increase in porosity and/or U_p results in larger number of critical hot-spots because of enhanced plasticity and frictional dissipation resulting from high pressure slip between particles.

Critical hot-spot number densities $\tilde{n}_{HS}$ and volume fractions $\tilde{n}_{HS}$ as a function of U_p are shown for various meso-structures in Figure 4.21. For a given meso-structure small variations in critical hot-spot number densities are predicted between the metalized and

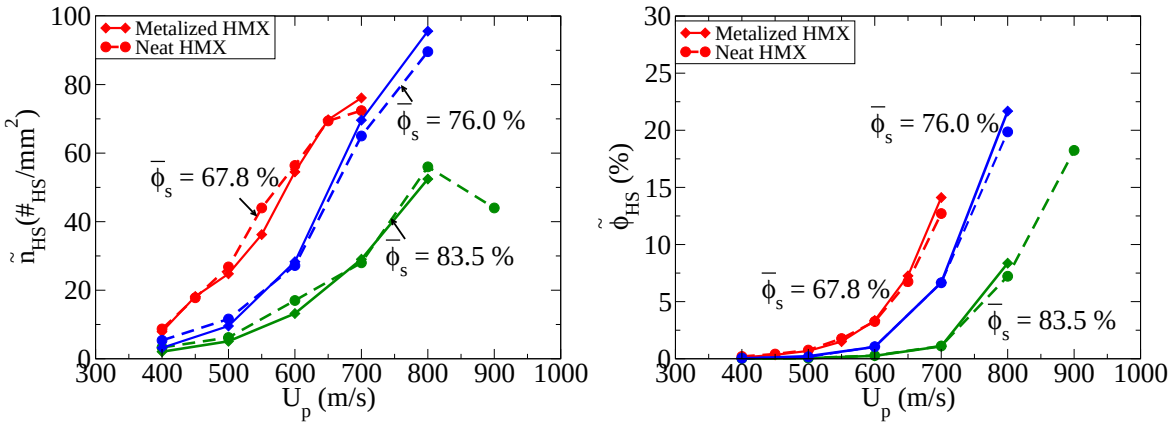

Figure 4.21: Critical hot-spot volumetric properties expressed as a function of piston speed for meso-structures A-C: (a)Number density $\tilde{n}_{HS}$; (b)Volume fraction $\tilde{\phi}_{HS}$.

neat HMX formulations. In Figure 4.21(b) an increase in U_p is found to marginal increase the hot-spot volume fraction for metalized formulations indicating larger critical hot-spots due to enhanced plasticity within the material.

For a fixed power $\bar{P}U_p$ or $\bar{P}$, the critical hot-spot number densities and volume fraction, are found to decrease with the inclusion of metal as shown in Figure 4.22. Also, $\tilde{n}_{HS}$ and $\tilde{\phi}_{HS}$ do not exhibit a linear linear relationship with the power input indicating that critical hot-spot formation maybe more stochastic compared to the overall hot-spot formation due to the non-linearities associated with the joint distributions of hot-spot size and the corresponding peak intensity. Because, for a fixed wave strength, both the critical and the overall hot-spot number densities were lower for metalized formulations which results in larger separation between hot-spots, it is plausible that the inclusion of metal reduces the sensitivity of the meso-structures considered in this chapter. Without implementing combustion within the model it is impossible to predict as to which material is more shock sensitive. It is possible that a meso-structure with just few critical hot-spots may detonate faster than a meso-structure with larger number of critical hot-spots. However, the probability of this occurring is lower. As such, based on the predictions of the inert hot-spot fields, one can only incur the most probable scenarios.

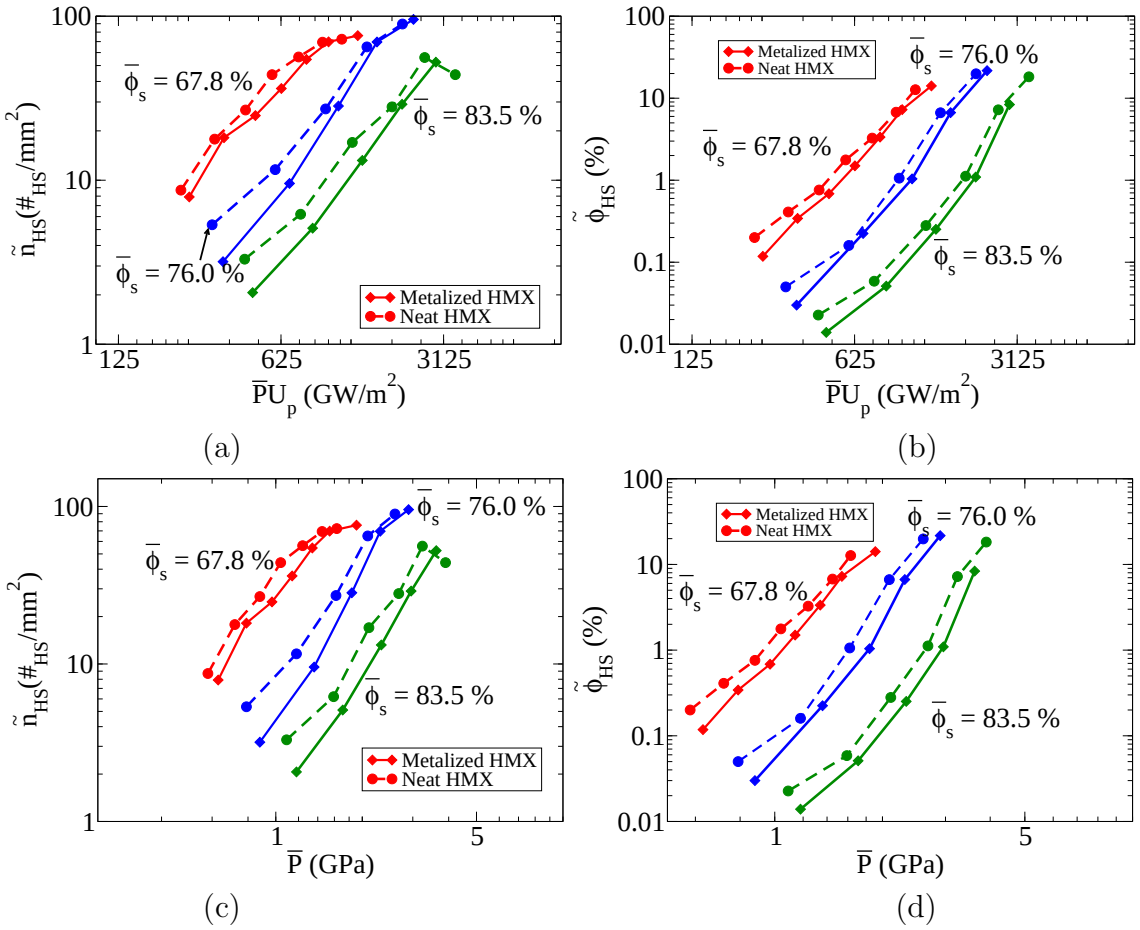

Figure 4.22: Critical hot-spot volumetric properties expressed as a function of power input $\bar{P}U_P$ and effective pressure $\bar{P}$ for meso-structures A-C: (a)Number density $\tilde{n}_{HS} = f(\bar{P}U_p)$; (b)Volume fraction $\tilde{\phi}_{HS} = f(\bar{P}U_p)$; (c)Number density $\tilde{n}_{HS} = f(\bar{P})$; (d)Volume fraction $\tilde{\phi}_{HS} = f(\bar{P})$.

Additionally, it is important to note that meso-structures considered in this chapter are composed of a narrow range of particle sizes ($\bar{r}$ = 20-40 μm). Also, the sizes of Al and HMX particles are identical across the meso-structures. However, experiments indicate variations in material sensitivity of aluminized HMX formulations due to changes in the aluminum particle size [32]. As such, it may be important to consider the effects of Al particle size on hot-spot fields as well. The following chapter addresses this issue.

Figures 4.23(a) and (b) show the CDFs for critical hot-spot $r_{s,s}$ distributions in meso-structures A-C corresponding to U_p = 400, and 700 m/s. An increase in porosity and/or piston speed reduces the average separation between the critical hot-spots. Additionally

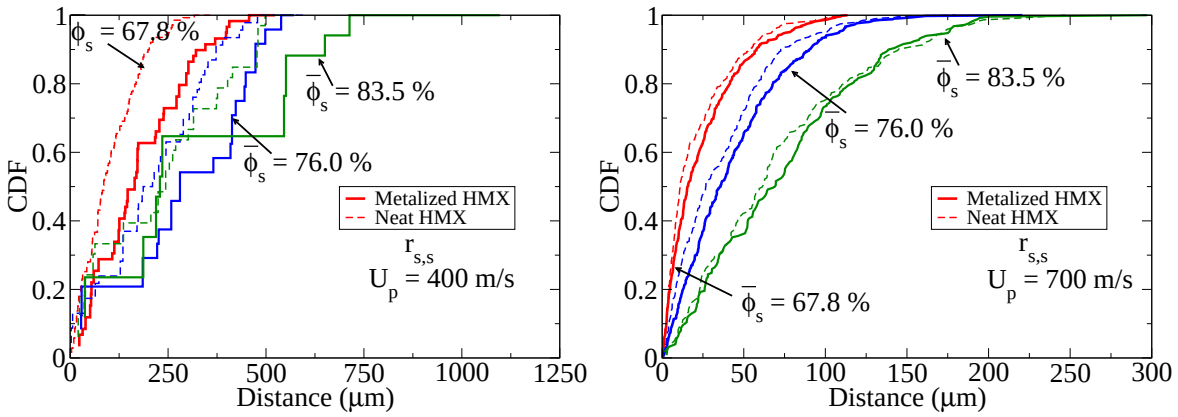

Figure 4.23: Critical hot-spot proximity CDFs for $r_{s,s}$ as a function of piston speed for meso-structures A-C: (a)$U_p = 400$ m/s; (b)$U_p = 700$ m/s.

inclusion of metal is found to substantially increase critical hot-spot separation at $U_p = 400$ m/s, with a minimum increase of around 80 μm predicted for meso-structure A. Densely packed meso-structures exhibit even larger differences in $r_{s,s}$ values between metalized and neat HMX formulations. The enhanced sensitivity to critical hot-spot formation at lower speeds is due to localized plasticity and/or frictional dissipation which are more sensitive to particle scale interactions at the HMX-Al interfaces. However at $U_p = 700$ m/s, smaller variations in the critical hot-spot distances are predicted between metalized and the corresponding neat HMX formulations due to the onset of significant plasticity within the material leading to substantially larger number of critical hot-spots in both metalized and neat explosives.

4.7 Combustion Implications

The Shock to Detonation (SDT) process can be described as a multi-step process. First, the passage of the deformation wave within the material results in the creation of critical hot-spots that may possess enough thermal inertia to overcome conductive and acoustic expansion losses and as such react behind the deformation wave. Second, the exothermic energy release from the critical hot-spot reaction (local ignition) may accelerate the hot-spot growth and coalescence which results in a measurable/observable global ignition event. Finally, the global ignition may transition to material detonation if the conditions are favorable. Not

all critical hot-spots are of equal importance. Some of the critical hot-spots may exhibit explosion times which are much lower than the corresponding wave rise times. Additionally, these critical hot-spots may quickly interact with the surrounding hot-spots leading to faster hot-spot growth and coalescence which influences the global ignition event. Ignition events which occur on the time-scales of the wave rise times can result in enhancing the strength of the deformation wave since the exothermic energy released from the ignition is coupled to the wave . As such, estimating the thermal explosion time distributions for the critical hot-spots is important. Here, the thermal explosion times are estimated based a temperature dependent expression t_{ex} for HMX based materials formulated by [37]: $\tau_{exp}(\hat{T}) = exp(ln(\frac{1}{B} + \frac{E_T}{R\hat{T}}))$, where $B = 5.9 \times 10^{12}\ s^{-1}$, $E_T = 148.9\ KJ/mol$, and $R = 8.314 \times 10^{-3}\ KJ/K\text{-}mol$ is the universal gas constants. Because, the explosion times are estimated based on the peak hot-spot temperatures, these values likely represent the lower limits of the explosion time. Whether the thermal explosion times are strictly based on the intensity of the hot-spot or rather on the joint distribution of hot-spot intensity and size is an unresolved issue. Figure 4.24 shows the predicted critical hot-spot thermal explosion times τ_{ex} for neat HMX meso-structures A and C for varying piston speeds. Also shown are the corresponding wave rise times. From Figure 4.24 it is evident that few of the critical hot-spots have τ_{ex} much lower than the wave rise times of $< 1\ \mu s$. However, most of the critical hot-spots have long explosion times compared to the simulation time and/or wave rise times (O$\approx$ 0.1-5 μs). Additionally, little variation in explosion times is predicted due to variations in the porosity, composition and/or wave strength. How many critical hot-spots are necessary for global ignition of the material remains an unsolved question within the energetics community. It is possible that a single critical hot-spot can eventually trigger a global ignition. The predicted explosion times indicate that the sensitivity of the materials may be more dependent on the growth and coalescence stage than the local ignition phase. It is important to note that there are uncertainties associated with these predictions due to modeling assumptions. For example, the predicted hot-spot temperatures are likely to be different from the hot-spot temperatures

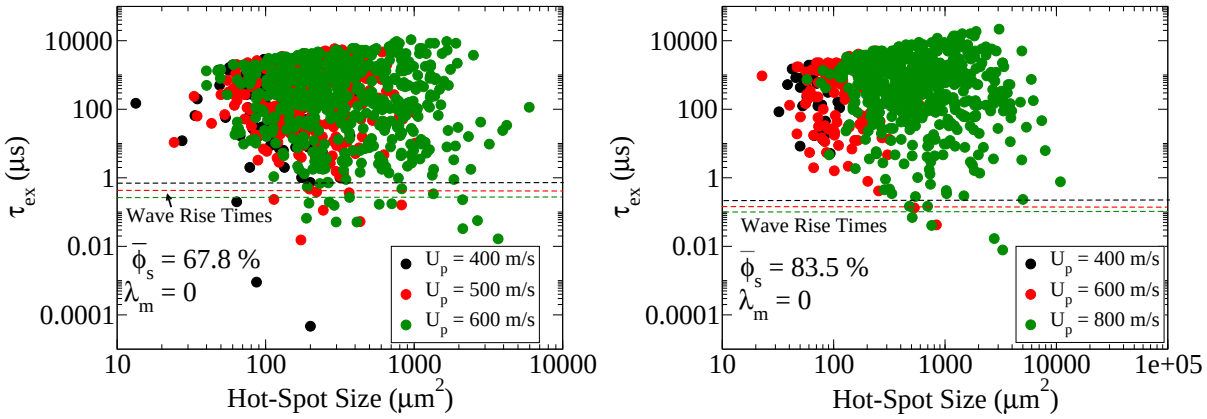

Figure 4.24: Predicted explosion times as a function of hot-spot size for neat HMX meso-structures A and C: (a)Meso-structure A; (b) Meso-structure B.

in reality due to temperature independent material properties (specific heat, yield strength and friction coefficient) used in this analysis. Also, other physical phenomena such as melting, and fracture may suppress or enhance the hot-spot temperatures, however they were not considered in the study.

While critical hot-spot fields are useful in estimating the local ignition within the material, the overall hot-spot volumetric quantities can potentially be used to establish sensitivity of the meso-structures by computing global ignition manifolds. It was observed in the previous sections that an increase in hot-spot number density and/or volume fraction typically leads to a decrease in the average hot-spot separation. Because, global ignition is controlled by hot-spot growth and coalescence which is dependent on the hot-spot separation in the material, the volumetric quantities can be used to provide preliminary predictions for the global ignition times within these materials. The detonation times, and run to detonation distances are routinely expressed as a function of wave pressure within the energetics community since the burn rate of the explosives are strongly dependent on the wave pressure. Hence, the main purpose of the analysis is to formulate a method wherein the ignition manifolds and/or global ignition times (τ^*) for all the meso-structures can explicitly be cast in terms of the equilibrium wave pressure $\bar{P}$. It is important to mention that the method outlined here is a simple description of an extremely complex combustion process, and there-

fore, the predictions shown in this section are only to highlight the qualitative trends in the ignition manifolds. To provide accurate predictions of ignition times/manifolds that can replicate experimentally observed values over a wide range of loading conditions, requires the use of complex ignition and growth models that account for detailed hot-spot statistics including distributions in hot-spot size, intensity, shape, and proximity. Further, realistic 3-D meso-structures and relevant physics such as fracture, melting, and temperature dependent material properties may have to be employed within the meso-scale model. However, this is beyond the scope of this study. In this analysis, it is assumed that the ignition time of the material varies inversely with the hot-spot mass flux emanating behind the quasi-steady deformation wave. This is a reasonable assumption because, if higher amounts of mass within the explosive is heated to elevated temperatures behind the deformation wave, the material is likely to exhibit faster global ignition times. It is important to note that in reality, the ignition time could be nonlinearly related to the inverse of the mass flux. However for simplicity, the non-linear variations in ignition time with inverse of the mass flux are not considered in this study for simplicity. Figure 4.25 represents the formation of hot-spots behind the deformation wave. Here, D corresponds to the wave speed, δ is the compaction wave thickness, H is the transverse width of the deformation wave, and W corresponds to the width of the quasi-steady region behind the wave. In a wave attached frame, the rate of hot-spot mass created behind the deformation wave can be defined as

$$\frac{dm_{HS}}{dt} = \rho_{HS}\phi_{HS}\frac{dV_T}{dt}, \tag{4.17}$$

where m_{HS} is the hot-spot mass, ρ_{HS} is the average hot-spot density, ϕ_{HS} is the hot-spot volume fraction, and dV_T/dt is the time rate of change of total volume fraction behind the deformation wave which can be expressed as

$$\frac{dV_T}{dt} = (D - U_p)A. \tag{4.18}$$

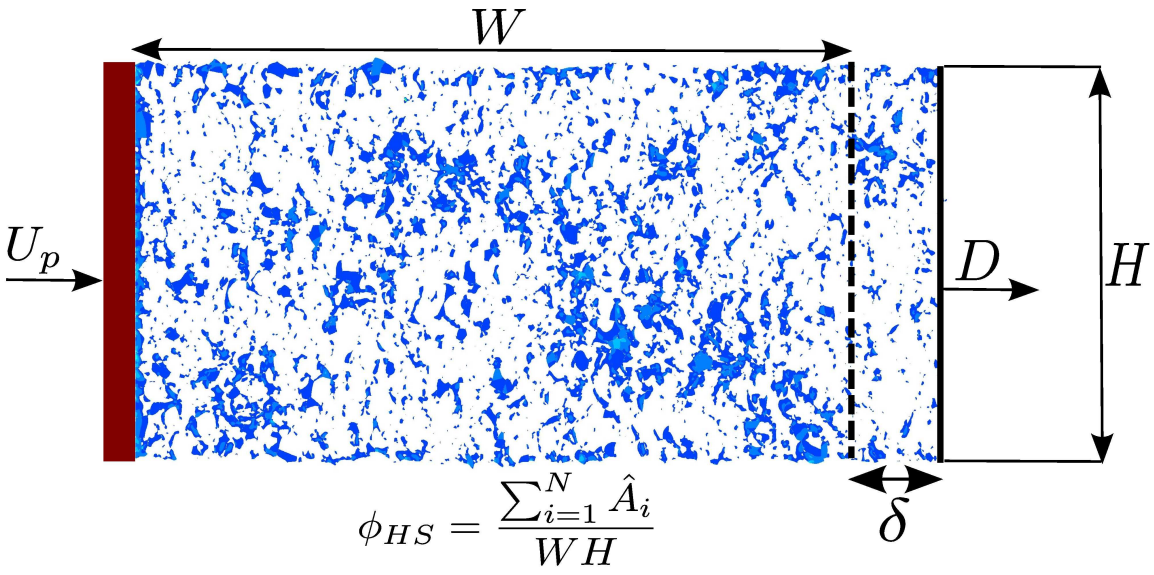

Figure 4.25: Schematic representing the creation of hot-spot fields within the meso-structures due to piston driven quasi-steady waves.

Here, A is the transverse area of the wave which is mathematically defined as $A = H \times 1$. Using Eq. 4.18, Eq. 4.17 can be rewritten as

$$\frac{dm_{HS}}{dt} = \rho_{HS}\phi_{HS}(D - U_p)A. \tag{4.19}$$

Since we are primarily focused on explosive component heating, we can express ϕ_{HS} as $\phi_{HS} = \tilde{\phi}_{HS}\phi_e$. Using this expression and simplifying, the rate of explosive hot-spot mass flux behind the deformation wave can be written as

$$\frac{1}{\phi_e A}\frac{dm_{HS}}{dt} = \rho_{HS}\tilde{\phi}_{HS}(D - U_p). \tag{4.20}$$

It is important to note that ρ_{HS} varies behind the deformation wave for different meso-structures for a given wave-strength. However, for simplicity an equilibrium value of hot-spot density $\rho_{HS} = 1903\ Kg/m^3$ is assumed throughout this analysis. The ignition time is assumed to be inversely proportional to the mass flux rate described by Eq. 4.20, and

mathematically it is expressed as

$$\rho_{HS}\tilde{\phi}_{HS}(D - U_p)\tau^* = I^*, \tag{4.21}$$

where τ^* is the ignition time, and I^* is a critical mass flux value for ignition which may vary for different meso-structures and wave-strengths. However, in this analysis, the value of I^* is chosen based on experimentally available ignition time for neat granular HMX ($\bar{\phi}_s = 65.5\%$) performed by McAfee et al. [53]. McAfee reported that vigorous combustion in neat HMX ($\bar{\phi}_s = 65.5\%$) begins at approximately 400 μs for a wave pressure of $\bar{P} \approx 0.04$ GPa. Since meso-structure A has an initial packing density ($\bar{\phi}_s = 67.8\%$) which is close to the packing density considered in McAfee's study, it is plausible to reasonably estimate the value of I^* corresponding to $\tau^* = 400$ μs, and $\bar{P} = 0.04$ GPa for meso-structure A. Both the wavespeed D and the corresponding piston speed U_p can be expressed as a function of $\bar{P}$, based on the curve fits for the Hugoniot plots. The best fit parameters for these curve fits are shown in Appendix A. By using these values in Eq. 4.21, the value of the critical mass flux is estimated to be $I^* = 0.0057\ Kg/m^2$. Though the packing densities of most meso-structures and the corresponding wave strengths/piston speeds considered in this study are significantly different from the one used in McAfee's study, for simplicity, $I^* = 0.0057\ Kg/m^2$ is used for all the meso-structures. As mentioned earlier, I^* may have a non-linear dependency on both the meso-structure and wave strength, however more experimental data on porous HMX is be needed to better estimate these variations in I^*. Since $\tilde{\phi}_{HS}$, D, and U_p can all be expressed as a function of $\bar{P}$, ignition time τ^* can be described solely as a function of wave pressure $\tau^* = f(\bar{P})$. Some preliminary predictions using the method outlined are presented below.

Figure 4.26(a) shows the variations in τ^* for meso-structures A-C as a function of wave pressure $\bar{P}$. Also shown are the experimentally observed [25] detonation times for porous HMX with an initial packing density of $\bar{\phi}_s = 65.5\%$. For the global ignition times to be

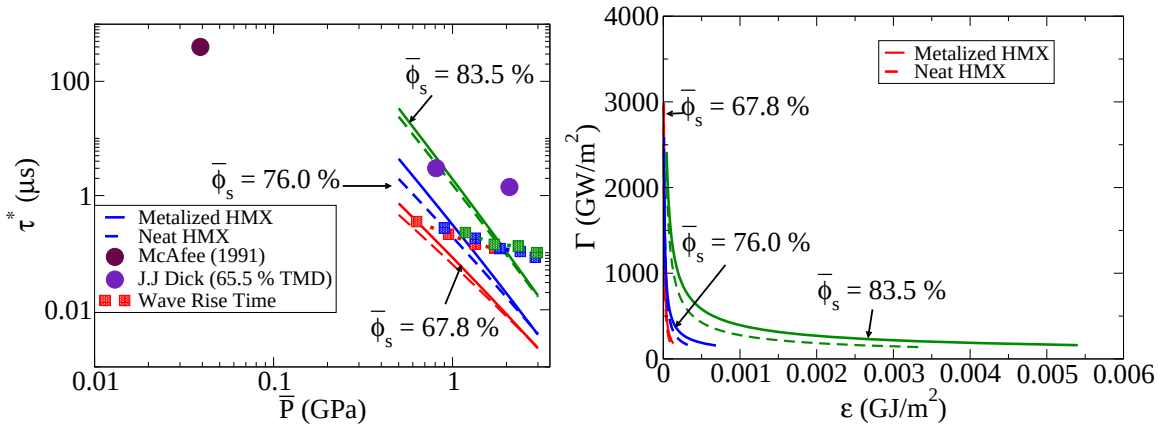

(a) (b)

Figure 4.26: Predicted ignition manifolds for meso-structures A-C: (a)$\tau^*/\tau^*_B = f(\bar{P})$; (b) Power ($\Gamma$)-Effluence ($\Gamma\tau*$).

meaningful, they must have a value lower than the corresponding detonation times. From Figure 4.26(a) the following observations are noteworthy. First, it is evident that the predicted ignition times are lower than their corresponding wave rise times. This means that for the piston speeds in the range of $400 \leq U_p \leq 800$ m/s considered in this study, the energy released by material ignition is strongly coupled to the lead deformation wave. Second, an increase in porosity leads to lower global ignition times within the material due to enhanced dissipation. This is consistent with the predicted hot-spot fields wherein larger values of hot-spot volume fractions were predicted for a given wave pressure in meso-structure A ($\bar{\phi}_s = 67.8\%$) compared to meso-structures B ($\bar{\phi}_s = 76.0\%$) and C ($\bar{\phi}_s = 83.5\%$) which have lower initial porosities. Second, for a fixed porosity, the inclusion of metal leads to an increase in ignition times within the meso-structures with larger variations in τ^* predicted at lower pressures. Once again this observation is consistent with the predicted $\tilde{\phi}_{HS}$ curves which exhibit lower values in metalized meso-structures corresponding to a given wave pressure. Figure 4.26(b) show the power $\Gamma = \bar{P}U_p$ -effluence $\epsilon = \bar{P}U_p\tau^*$ curves. For a given meso-structure the power-effluence curves provide the ignition manifolds wherein the region above the curve results in material ignition. From Figure 4.26(b) it is observed that an increase in Γ leads to a decrease in ϵ due to lower ignition times. Once again, the curves show similar qualitative trends between the meso-structures with an increase in porosity resulting

in lower ignition times for a given power input, and the inclusion of metal requiring higher power inputs to ignite the material for a fixed packing density/porosity.

CHAPTER 5
EFFECTS OF METAL PARTICLE SIZE

In this chapter, the effects of component particle size ratios and their corresponding distributions on the shock sensitivity are discussed. Here, component particle size ratio (CR) represents the ratio of the effective metal (Al) particle size to the effective explosive (HMX) particle size. The CR values are varied by varying the effective size of the metal particles while maintaining the same effective size of the HMX particles within the meso-structure. As discussed later in this section, only a narrow range of component size ratios are considered in this study due to limitations of the numerical technique. A number of experiments have tried to characterize the effects of particle size on shock sensitivity of explosive mixtures. Experiments performed by [80] on aluminized HMX composites suggested that values of $CR > 1$ resulted in better decomposition of HMX particles within the detonation wave front due to enhanced reactions, resulting in large detonation pressures. The authors argued that the enhanced reaction was not observed when large HMX particles were surrounded by nano-aluminum particles because the nano-aluminum particles were more effective in absorbing dissipated energy within the detonation wave due to their large surface area (thermal conduction). On the contrary, numerous experiments [32, 77] have suggested that nano-aluminum particles may enhance the post-detonation blast wave because of their larger burn surface area if the shock intensity is strong enough to start ignition within the explosive grains. Experiments performed by [72, 76] showed that distance to detonation vs. pressure curves for coarse and fine particles will cross. At low pressures, fine particles were less sensitive to impact while the ordering was reversed for high pressures. The argument postulated was that at lower inputs, the fine particles have lower stresses due to increased surface area, leading to lower temperatures, whereas at high inputs, the smaller particles burn more rapidly due to their large surface area. Along with the effective particle size, the

particle size distributions (monomodal, bimodal) can also influence the shock sensitivity of the explosives. Computational studies performed by Barua et al.[6], suggested an increase in PBX sensitivity with bimodal distribution of particle sizes. Barua argued that bimodal distribution of particle sizes resulted in micro-structures which had a larger effective packing density and as such, resulted in enhancing dissipation within the material due to fracture at the contact interfaces. On the contrary experiments performed by [68] showed larger run distance to detonation for PBX explosives with bimodal distributions of particle sizes. However little physical justification was provided for this observation. How the variations in component particle sizes and the corresponding distributions affects the shock sensitivity of the material, is a wide open question within the energetics community.

Performing a detailed analysis on the effects of particle sizes, and particle size distributions is impossible due to the vast number of variables involved. As mentioned, one of the limitations of the combined FEM-DEM technique used in this study is that it is susceptible to mesh distortion issues resulting from large plastic deformation of particles. Due to this limitation, only a few combinations of particle size ratios could be addressed in this study. Metal (Al) particles have a lower yield strength compared to explosive (HMX) particles, and therefore are likely to undergo larger inelastic deformation for a given wave strength. As such, meso-structures with $CR < 1$ have a higher probability of producing numerical instabilities. Even meso-structures with moderate size ratios of $CR = 1/3$ could not be simulated using this technique because of mesh-distortion associated with large deformation of small Al particles that were enveloped by large HMX particles. The deformation of these small particles occurs as a result of pinching wherein a small particle is squeezed between two large particles which essentially act as rigid walls. Pinching of the small particles can lead to significant heating and thereby enhance explosive sensitivity. Due to the numerical limitations mentioned above, in this study, only meso-structures with $CR > 1$ were considered. Even for these meso-structures, simulations could be performed up to $CR = 6$, as larger ratios resulted in numerical instabilities due to severe distortion of small explosive

particles that were enveloped by large Al particles. A bimodal distributions of particle sizes will be considered to investigate whether particle size distribution considerably affects the shock sensitivity. With respect to the metalized explosive formulations, each mode corresponds to a Gaussian distribution of a single component (HMX or Al). A meso-structure with a uniform particle size distribution of equally sized Al, and HMX particles ($CR = 1$) forms the baseline case. The corresponding neat HMX formulations of these meso-structures enable us to compare the effects of metal particle size and metal mass fraction on explosive component heating. The details of the meso-structures for which predictions are given in this chapter are summarized in Table 5.1. Along with the above mentioned variations, for a fixed value of CR and particle size distribution, the metal mass fraction is varied in the range of $0.0 \leq \lambda_m \leq 0.56$.

As seen in Table 5.1, the effective porosity across these meso-structures are not the same. However, the variations are minimal and most of the observed variations in the predictions are likely due to differences in particle size ratios and distributions. The marginal variations in the effective porosity is a consequence of the pseudo-gravity settling algorithm used to generate the material packing. Figure 5.1 illustrates the different meso-structures considered to address the particle size effects. Also shown are the corresponding particle size distributions within each meso-structure. The red particles in the ensemble represent Al while the yellow particles represent HMX. For the neat HMX formulations of these meso-structures even the large metal particles are considered as HMX particles. In the remainder of this chapter, the meso-structures are referred using the nomenclature given in Table 5.1 (*EM 1-EM 6*)

5.1 Hugoniots

Hugoniots represent the effective end states behind the deformation waves. For meso-structures with equal particle sizes of Al and HMX, initial packing density ($\bar{\phi}_s$) and metal fraction λ_m were found to affect the Hugoniot curves (Chapter 4). Particle size can also have an effect on the bulk wave end states as suggested by some experiments [72] since smaller

Table 5.1: Summary of meso-structures considered in the study to investigate the effects of particle sizes and particle distributions

Meso-structure	ϕ_s	Distribution	Mean Particle Radius (μm)	λ_m
EM 1	83.7 %	Bimodal	Al $\approx$ 101, HMX $\approx$ 32	0.0, 0.2
EM 2	83.0 %	Bimodal	Al $\approx$ 180, HMX $\approx$ 32	0.0, 0.2
EM 3	83.5 %	Uniform	Al $\approx$ 30, HMX $\approx$ 30	0.0, 0.2
EM 4	84.6 %	Bimodal	Al $\approx$ 101, HMX $\approx$ 32	0.0, 0.56
EM 5	85.9 %	Bimodal	Al $\approx$ 180, HMX $\approx$ 30	0.0, 0.56
EM 6	83.5 %	Uniform	Al $\approx$ 30, HMX $\approx$ 30	0.0, 0.56

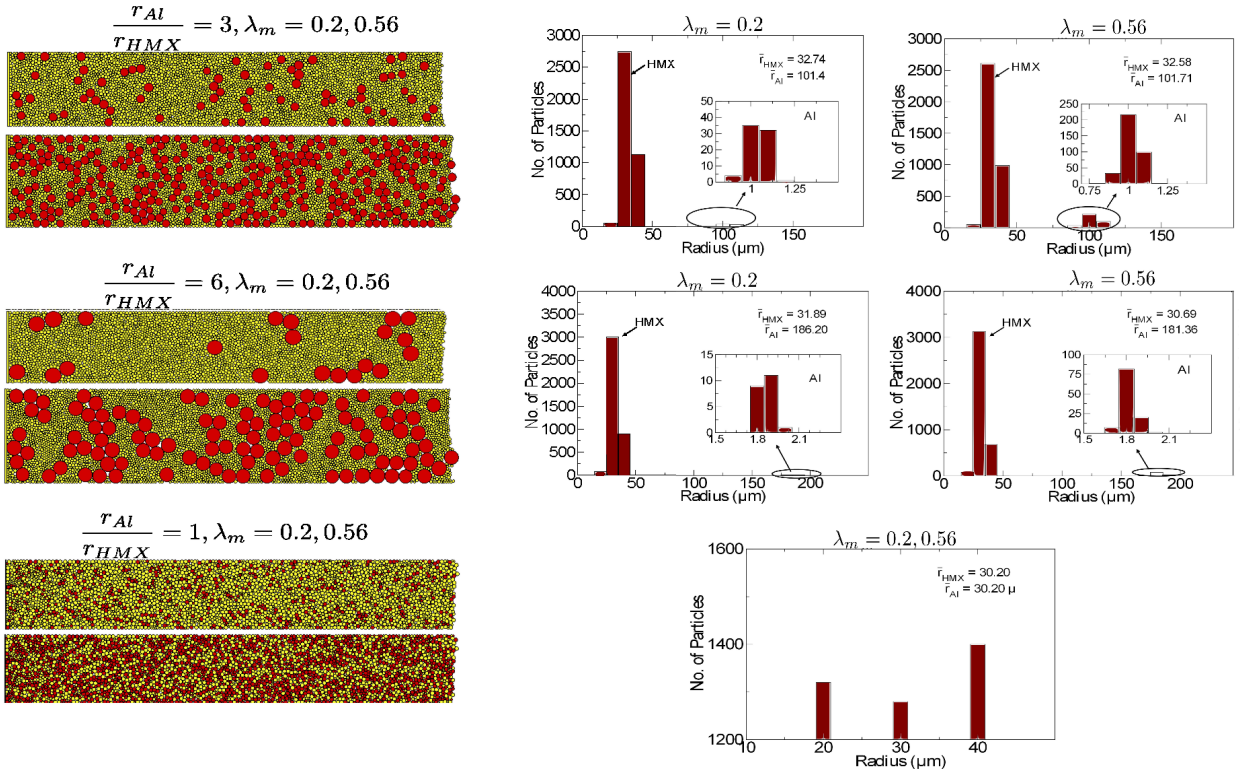

Figure 5.1: Meso-structures with varying particle sizes, particle distributions and composition. Here, red particles represent metal, and yellow particles represent explosive.

particles significantly affect the wave rise times, and as such can influence the effective plastic dissipation and temperature behind the deformation wave. Figures 5.2(a) and (b) depict the predicted Hugoniot curves for metalized meso-structures ($\lambda_m = 0.2$) in the $\bar{P}$-U_p plane. Here U_p represents the piston speed and $\bar{P}$ is the effective quasi-steady pressure behind the wave defined as $\bar{P} = (\bar{P}_e\bar{\phi}_e + \bar{P}_m\bar{\phi}_m)/(\bar{\phi}_e + \bar{\phi}_m)$. The variables $\bar{P}_e$, $\bar{P}_m$ are the effective explosive (HMX) and metal (Al) pressures respectively, and $\bar{\phi}_e$, $\bar{\phi}_m$ are the effective

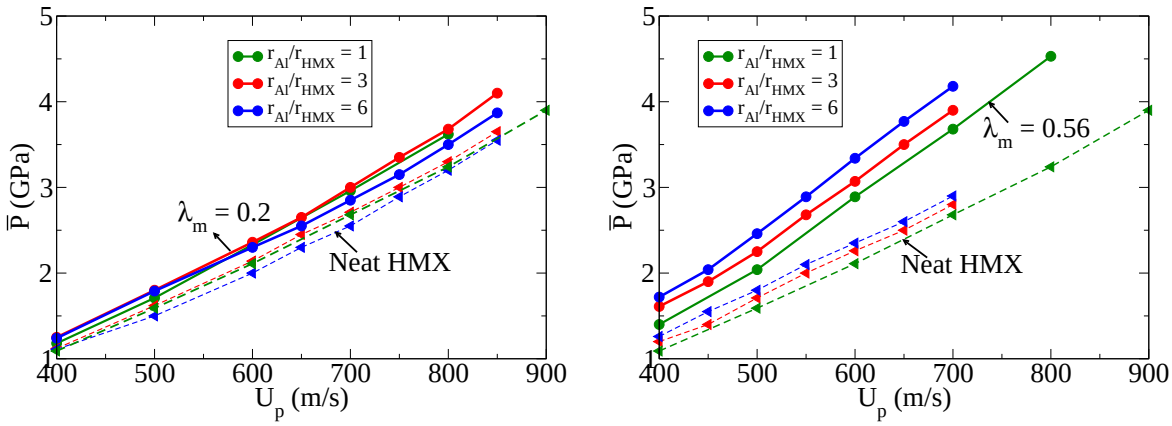

(a) (b)

Figure 5.2: Predictions for the effects of particle size on Hugoniots in the $\bar{P}$-U_p plane for various metal mass fractions: (a)$\lambda_m = 0.2$; (b)$\lambda_m = 0.56$. Also shown are the predictions for the corresponding neat HMX formulations.

explosive and metal volume fractions behind the deformation wave. For neat HMX, $\bar{P} = \bar{P}_e$. In Figure 5.2(a), for a fixed metal mass fraction $\lambda_m = 0.0$ or $\lambda_m = 0.2$, marginal differences are predicted in $\bar{P}$ between meso-structures EM 1($CR = 3$) and EM 2 ($CR = 6$) and EM 3 ($CR = 1$). These marginal variations in effective pressure are associated with the small differences in their effective packing densities. Once again, the inclusion of metal is found to increase the effective pressures behind the wave for all the meso-structures due to the high acoustic impedance of Al which causes the reflection of acoustic energy at the Al-HMX interface leading to larger pressures within the explosive component. As discussed before, larger effective pressures within the meso-structure leads to enhanced dissipation within the material due to enhanced plasticity of the explosive particles.

In Figure 5.2(b), the value of $\bar{P}$ is found to be higher in EM 5 ($CR = 6$, $\lambda_m = 0.0$, 0.56) for both neat and metalized meso-structures compared to the corresponding formulations of EM 4($CR = 3$, $\lambda_m = 0.0$, 0.56), and EM 6 ($CR = 1$, $\lambda_m = 0.0$, 0.56). There are different variations within the meso-structures that contribute to this prediction. For the neat HMX formulations most of the observed differences in $\bar{P}$ between EM 4, EM 5, and EM 6 are due to variations in $\bar{\phi}_s$ and the large HMX particles influence the effective pressures minimally. However, for the metalized meso-structures ($\lambda_m = 0.56$) Al particle size also affects the

effective pressures within the material with a noticeable increase in $\bar{P}$ observed with an increase in Al particle size. This observation is due to the following reasons. First, even for inelastic contacts, it is reasonable to assume that the pressure within a particle scales as $P \approx K\delta^m$, [40] where K is a constant which is a function of the material properties and the effective radius of contact between two contacting particles, δ is the compression ratio, and m is a constant. Therefore for a fixed compression ratio, an increase in particle size and/or bulk modulus leads to an increase in K and as such an increase in $\bar{P}$. Additionally, the smaller particles within these meso-structure experience much larger pressures since they are compressed significantly against the interface of the large Al particles which behave as rigid walls due to their lower compressibility.

Figures 5.3(a) and (b) illustrate the effective plastic work $\bar{W}_{pe}$ in the explosive component as a function of U_p corresponding to metal mass fractions of $\lambda_m = 0.2$ and $\lambda_m = 0.56$ respectively. Also shown on the plots are the values for the corresponding neat HMX formulations. An increase in $\bar{W}_{pe}$ is predicted with the inclusion of metal for the entire range of

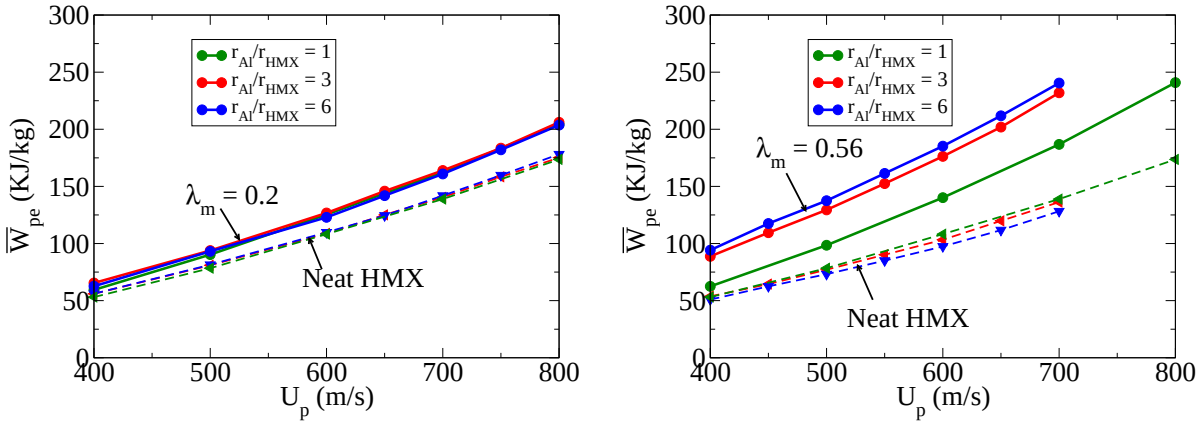

(a) (b)

Figure 5.3: Predicted variations in explosive component effective plastic work $\bar{W}_{pe}$ as a function of U_p for meso-structures with varying particle sizes and metal mass fraction: (a)$\lambda_m = 0.2$; (b)$\lambda_m = 0.56$. Also shown are the predictions for the corresponding neat HMX formulations.

piston speeds. In Figure 5.3(a) for a fixed λ_m ($\lambda_m = 0.0$ or $\lambda_m = 0.2$) only marginal differences in $\bar{W}_{pe}$ between the meso-structures is predicted indicating little effect of particle size.

This is plausible because for $\lambda_m \leq 0.3$ the macro-scale compaction is primarily driven by the explosive-explosive contacts as meso-structures contain few large particles (< 2 % by number fraction). However, an increase in metal fraction $\lambda_m = 0.56$ leads to an increase in the number of large particles ($> 6\%$ by number fraction) within the material, and therefore the effects of particle size on macro-scale plastic dissipation is evident between meso-structures (Figure 5.3(b)). In Figure 5.3(b) for metalized formulations, a monotonic increase in $\bar{W}_{pe}$ is predicted with an increase in Al particle size. This prediction is reasonable because, an increase in Al particle size results in larger contact surface area between the HMX and Al particles and the impedance mismatch at these interfaces result in the reflection of acoustic energy into the explosive particles resulting in larger plasticity. Additionally, the small explosive particles tend to get pinched between clusters of large Al particles which act as rigid walls due to their high bulk modulus.

As mentioned earlier, an explosive composite is considered to be sensitive if most of the energy input is converted into irreversible thermal energy within the material. Hence, expressing $\bar{W}_{pe}$ as a function of energy/power input is important. Additionally, $\bar{P}$ is an important parameter in determining the shock sensitivity of explosives since experiments observe a strong correlation between shock pressures and the corresponding distance to detonation or time to detonation parameters. As such, macro-scale ignition and growth models commonly use pressure dependent burn rates. Hence it is also useful to express $\bar{W}_{pe}$ as a function of the effective pressure $\bar{P}$. Figure 5.4 shows the variations in $\bar{W}_{pe}$ as a function of power input $\bar{P}U_p$ on a log-log plot. In Figure 5.4(a), a small increase in $\bar{W}_{pe}$ is observed for the metalized ($\lambda_m = 0.2$) formulations compared to the corresponding neat HMX formulations. However for a fixed $\lambda_m = 0.0$ or $\lambda_m = 0.2$, negligible differences in $\bar{W}_{pe}$ is predicted between the meso-structures since the packing densities between EM 1, EM 2 and EM 3 are comparable. This suggests for lower metal mass fractions $\lambda_m < 0.3$ large particles have negligible effect on the bulk dissipation. Once again, increasing the metal fraction from $\lambda_m = 0.2$ to $\lambda_m = 0.56$ results in much larger dissipation within the

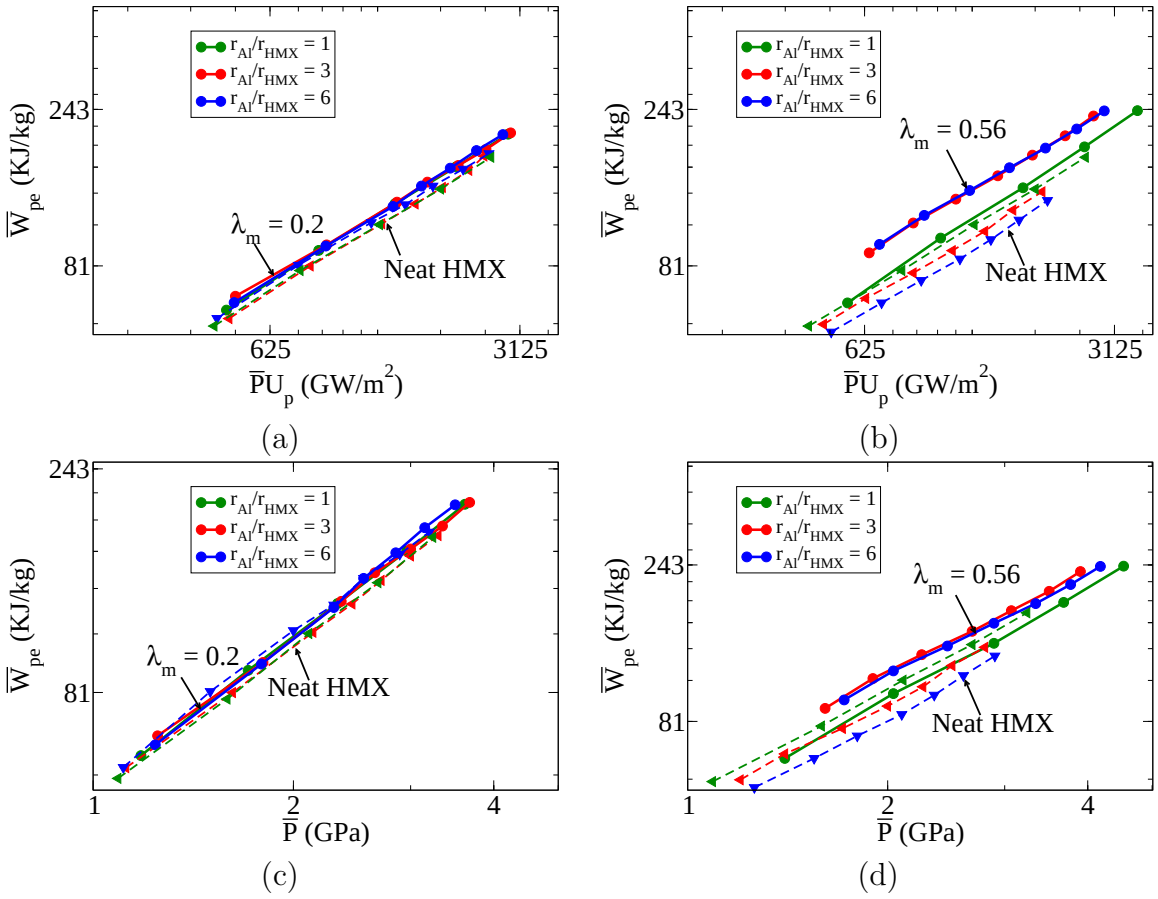

Figure 5.4: Predicted variations in explosive component effective plastic work $\bar{W}_{pe}$ as a function of input power $\bar{P}U_p$ and $\bar{P}$ for meso-structures with varying particle sizes and metal mass fraction: (a)$W_{pe} = f(\bar{P}U_p)(\lambda_m = 0.2)$; (b)$W_{pe} = f(\bar{P}U_p)(\lambda_m = 0.56)$; (c)$W_{pe} = f(\bar{P})(\lambda_m = 0.2)$; (d)$W_{pe} = f(\bar{P})(\lambda_m = 0.56)$.

explosive component compared to the corresponding neat HMX formulations. Also contrary to predictions in Figure 5.4(a), Al particle size is found to have an affect on explosive particle deformation with larger $\bar{W}_{pe}$ values predicted in meso-structures EM 4 and EM 5 compared to EM 6. Similar qualitative observations are made in Figures 5.4(c) and (d) for $\bar{W}_{pe}$ as a function of the effective pressure $\bar{P}$. Another important observation is that the effective plastic work is found to linearly vary with power input and pressure on log-log plot which is qualitatively similar to experimentally observed variations in distance to detonation versus shock pressure which also show a power law relationship. The parameters for $\bar{W}_{pe}$ power law fits as a function of $\bar{P}$ are shown in Table A.7.

In Chapter 4 it was observed that an increase in the packing density and/or λ_m increases D within the material. Variations in particle sizes can also have an effect on the wavespeed [72] due to changes in the granular bed structure. Figures 5.5(a) and (b) show the quasi-steady wave speeds D as a function of U_p for varying metal mass fractions. In Figure 5.5 for

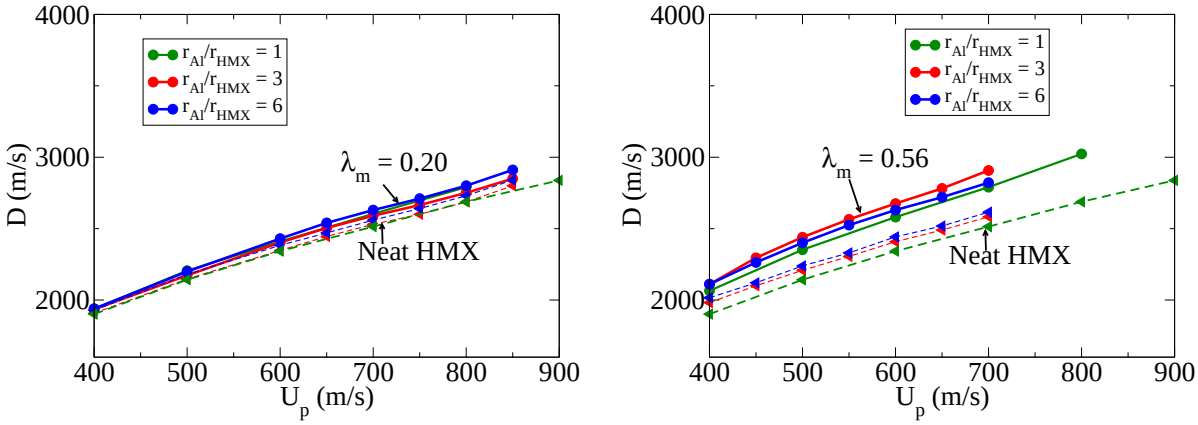

Figure 5.5: Predictions for the effects of particle size on Hugoniots in the D-U_p plane for various metal mass fractions: (a)$\lambda_m = 0.2$; (b)$\lambda_m = 0.56$. Also shown are the values for the corresponding neat HMX formulations.

a fixed metal fraction $\lambda_m = 0.2$ or $\lambda_m = 0.0$ very little variations ($\approx 4\%$) in D is predicted between the meso-structures. This suggests that for $\lambda_m \leq 0.2$, CR and particle distributions have little effect on D compared to the effects of the initial packing density. For higher values of $\lambda_m > 0.3$, D can vary significantly due to variations in particle size, since stress chains of large Al particles can transmit the information (stress waves) faster due to their lower compressibility. Thus, for a given meso-structure increasing the metal fraction from $\lambda_m = 0.2$ to $\lambda_m = 0.56$ increases D noticeably within the material as shown in Figure 5.5(b). In Figure 5.5 two observations are noteworthy. First, neat HMX formulation of EM 5 ($CR = 6$) has marginally higher wavespeeds compared to the corresponding formulations of EM 4 ($CR = 3$), and EM 6 ($CR = 1$) due to its higher initial packing density. However, metalized formulations ($\lambda_m = 0.56$) of the same meso-structures exhibit qualitatively different trends. It is observed that metalized formulation ($\lambda_m = 0.56$) of EM 4 has marginally higher D compared to EM 5 and EM 6. Although speculative at this juncture, the prediction is

plausible because the larger dissipation associated with EM 5 may lead to the weakening of stress wave within that material which results in lower wave speeds.

Figure 5.6 shows the wave rise times as a function of U_p for meso-structures in Table 5.1 with varying particle size and metal mass fractions. Little variations in wave rise times is predicted across the meso-structures indicating that the wave rise times are more a function of the packing density than the particle size or metal mass fractions. In experiments, differences are observed in wave rise times with large variations (order of magnitude) in particle size [72], however because a narrow range of particle sizes are used in this study, large variations in wave rise times are not predicted.

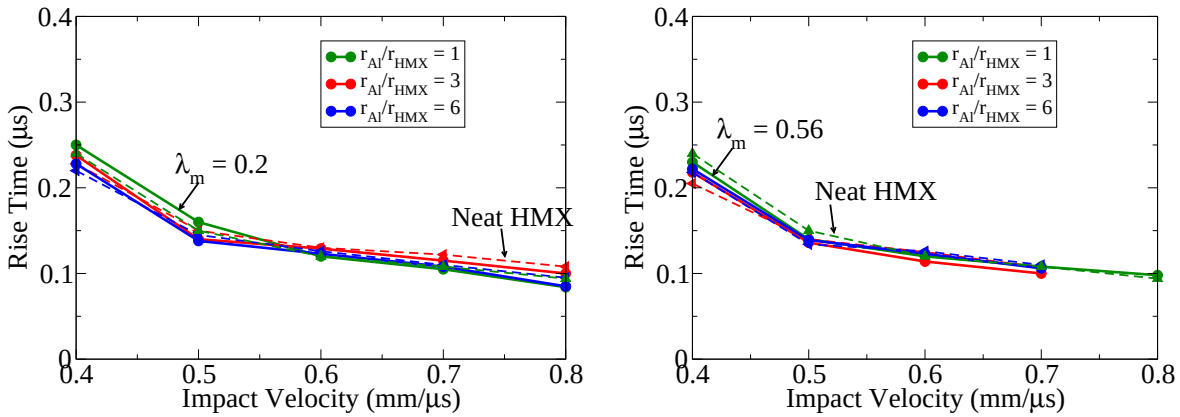

Figure 5.6: Predicted wave rise times for meso-structures with varying particle sizes as a function of U_p: (a)$\lambda_m = 0.2$; (b)$\lambda_m = 0.56$. Also shown are the values for the corresponding neat HMX formulations.

Basically, from all of the discussions in this section, it is evident that for neat HMX meso-structures most of the observed variations in Hugoniots are due to the variations in $\bar{\phi}_s$ resulting from the packing algorithm. The same also holds true for the metalized meso-structures with $\lambda_m = 0.2$ since the macro-scale compaction dynamics in these meso-structures is basically driven by explosive-explosive (small particles) contacts and as such Al particle size has little effect. However for meso-structures with a metal mass fraction of $\lambda_m = 0.56$, a higher number of large Al particles in the material starts to affect the overall Hugoniots in particular $\bar{P}$ and $\bar{W}_{pe}$.

5.2 Overall Hot-Spot Statistics

This section provides the predictions for the overall hot-spot fields. Variations in important hot-spot volumetric properties such as its number density and volume fraction are discussed for meso-structures with varying particle size and metal fractions. Additionally, effects of CR on hot-spot proximity distributions are discussed since they are important in determining hot-spot growth and coalescence. Figure 5.7 shows the predicted hot-spot contours for PE 1 ($CR = 3$) in order to illustrate the effects of larger metal particles on the explosive component hot-spot fields. For comparison, hot-spot contours of the corresponding neat HMX formulations are also shown. In these contours, the red regions represent hot-spots within the particles. Similar observations were also made for $CR = 6$ and therefore are not shown for brevity.

As seen in Figure 5.7, large hot-spots are formed at the interface of Al-HMX particles due to the following reasons. First, for a fixed HMX particle size, the contact area between Al-HMX particles increases with an increase in metal particle size, and the reflection of acoustic energy into the explosive particles at these interfaces results in enhanced particle deformation. Second, Al particles act as rigid walls due to their high bulk modulus (lower compression) and this contributes to the explosive particle deformation. It is important to note that most of the large hot-spots at the Al-HMX interfaces form downstream of the wave (below the large particles). This biasing is due to pinching (compression) of the small HMX particles against the rigid Al particles due to geometric constraints whereas the particles above the large Al particles are less constrained geometrically. It was mentioned in Chapter 4 that along with hot-spot intensity, its size was important in determining its capability to react since large more intense hot-spots can withstand thermal conduction and acoustic cooling losses. As such, these large hot-spots in the vicinity of the Al-HMX particle interfaces may enhance the material sensitivity. On the contrary, the large Al particles that are in contact with these hot-spots may suppress the hot-spot growth by absorbing most of the heat from the reaction. Lower number of hot-spots are predicted in the corresponding

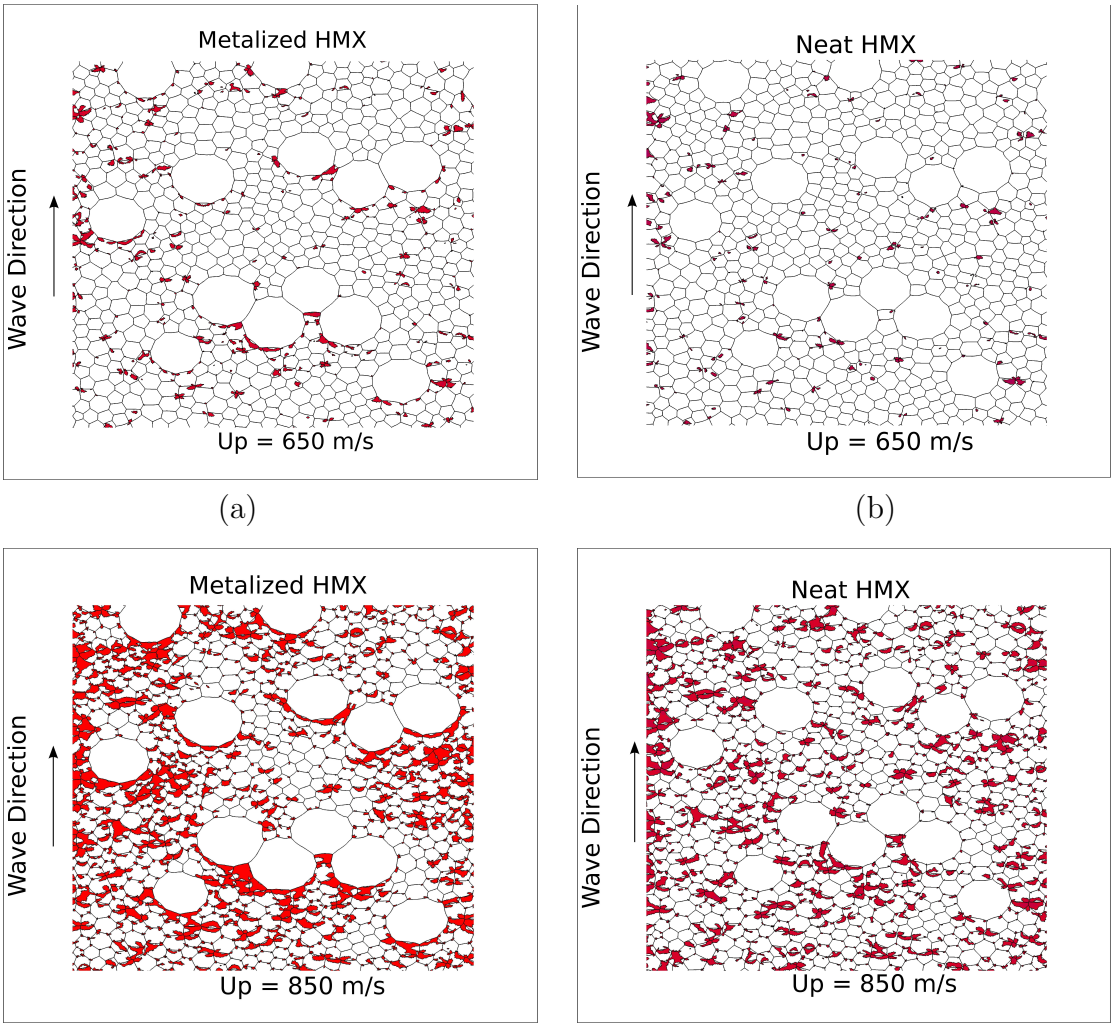

Figure 5.7: Hot-spot contours illustrating the effects of metal particle size on the explosive component hot-spots for meso-structure EM 1. Also shown are the hot-spot fields for the corresponding neat HMX formulations.

neat HMX formulations indicating lower hot-spot number densities. This is contrary to predictions in Chapter 4 wherein the inclusion of metal, was found to decrease the overall hot-spot number density within the material due to dilution effects.

5.2.1 Volumetric Properties

Previously it was discussed that hot-spot volumetric properties may be useful in establishing parameters for macro-scale ignition and growth models. Also, two ways of computing the hot-spot volumetric properties was presented in Chapter 4. For example, if N is the total number of hot-spots in the domain, then the hot-spot number density can be computed

either based on the overall domain area A_T or based on the explosive component area A_e. Mathematically it can be written as $n_{HS} = N/A_T$, and $\tilde{n}_{HS} = N/A_e$. Similarly hot-spot volume fractions can also be computed (Eqn. 4.13). Further it was shown that both of these representations can provide different information about the resulting hot-spot fields. While n_{HS} and ϕ_{HS} values highlight the dilution effect within the metalized meso-structures, $\tilde{n}_{HS}$ and $\tilde{\phi}_{HS}$ values can show the relative increase in dissipation within the explosive component due to the addition of metal.

Figure 5.8 shows n_{HS} and ϕ_{HS} as a function of U_p for metalized meso-structures $\lambda_m = 0.2$ (EM 1, EM 2, and EM 3). Also shown are the volumetric curves for the corresponding neat HMX formulations.

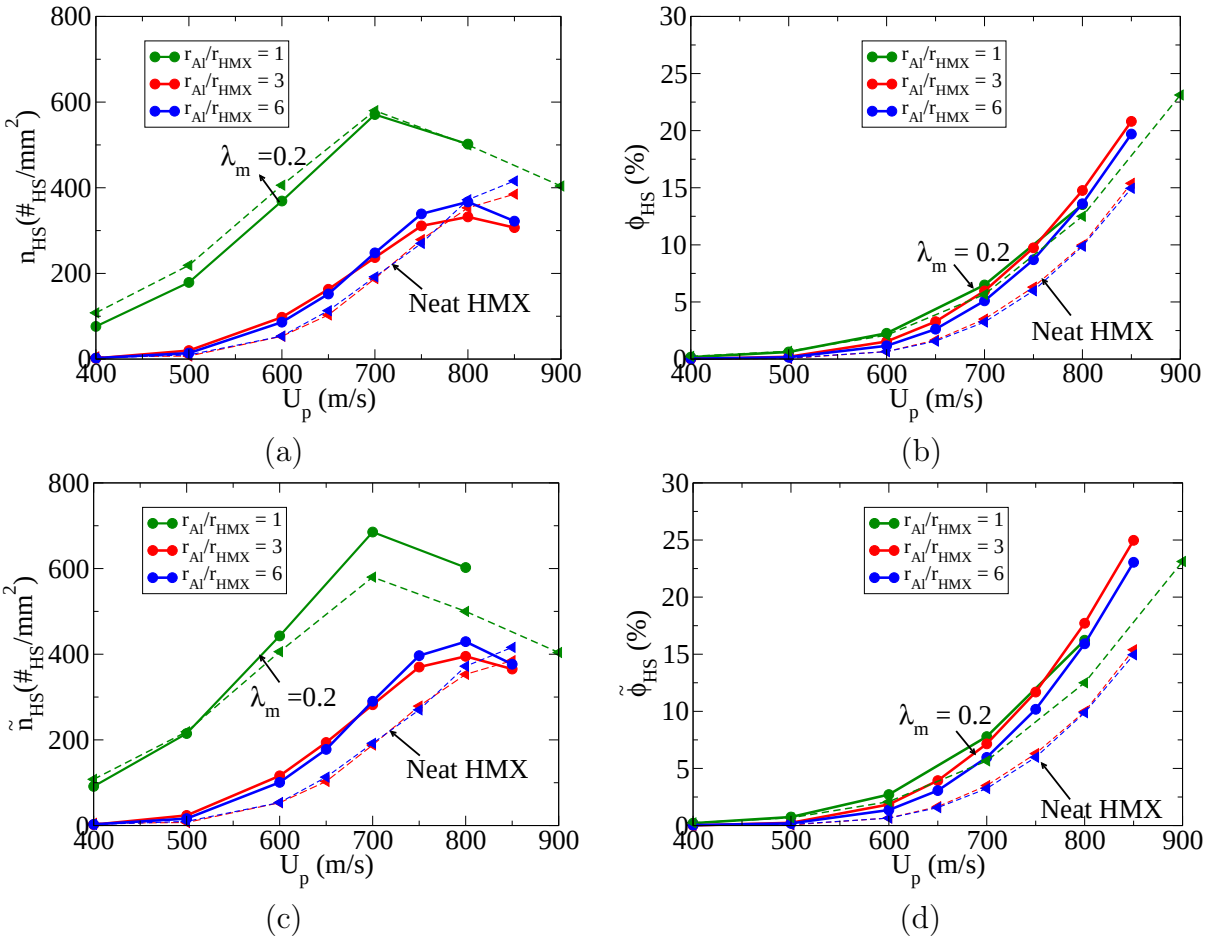

Figure 5.8: Overall hot-spot volumetric properties expressed as a function of piston speed and metal mass fraction $0.0 \leq \lambda_m \leq 0.2$ for meso-structures in Table 5.1: (a)Number density n_{HS}; (b) Volume fraction ϕ_{HS}; (c)Number density $\tilde{n}_{HS}$; (d)Volume fraction $\tilde{\phi}_{HS}$.

In Figure 5.8(a) it is observed that while for meso-structure EM 3 consisting of equally sized Al and HMX particles ($CR = 1$), the inclusion of metal decreases the overall hot-spot number density, an increase in n_{HS} is predicted for EM 1 and EM2 consisting of larger Al particles. Similarly, the hot-spot volume fraction ϕ_{HS} is found to increase substantially in EM 1 and EM 2 with the inclusion of metal. An interesting observation is made for the corresponding neat HMX meso-structures. The n_{HS} curves show that even for neat HMX cases, fewer number of hot-spots are formed in EM 1 and EM 2 compared to EM 3. The reason for this observation is not clearly understood. In meso-structures EM 1 and EM 2 the large particles constitute less than 2 % of the total number of particles. As such, it is reasonable to believe that the compaction dynamics for these neat HMX meso-structures will be dominated by the small HMX-HMX contacts and the hot-spot fields must be somewhat similar since the small HMX particle sizes are identical across these meso-structures ($\bar{r} = 30$ μm). But these results suggest that small variations in the granular bed morphology resulting from the inclusion of large particles can result in significantly different hot-spot fields due to the highly non-linear dependency of hot-spot formation on the contact mechanics. It is important to note that several other scenarios were considered to mitigate any numerical artifacts that can contribute to the substantial variations in hot-spot fields between the neat HMX meso-structures EM 1, EM 2, and EM3. For example, the mesh density of the small particles across the meso-structres were identical. Additionally, it is plausible that these observations are strongly dependent on the choice of the threshold temperature $T_{th} = 500$ K which is used throughout this study. As such even the T_{th} values were varied and the volumetric quantities were recomputed across the neat HMX formulations of EM 1, EM 2, and EM 3. For marginal variations in $T_{th} = 500 \pm 10$ K similar qualitative trends were observed wherein higher number of hot-spots formed within EM 3 compared to EM 1 and EM 2.

Figures 5.8(c) and (d) show the hot-spot volumetric properties $\tilde{n}_{HS}$ and $\tilde{\phi}_{HS}$ computed based on the explosive component area. The predictions are qualitatively similar to that

of the corresponding n_{HS} and ϕ_{HS} values. The plastic work Hugoniots in Figure 5.3 shows that for a fixed λ_m, the overall dissipation in the meso-structures EM 1 ($CR = 3$), EM 2 ($CR = 6$) and EM 3 ($CR = 1$) are similar . However significantly lower number of hot-spots are predicted in EM 1, and EM 2 compared to EM 3. It is important to note that the rate of increase in n_{HS} with U_p or wave strength is equal to the hot-spot formation rate minus the hot-spot agglomeration rate behind the deformation wave. As such for a similar hot-spot formation rate, if the hot-spots agglomerate at a higher rate behind the wave, a decrease in n_{HS} value is possible. This is one of the reasons for the lower values of n_{HS} in EM 1 and EM 2 since for these meso-structures a number of hot-spots agglomerate in the vicinity of the large particles . In essence, the significant variations in hot-spot volumetric properties reiterates the fact that identical amounts of input energy can be dissipated in numerous ways within the heterogeneous explosives leading to vastly different shock response. In the following discussions, only predictions for variations in $\tilde{n}_{HS}$ and $\tilde{\phi}_{HS}$ with meso-structure and U_p are presented since the n_{HS} and ϕ_{HS} values can be computed by using just simple scaling arguments.

Figures 5.9(a) and (b) illustrate the variations in $\tilde{n}_{HS}$ and $\tilde{\phi}_{HS}$ for meso-structures as a function of U_p and metal mass fraction $0.2 \leq \lambda_m \leq 0.56$. In Figure 5.9(a) for each meso-structure, an increase in λ_m results in increased hot-spot formation due to enhanced plasticity of explosive as a result of inreased pressures within the meso-structure. Additionally, for $\lambda_m = 0.56$, lowest number of hot-spots are predicted in meso-structure EM 5 ($CR = 6$). However, qualitatively different trend is observed for $\tilde{\phi}_{HS}$ in Figure 5.9(b) wherein larger $\tilde{\phi}_{HS}$ are predicted for meso-structures EM 4 ($CR = 3$, $\lambda_m = 0.56$), and EM 5 ($CR = 6$, $\lambda_m = 0.56$) compared to EM 6 ($CR = 1$, $\lambda_m = 0.56$) because of substantial plastic deformation of explosive particles that are in contact with large Al particles. Once again, the lower values of $\tilde{n}_{HS}$ in EM 4, and EM 5 are due to significant hot-spot agglomeration behind the deformation as a result of increased hot-spot size.

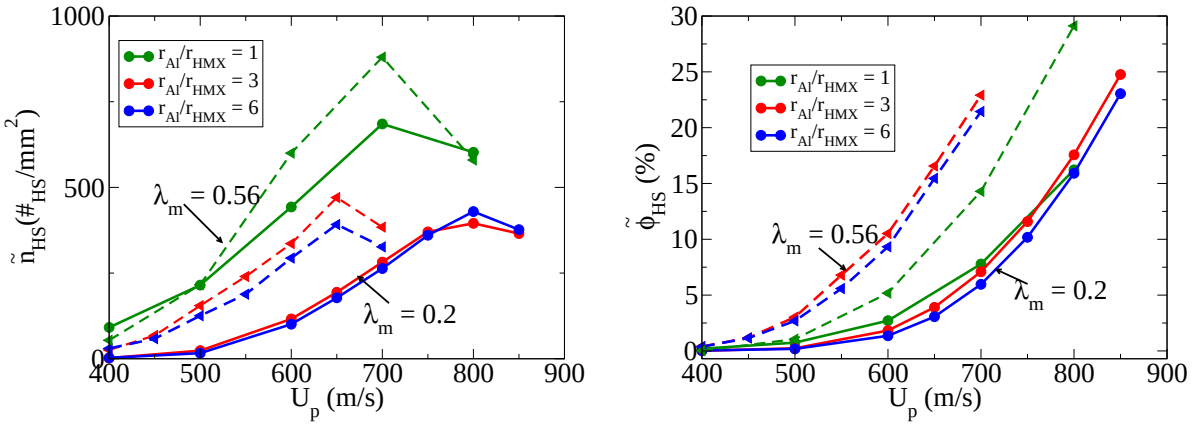

Figure 5.9: Hot-spot volumetric properties expressed as a function of piston speed and metal mass fraction $0.2 \leq \lambda_m \leq 0.56$ for meso-structures in Table 5.1: (a)Number density $\tilde{n}_{HS}$; (b)Volume fraction $\tilde{\phi}_{HS}$.

Figures 5.10(a) and (b) illustrate variations in $\tilde{n}_{HS}$ and $\tilde{\phi}_{HS}$ as a function of power input on a log-log plot for meso-structures with $\lambda_m = 0.2$. Also shown are the corresponding neat HMX curves. In practice, to achieve sustained loading/constant piston speeds for distinct meso-structures requires different power input due to variations in compaction resistance. The variations in compaction resistance between meso-structures arises due to differences in the granular bed morphology. Again, $\tilde{n}_{HS}$ values are larger for EM 3 ($CR = 1$, $\lambda_m = 0.2$) compared to EM 1 ($CR = 3$, $\lambda_m = 0.2$) and EM 2 ($CR = 6$, $\lambda_m = 0.2$) suggesting higher hot-spot formation rates for a given power input. In Figure 5.10(b) for power input of ($\bar{P}U_P \leq 1500\, GW/m^2$) corresponding to piston speeds of $U_p \leq 600$ m/s, significant variations in $\tilde{\phi}_{HS}$ are predicted between meso-structures. But the curves tend to coalescence for stronger power inputs. The significant variations in $\tilde{\phi}_{HS}$ are due to sensitivity of localized surface dissipative mechanisms like friction or frictionally induced plasticity (surface tractions) to granular bed morphology (contact mechanics) with most of the hot-spots in EM 1 and EM 2 forming in the vicinity of the large Al particle interfaces for low power inputs. Also, for a given power input, metalized meso-structures EM 1 and EM 2 have higher $\tilde{\phi}_{HS}$ values compared to that of the corresponding neat HMX meso-structures. This is contrary to the observation in meso-structure EM 3 which consists of equally sized Al and HMX particles

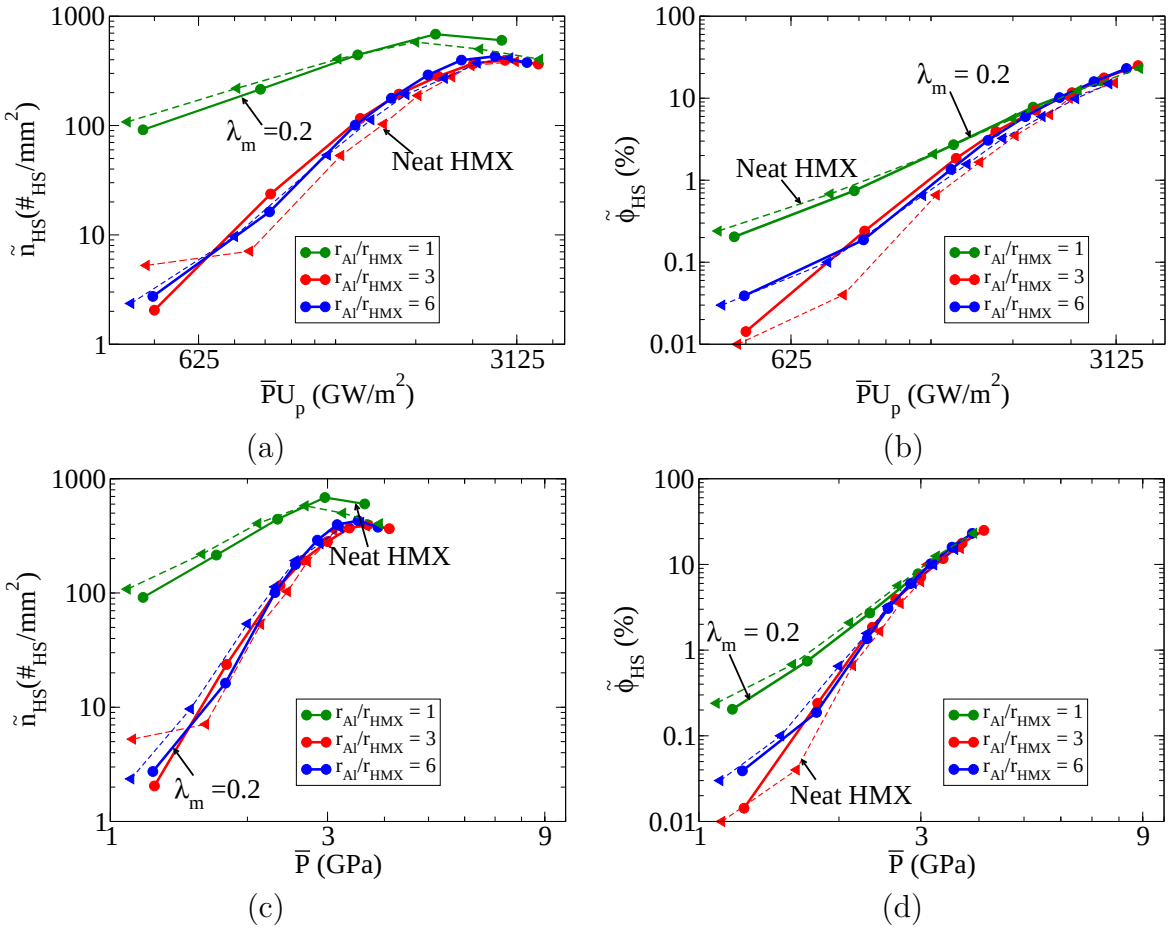

Figure 5.10: Hot-spot volumetric properties expressed as a function of power input $\bar{P}U_p$ and effective pressure $\bar{P}$ for a metal mass fraction $0.0 \leq \lambda_m \leq 0.2$ for meso-structures in Table 5.1: (a) Number density $\tilde{n}_{HS} = f(\bar{P}U_p)$; (b)Volume fraction $\tilde{\phi}_{HS} = f(\bar{P}U_p)$; (c)Number density $\tilde{n}_{HS} = f(\bar{P})$; (d)Volume fraction $\tilde{\phi}_{HS} = f(\bar{P})$.

wherein a reduction in hot-spot volume fraction and number density is predicted in metalized formulations due to dilution effect. Figures 5.10(c) and (d) show the variations in $\tilde{n}_{HS}$ and $\tilde{\phi}_{HS}$ as a function of $\bar{P}$. As mentioned earlier, most experiments observe a power law relation between distance to detonation or time to detonation of an explosive with the pressure within the material. As such, ignition and growth models commonly use a pressure dependent burn rate equation. Unlike the predictions in Chapter 4, the predicted hot-spot volumetric curves are both found to exhibit a non-linear trend with wave pressure. This observation is possible since disparate particle sizes can significantly influence the contact mechanics thereby leading to distributions that may not be described using simple power

law expressions. For example, at low wave pressures $\bar{P} < 2.5$ GPa, most of the hot-spots form near the large metal particles, however at higher pressures, hot-spots also form at the small HMX particle contacts. Numerical experiments indicated that for metalized meso-structures consisting of large Al particles, non-linear power law fits of the form of $\log(f(P)) = a\log(P)^2 + b\log(P) + c$ better fit the data. As such, non-linear power law fits were used to describe the functional relationships between the hot-spot volumetric quantities and the effective wave pressure. Table A.8 lists the best fit parameters for these non-linear power law fits.

Figures 5.11(a) and (b) illustrate the variations in hot-spot volumetric properties as a function of λ_m and input power. Similar to predictions in Figure 5.11(a), for $\lambda_m = 0.56$ higher $\tilde{n}_{HS}$ values are predicted for meso-structure EM 6 consisting of equally sized explosive and metal particles. Also, an increase in λ_m is found to affect the hot-spot formation rates due to higher number of explosive-metal contacts within the meso-structures. In Figure 5.11(b), the hot-spot volume fraction $\tilde{\phi}_{HS}$ is found to be larger in meso-structures EM 4 ($CR = 3$, $\lambda_m = 0.56$), and EM 5 ($CR = 6$, $\lambda_m = 0.56$) compared to EM 6 ($CR = 1$, $\lambda_m = 0.56$) for a given power input indicating higher dissipation within these materials. Once again it is observed that while for meso-structures EM 4 and EM 5 an increase in λ_m results in increased hot-spot number densities and volume fractions, a decrease in these quantities is observed for meso-structure EM 6 consisting of equally sized Al and HMX particles. Therefore it is reasonable to say that the inclusion of large Al particles within the meso-structure for a fixed HMX particle size, leads to enhanced sensitivity. Similar qualitative trends are predicted when $\tilde{n}_{HS}$ and $\tilde{\phi}_{HS}$ are expressed as a function of the effective mixture pressure $\bar{P}$. Similar to predictions in Figure 5.10 hot-spot volumetric quantities in meso-structures EM 4 and EM 5 exhibit non-linear dependency on wave pressure. The specifics of the non-linear curve fit parameters are listed in Table A.8. These functional relationships between hot-spot volumetric properties and wave pressure/power can be used to ignition times/manifolds as discussed in section 4.7.

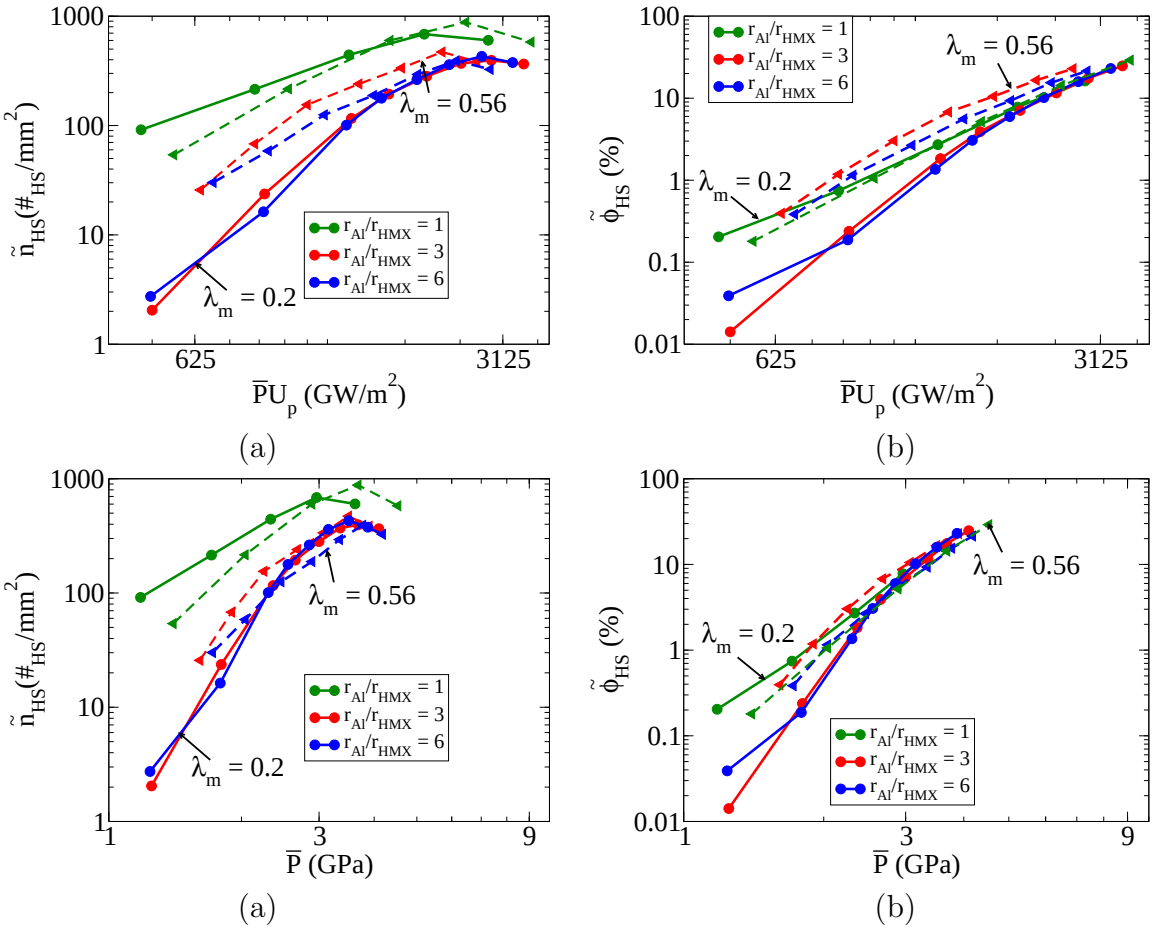

Figure 5.11: Hot-spot volumetric properties expressed as a function of power input $\bar{P}U_p$ and effective pressure $\bar{P}$ for metal mass fractions $0.2 \leq \lambda_m \leq 0.56$ for meso-structures in Table 5.1: (a) Number density $\tilde{n}_{HS} = f(\bar{P}U_p)$; (b)Volume fraction $\tilde{\phi}_{HS} = f(\bar{P}U_p)$; (c)Number density $\tilde{n}_{HS} = f(\bar{P})$; (d)Volume fraction $\tilde{\phi}_{HS} = f(\bar{P})$.

From the predicted values of $\tilde{n}_{HS}$ and $\tilde{\phi}_{HS}$ in Figures 5.10 and 5.11, the average hot-spot size $\bar{A}_{HS}$ can be computed based on the expression $\bar{A}_{HS} = \tilde{\phi}_{HS}/\tilde{n}_{HS}$. Figures 5.12(a)-(d) show the variations in $\bar{A}_{HS}$ for meso-structures in Table 5.1 as a function of piston speed U_p and effective wave pressure $\bar{P}$. From Figure 5.12, it is evident that the average hot-spot size is larger in meso-structures consisting of a bimodal distribution of large and small particles. This is due to the creation of large hot-spots in the vicinity of the large particle interfaces (Figure 5.7). As mentioned before, the agglomeration of hot-spots even at low speeds results in lower number densities in these materials.

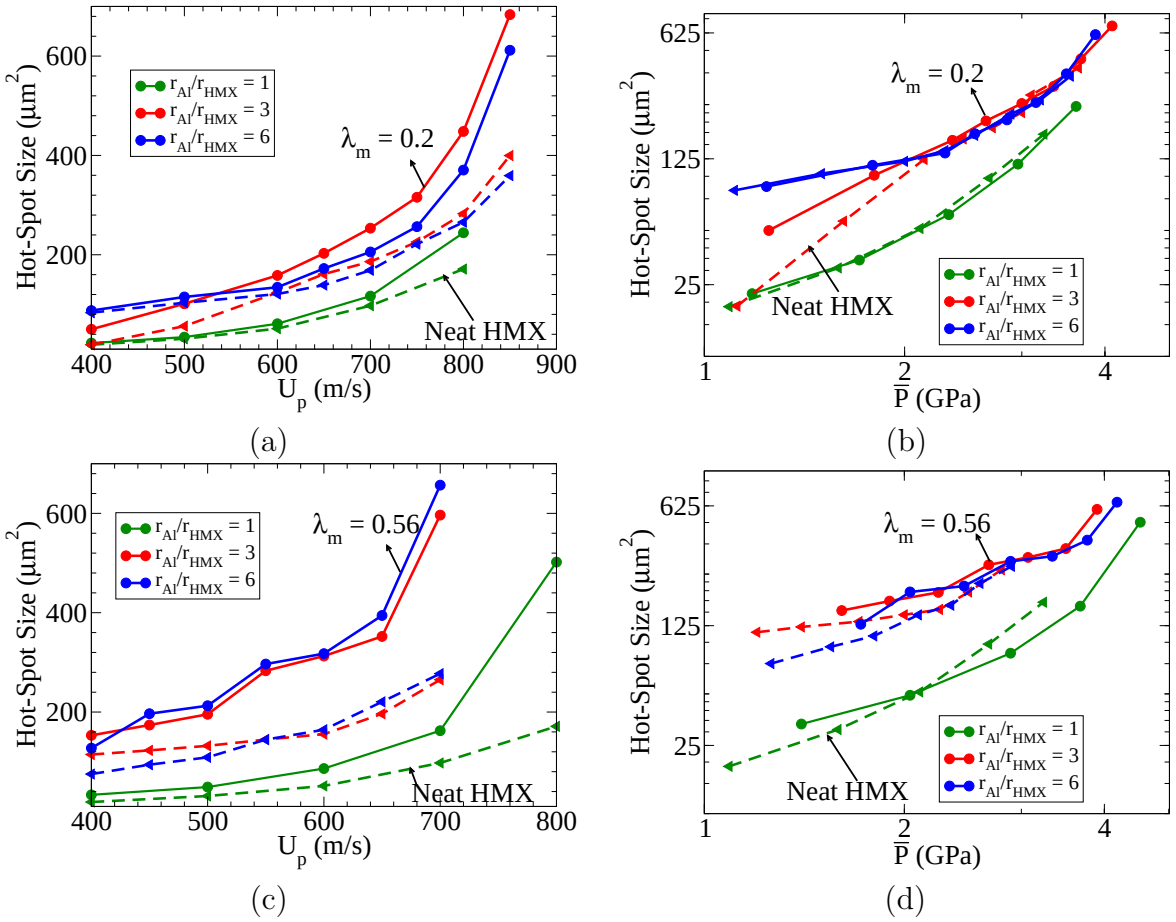

Figure 5.12: Predicted average hot-spot size $\bar{A}_{HS}$ for meso-structures in Table 5.1 for $0.0 \leq \lambda_m \leq 0.56$ as a function of U_p and $\bar{P}$: (a)$\bar{A}_{HS}$-$f(U_p)$; (b)$\bar{A}_{HS}$-$f(\bar{P})$; (c)$\bar{A}_{HS}$-$f(U_p)$; (d)$\bar{A}_{HS}$-$f(\bar{P})$.

Even for neat HMX meso-structures, significantly higher number of hot-spots were predicted in EM 3 compared to EM 1 and EM 2. There are two major differences between the meso-structures. Meso-structures EM 1 and EM 2 consist of both small HMX (r = 20-40 μm), and large HMX particles ($r > 90$ μm) whereas EM 3 is entirely composed of small HMX particles (r = 20-40 μm). The second major difference is in the distributions of the small particles between these meso-structures. While, EM 1 and EM 2 consist of a Gaussian distributions of small particles, EM 3 consists of a uniform distribution of small particles. As such, it is not possible to definitively say as to whether it is the large particles within the material that influence the hot-spot fields significantly or if the variations in the hot-spot fields are primarily due to changes in the particle size distributions of the small particles

(Uniform vs Gaussian). Since only a few large HMX particles exist in meso-structures EM 1 and EM 2 it is reasonable to believe that compaction dynamics is primarily driven by the small HMX particles contacts. As such another meso-structure EM 7 was created wherein the large particles had a size distribution identical to the one in EM 1, however the small particle sizes within this meso-structure had a uniform distribution as opposed to a Gaussian distribution. Therefore, if significant differences in the hot-spot fields still exists between EM 7 and EM 3 then it is clear that most of the observed variations are due to the large particles which alter the granular bed morphology. Figures 5.13(a) and (b) illustrate the variations in hot-spot volumetric properties between EM 3 and EM 7 as a function of U_p. Significant differences still exists between the two meso-structures which means that most of the observed variations in the hot-spot fields are due to the large particles in the meso-structure and not due to the variations in the particle size distributions (Uniform vs Gaussian) of the small HMX particles.

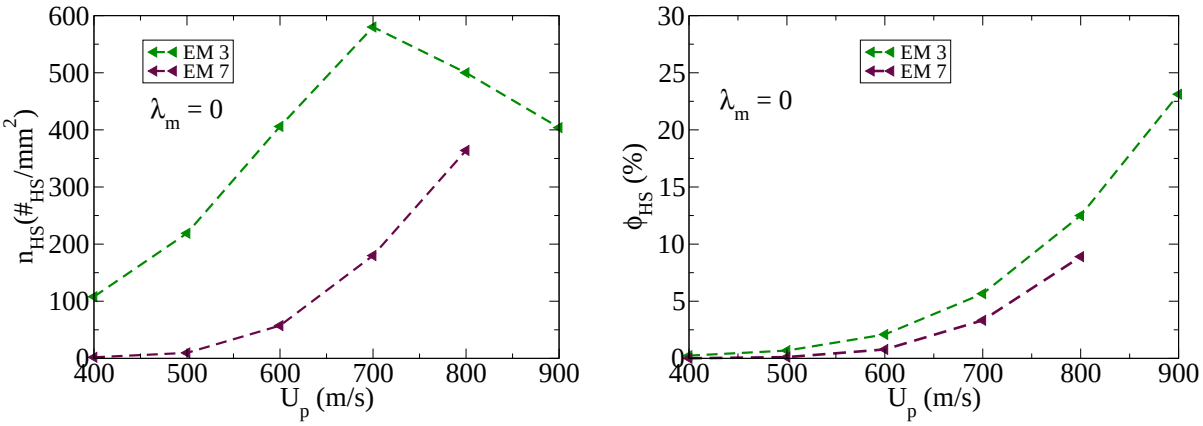

Figure 5.13: Predictions highlighting the influence of large particles on the hot-spot fields: (a)Number density n_{HS}; (b)Volume Fraction ϕ_{HS}

5.2.2 Hot-Spot Proximity

Figures 5.14(a) and (b) show the predicted CDFs for $r_{s,s}$ distributions in metalized meso-structures ($\lambda_m = 0.2$) corresponding to $U_p = 500$, 800 m/s respectively. Also shown are the corresponding $r_{s,s}$ distributions for neat HMX. As mentioned earlier, CDFs for $r_{s,s}$

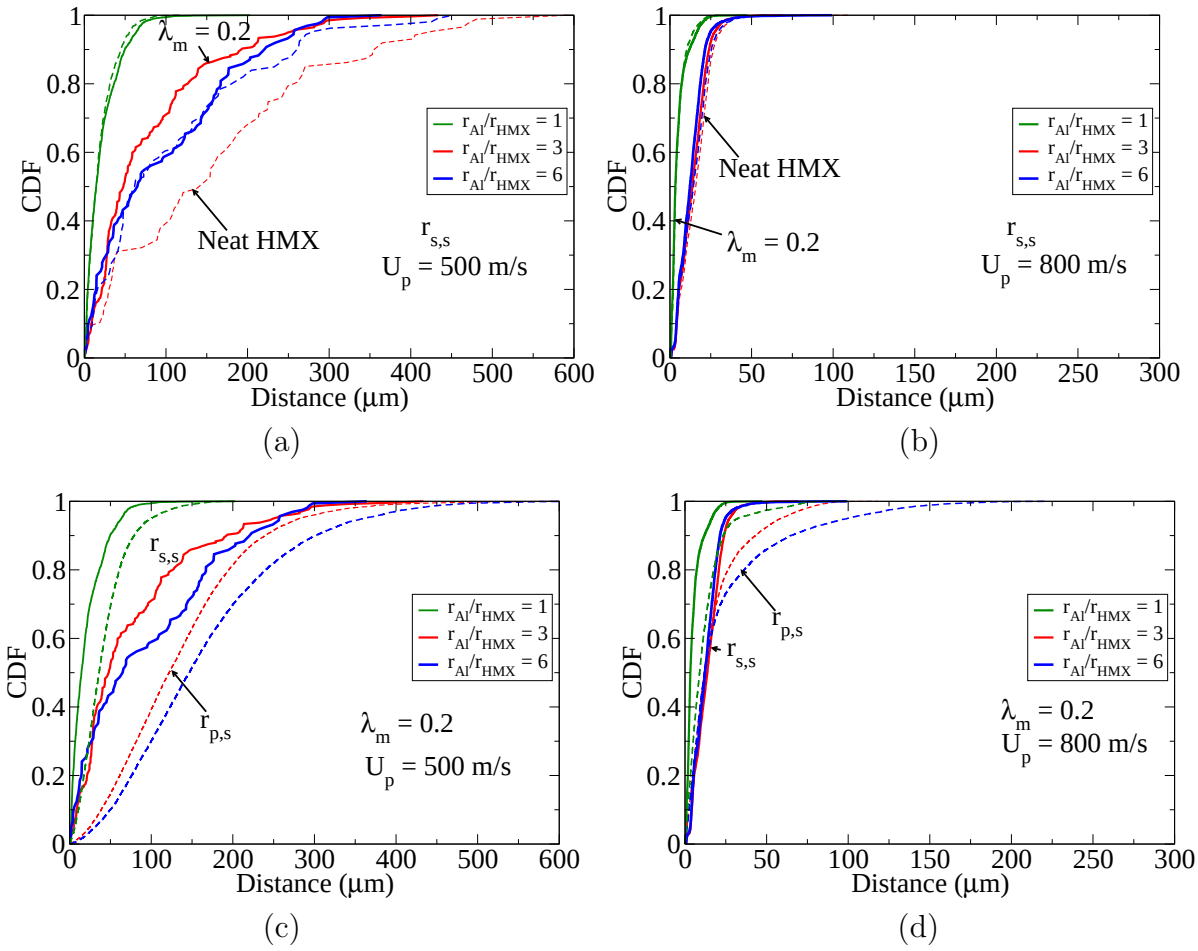

Figure 5.14: Hot-spot proximity CDFs ($r_{s,s}$, $r_{p,s}$) for meso-structures with varying particle sizes (Table 5.1) as a function of piston speed: (a)$r_{r,s}$-U_p = 500 m/s; (b)$r_{r,s}$-U_p = 800 m/s; (c)($r_{r,s}$, $r_{p,s}$-U_p) = 500 m/s; (d)($r_{r,s}$, $r_{p,s}$)-U_p = 800 m/s.

distributions provides details about the proximity of the hot-spots, and this is important with respect to material sensitivity since it affects hot-spot growth and coalescence. In Figure 5.14(a) it is observed that variations in CR have a significant effect on the nearest neighbor distances between hot-spots due to changes in the granular bed morphology. First, meso-structure with $CR = 1$ results in more closely spaced hot-spots compared to meso-structures with larger Al particles ($CR = 3, 6$). This observation is consistent with the number density curves as shown in Figure 5.8(a) wherein substantially larger number of hot-spots are predicted in EM 3 which results in lower hot-spot separation. In Figure 5.14(a), the average $r_{s,s}$ values for metalized meso-structures EM 1 ($CR = 3$), EM 2 ($CR = 6$), and EM 3 ($CR = 1$) are 77.74 μm, 94.67 μm, and 21.07 μm respectively. The corresponding values

for neat HMX meso-structures consisting of identical particle size distributions are 160.77 μm, 106.80 μm, and 19.25 μm. An increase in impact speed $U_p = 800$ m/s, results in stresses within the explosive which is much larger than its yield strength. Hence, this results in an exponential increase in hot-spot formation, and therefore the corresponding hot-spot fields are fairly uniform across the meso-structures. Since substantial number of hot-spots form within each meso-structure, only marginal variations in the average $r_{s,s}$ values are predicted between the meso-structures. In Figure 5.14(b) for $U_p = 800$ m/s, the average $r_{s,s}$ values for metalized meso-structures EM 1 ($CR = 3$), EM 2 ($CR = 6$), and EM 3 ($CR = 1$) are 14.06 μm, 12.83 μm, and 5.05 μm respectively. The values in the corresponding neat HMX meso-structures are 15.81 μm, 14.73 μm, and 4.96 μm.

It was discussed earlier that surface to surface $r_{s,s}$ distribution coupled with point to surface $r_{p,s}$ distribution provides information on spatial clustering of hot-spots. For a isotropic homogeneous hot-spot field, the two distributions collapse into a single curve. However, a larger spread between the distributions suggests spatial clustering of hot-spots. Figures 5.14(c) and (d) show the predicted CDFs for $r_{s,s}$ and $r_{p,s}$ distributions in metalized meso-structures ($\lambda_m = 0.2$) corresponding to an impact speed of $U_p = 500$, and 800 m/s. In Figure 5.14(c), the spread between the $r_{s,s}$ and $r_{p,s}$ distributions is larger in meso-structures EM 1 ($CR = 3$) and EM 2 ($CR = 6$) compared to EM 3 ($CR = 1$). The greater spread is due to the clustering of hot-spots in the vicinity of the large Al particle boundaries. In EM 3, the hot-spot field is more uniform within the meso-structure since the number densities are much large due to the formation of a large number of small hot-spots (4-8 FE). At $U_p = 800$ m/s, noticeable differences still exists between $r_{s,s}$ and $r_{p,s}$ distributions for meso-structures EM 1, and EM 2.

Figures 5.15(a) and (b) show the variations in $r_{s,s}$ distributions between meso-structures for an increased metal mass fraction of $\lambda_m = 0.56$ corresponding to $U_p = 500$ and 700 m/s. Also shown are $r_{s,s}$ curves for the corresponding neat HMX formulations. As mentioned, an increase in λ_m increases the number of explosive-metal contacts within the meso-structures

and this may be important particularly for meso-structures consisting of larger metal particles (contact mechanics). In the hot-spot $\tilde{n}_{HS}$ curves shown in Figure 5.9 substantial

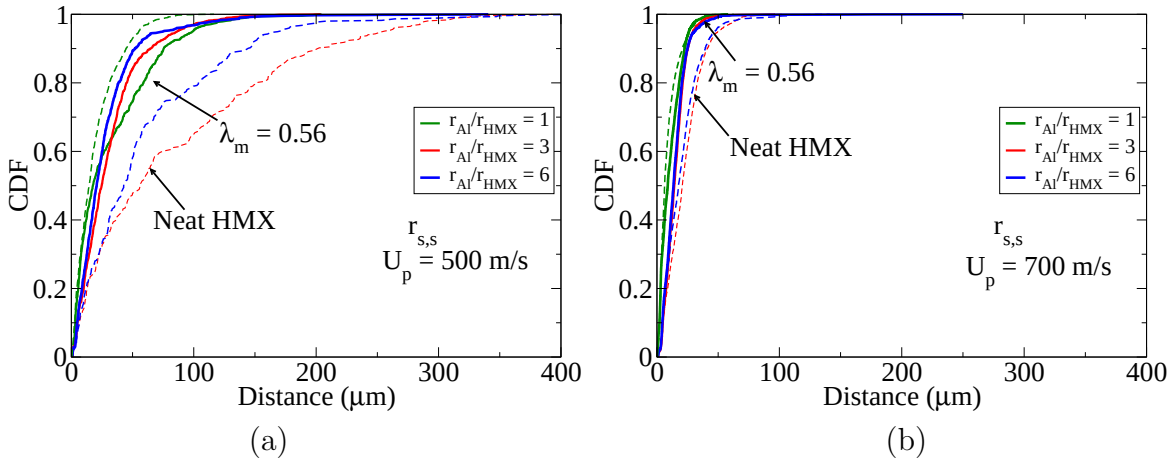

Figure 5.15: Hot-spot proximity CDFs $r_{s,s}$ for meso-structures with varying particle sizes (Table 5.1) as a function of piston speed and metal mass fraction $\lambda_m = 0.56$: (a)$U_p = 500$ m/s; (b)$U_p = 700$ m/s.

increase in hot-spot formation rates were predicted with an increase in λ_m. In Figure 5.15(a) the following observation is noteworthy. Compared to the $r_{s,s}$ values in the corresponding neat HMX formulations, metalized formulations of EM 4 ($CR = 3$, $\lambda_m = 0.56$), and EM 5 ($CR = 6$, $\lambda_m = 0.56$) have lesser separation between hot-spots, while for EM 6 ($CR = 1$, $\lambda_m = 0.56$) an increase in hot-spot separation is predicted with the inclusion of metal due to the dilution effect. In Figure 5.15(a), the average $r_{s,s}$ values for metalized meso-structures EM 4, EM 5, and EM 6 are 30.96 μm, 27.47 μm, and 31.89 μm respectively. The values for the corresponding neat HMX formulations are 84.43 μm, 60.07 μm, and 19.25 μm. Once again, for $U_p = 700$ m/s, the hot-spot fields across meso-structures are more uniform and therefore, this results in lower average values of $r_{s,s}$ for both metalized and the corresponding neat HMX meso-structures. The average $r_{s,s}$ values for metalized ($\lambda_m = 0.56$) meso-structures EM 4, EM 5, and EM 6 are 15.05 μm, 14.79 μm, and 10.79 μm respectively, whereas the $r_{s,s}$ values in the corresponding neat HMX formulations are given by 22.46 μm, 20.31 μm, and 9.05 μm. It is important to note that because the inclusion of larger Al particles results in smaller separation between hot-spots for high metal mass fractions ($\lambda_m = 0.56$), these

meso-structures may exhibit faster transit times to a global ignition event. However, the larger Al particles may hinder hot-spot growth and coalescence by absorbing heat before the onset of any significant chemical activity within the explosive.

5.3 Critical Hot-Spot Statistics

Figures 5.16(a) and (b) show the variations in critical hot-spot $\tilde{n}_{HS}$ and $\tilde{\phi}_{HS}$ for meso-structures with $\lambda_m = 0.2$ corresponding to various piston speeds. Also shown are the volumetric property curves for the corresponding neat HMX formulations. In Figure 5.16, variations in critical hot-spot volumetric quantities are found to be qualitatively similar to that of the overall hot-spot fields wherein substantial larger number of critical hot-spots form in meso-structure EM 3 ($CR = 1$) compared to that in meso-structures EM 1 ($CR = 3$), and EM 2 ($CR = 6$). Similarly the critical hot-spot volume fractions are predicted to be marginally higher in EM 3 compared to that in EM 1 and EM 2. Once again, this observation is qualitatively similar to the variations in the overall hot-spot volume fractions. It

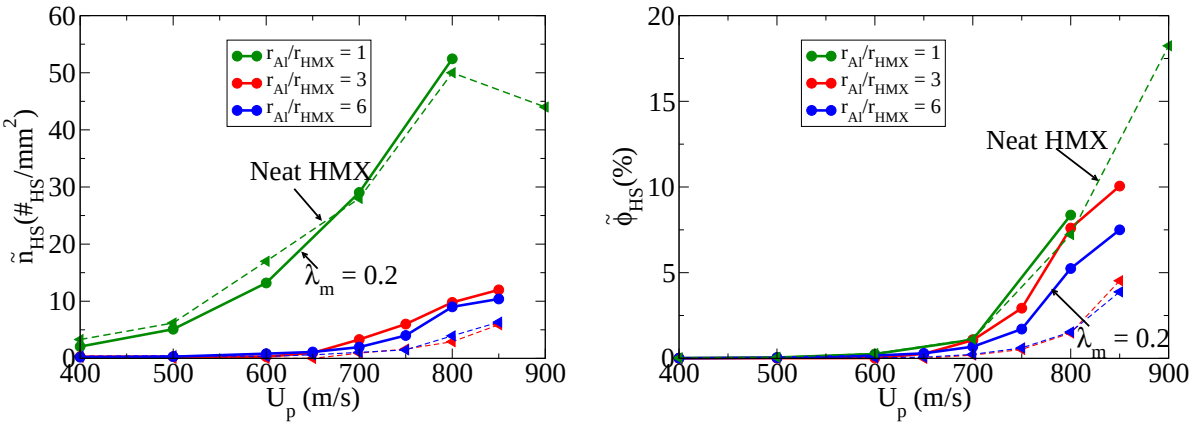

Figure 5.16: Critical hot-spot volumetric properties expressed as a function of piston speed and metal mass fraction $\lambda_m = 0.2$ for meso-structures in Table 5.1: (a) Number density $\tilde{n}_{HS}$; (b)Volume Fraction $\tilde{\phi}_{HS}$. Also shown are the predictions for the corresponding neat HMX.

is important to note that no critical hot-spots were formed within meso-structures EM 1 ($CR = 3$), and EM 2 ($CR = 6$) for $U_p \leq 600$ m/s, whereas around 20-60 critical hot-spots formed within EM 3 ($CR = 3$) for $U_p < 600$ m/s. Since the number density of critical hot-spots in EM 1 and EM 2 is substantially lower compared to that in EM 3, it will take much

longer for these critical hot-spots to thermally interact (larger separation) and therefore it is plausible that including only a few large particles ($< 4\%$) within the meso-structure can lead to a significant decrease in material sensitivity. It is important to note that, without the inclusion of combustion it is impossible to predict the sensitivity of the materials, since the global ignition event is a complex phenomena which is dependent on a myriad of variables and their coupled non-linear dependencies on each other. As such based on the inert meso-scale hot-spot fields, one can only speculate the most likely possibilities based on certain physical reasoning. In the following section prediction is given to estimate local ignition time based on the hot-spot volumetric quantities.

Figures 5.17(a) and (b) show the variations in critical hot-spot number density and volume fraction as a function of λ_m for various piston speeds. As discussed before, an increase in λ_m leads to an increase in the number of Al-HMX contacts facilitating formation of hot-spots in explosive component due to acoustic wave reflections at these interfaces. Contrary

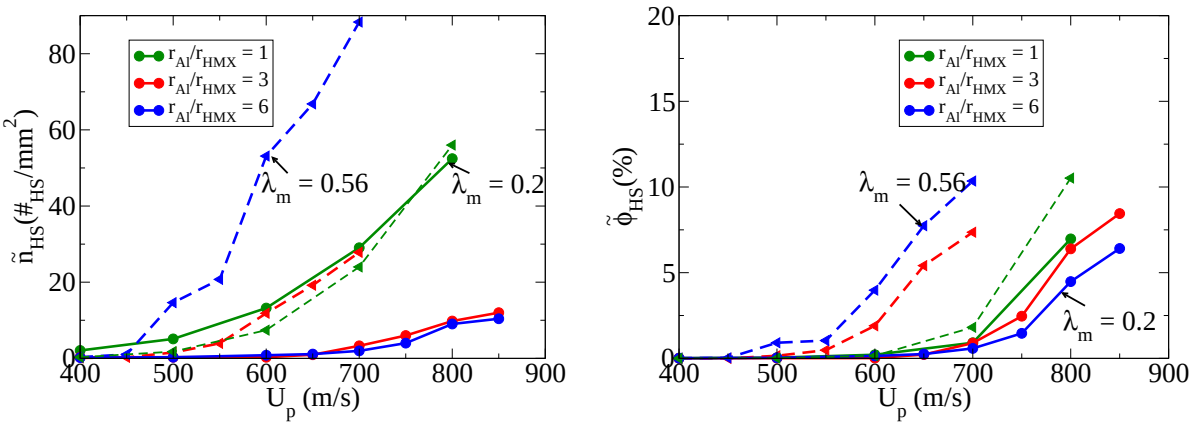

Figure 5.17: Critical hot-spot volumetric properties expressed as a function of piston speed and metal mass fraction $\lambda_m = 0.2, 0.56$ for meso-structures in Table 5.1: (a)Number density $\tilde{n}_{HS}$; (b)Volume fraction $\tilde{\phi}_{HS}$.

to predictions in Figure 5.16, an increase in λ_m from 0.2 to 0.56 results in substantially larger number of critical hot-spots in meso-structures EM 4 ($CR = 3$) and EM 5 ($CR = 6$). Additionally for $\lambda_m = 0.56$ an increase CR from 3 to 6 results in a non-linear increase of critical hot-spot number density for a metal mass fraction of $\lambda_m = 0.56$. Similarly an increase

in Al particle size for $\lambda_m = 0.56$ results in much larger $\tilde{\phi}_{HS}$ values with the material. Since an increase in the number of large reactive hot-spots is observed, for metalized meso-structures EM 4, EM 5 it is reasonable to say that these meso-structures are more probable to exhibit a global ignition event compared to meso-structure EM 1 and EM 2 which have identical particle size distributions but contain fewer number of large Al particles.

Figures 5.18(a) and (b) illustrate the critical hot-spot CDFs for $r_{s,s}$ distributions in meso-structures EM 1 ($CR = 3$, $\lambda_m = 0.2$), EM 2 ($CR = 6$, $\lambda_m = 0.2$), and EM 3 ($CR = 1$, $\lambda_m = 0.2$) corresponding to $U_p = 700$ and 850 m/s respectively. Also shown are the $r_{s,s}$ curves for the corresponding neat HMX formulations. In Figure 5.18(a), the average separation between hot-spots for metalized meso-structure EM 1, EM 2, and EM3 are 321.46 μm, 474.40 μm, and 73.71 μm respectively. The corresponding values for neat HMX meso-structures are 583.93 μm, 684.83 μm, and 52.80 μm. From the average values of $r_{s,s}$ it is evident that while in meso-structures with larger particles, the distances between critical hot-spots decreases with the inclusion of metal, it increases in meso-structure consisting of equally sized Al and HMX particle. Once again, this is due to the clustering of critical hot-spots near the large Al particle boundaries. For $U_p = 850$ m/s, the average distances between critical hot-spots for metalized meso-structures EM 1, EM 2, and EM 3 are 53.65 μm, 103.01 μm, and 38.32 μm respectively. The corresponding values in neat HMX are 126.58 μm, 155.54 μm, and 33.47 μm.

Figures 5.18 (c) and (d) illustrate the CDFs for $r_{s,s}$ distributions in meso-structures EM 4 ($CR = 3$, $\lambda_m = 0.56$), EM 5 ($CR = 6$, $\lambda_m = 0.56$), EM 6 ($CR = 1$, $\lambda_m = 0.56$) corresponding to $U_p = 500$, 700 m/s. Also shown for comparisons are the corresponding $r_{s,s}$ distribution for neat HMX formulations. Similar to predictions in Figure 5.18(a) and (b), lower average values of $r_{s,s}$ is predicted in metalized meso-structures EM 4, and EM 5 compared to the values in neat HMX formulations. However, in EM 6 the opposite trend is predicted with smaller average separation between critical hot-spots for the neat HMX formulation. For $U_p = 600$ m/s, and $\lambda_m = 0.56$ the average $r_{s,s}$ distances between critical

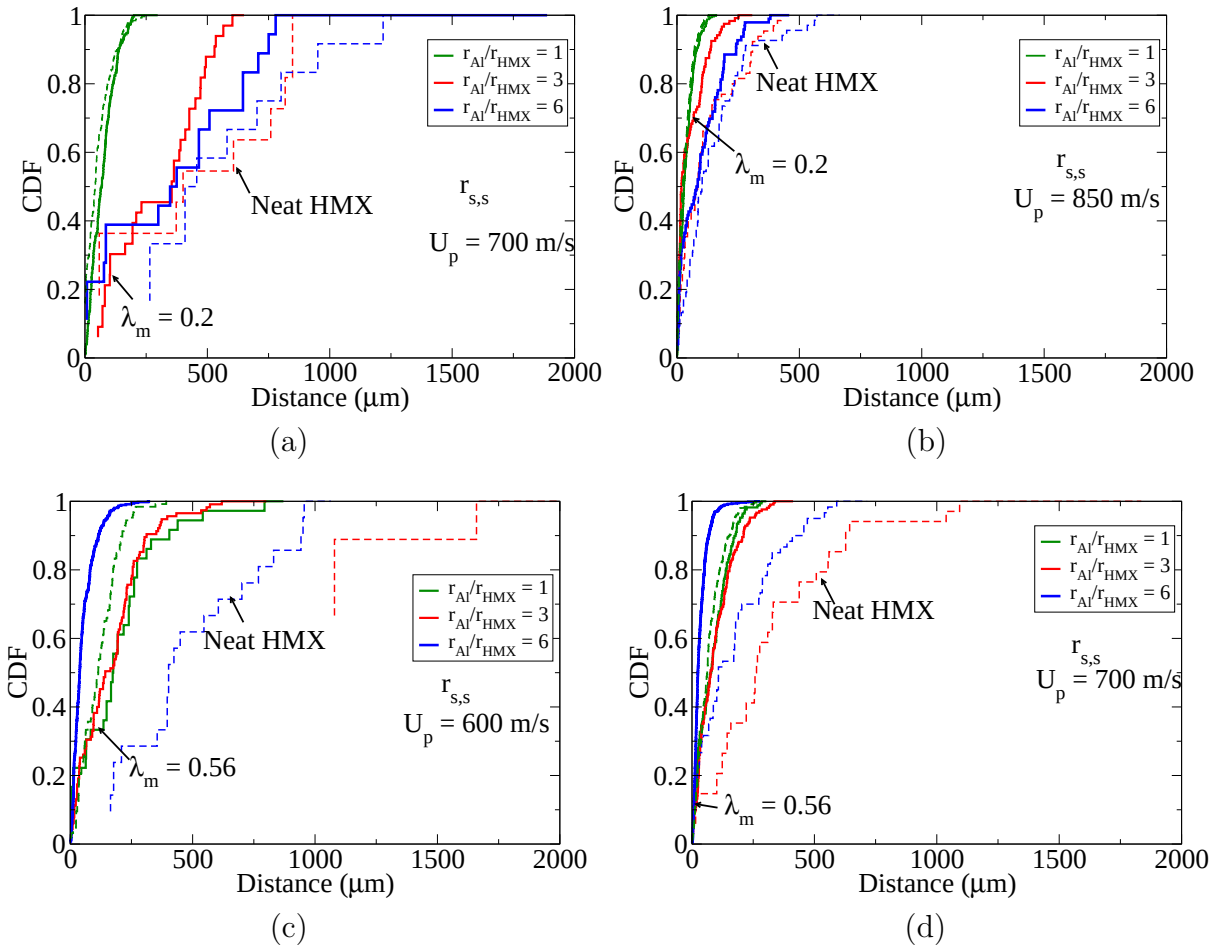

Figure 5.18: Critical hot-spot proximity CDFs $r_{s,s}$ for meso-structures with varying particle sizes (Table 5.1) as a function of piston speed and metal mass fraction $0.2 \leq \lambda_m \leq 0.56$: (a)$U_p = 700$ m/s; (b)$U_p = 850$ m/s; (c)$U_p = 600$ m/s; (d)$U_p = 700$ m/s.

hot-spots in meso-structures EM 4, EM 5 and EM 6 are 174.9 μm, 53.02 μm, 219.46 μm, whereas the values for the corresponding neat HMX formulations are 1555.72 μm, 530.58 μm, and 121.12 μm. Similar observations are also made for $U_p = 700$ m/s, with the predicted average $r_{s,s}$ values for metalized EM 4, EM 5, and EM 6 being 96.10 μm, 33.41 μm, and 85.67 μm respectively. The corresponding values for neat HMX are 377.38 μm, 185.56 μm, and 72.80 μm.

5.4 Meso-structural Stochasticity

The inclusion of disparate particle sizes leads to spatially non-homogeneous meso-structures within the material due to the limitations of the pseudo-gravity settling algorithm used to generate these meso-structure. The main source of material non-homogeneity (stochasticity)

arises due to particle clustering wherein the large particles tend to cluster within the meso-structures as seen in Figure 5.1. Because, the hot-spots form in the vicinity of these large particle boundaries (Figure 5.7), it is plausible that variations in particle clustering may lead to considerable differences in the hot-spot fields. To perform a comprehensive analysis on the effects of particle clustering on hot-spot fields within the meso-structure requires creating a number of meso-structures to obtain statistically meaningful results. However, this requires considerable amount of computational resources and time. As such, one additional meso-structure with identical particle size distribution and composition ($\lambda_m = 0.2$) to EM 1 (Table 5.1) was used to investigate the effects of particle clustering. Though the results may not be statistically meaningful, it still provides valuable information regarding whether the predicted hot-spot volumetric quantities are completely stochastic. It was also observed that compared to the baseline case consisting of equally sized Al and HMX particle size ($CR = 1$), meso-structures with larger Al particle sizes ($CR = 3$ or $CR = 6$) have lower hot-spot number densities and volume fractions for a given wave pressure with much larger differences observed for wave pressures $\bar{P} < 2.5$ GPa, which correspond to piston speeds of $U_p < 600$ m/s. However, little variation in these quantities were predicted between meso-structures with $CR = 3$ and $CR = 6$ (Fig 5.10) for the entire range of wave pressures. This suggests a non-monotonic dependency of the hot-spot volumetric quantities on Al particle size. Hence, three additional meso-structures with an intermediate component size ratio of $CR = 2$ and a metal mass fraction of $\lambda_m = 0.2$ were generated. Once again, the reason for considering multiple meso-structures with ($CR = 2$) is to highlight the effects of large particle clustering on hot-spot volumetric quantities. Table 5.2 provides the specific details for these meso-structures and Figure 5.19 illustrates the additional meso-structures considered in this analysis.

Figure 5.20, shows the variations in overall hot-spot number density $\tilde{n}_{HS}$ and volume fraction $\tilde{\phi}_{HS}$ as a function of U_p and the effective mixture pressure $\bar{P}$ for meso-structures in Table 5.2. Similar to predictions in Figure 5.20, a significant decrease in hot-spot number

Table 5.2: Summary of meso-structures considered in the study to investigate the effects of large particle clustering (stochasticity).

Meso-structure	ϕ_s	Distribution	Mean Particle Radius (μm)	λ_m
EM 1/EM 8	83.7 %	Bimodal	Al $\approx$ 101, HMX $\approx$ 32	0.2
EM 9/EM 10/EM 11	83.5 %	Bimodal	Al $\approx$ 60, HMX $\approx$ 30	0.2

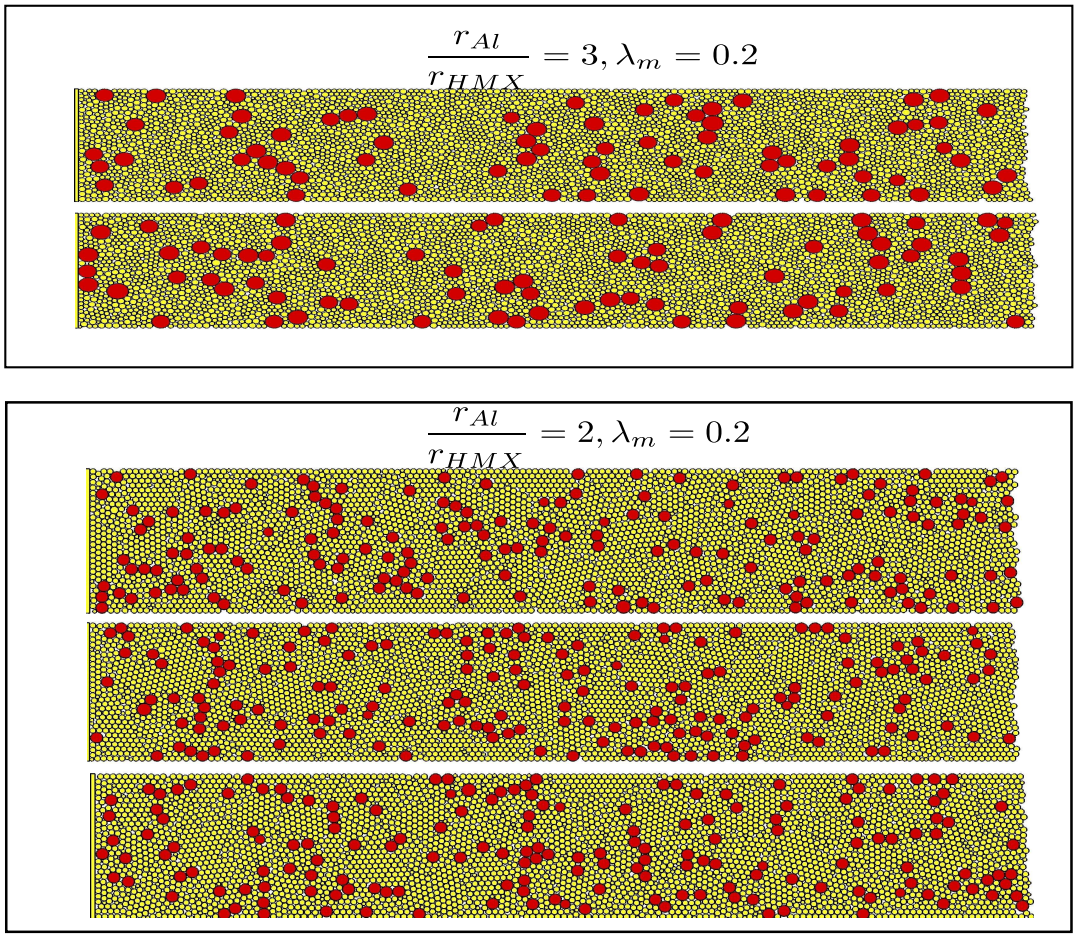

Figure 5.19: Meso-structures considered to investigate the effects of particle clustering on hot-spot fields. Here, red particles represent metal, and yellow particles represent explosive.

density is observed in meso-structures with large Al particles ($CR > 1$) compared to the baseline meso-structure with equally sized Al and HMX particles ($CR = 1$). Also, it is evident that the number density for meso-structures with a component particle size ratio of $CR = 2$ lies between the baseline case of $CR = 1$ and meso-structures with $CR = 3$. This suggests that there is a non-linear dependency of $\tilde{n}_{HS}$ on component particle size wherein for $1 \leq CR \leq 3$ a continuous decrease in $\tilde{n}_{HS}$ is observed whereas a further increase in

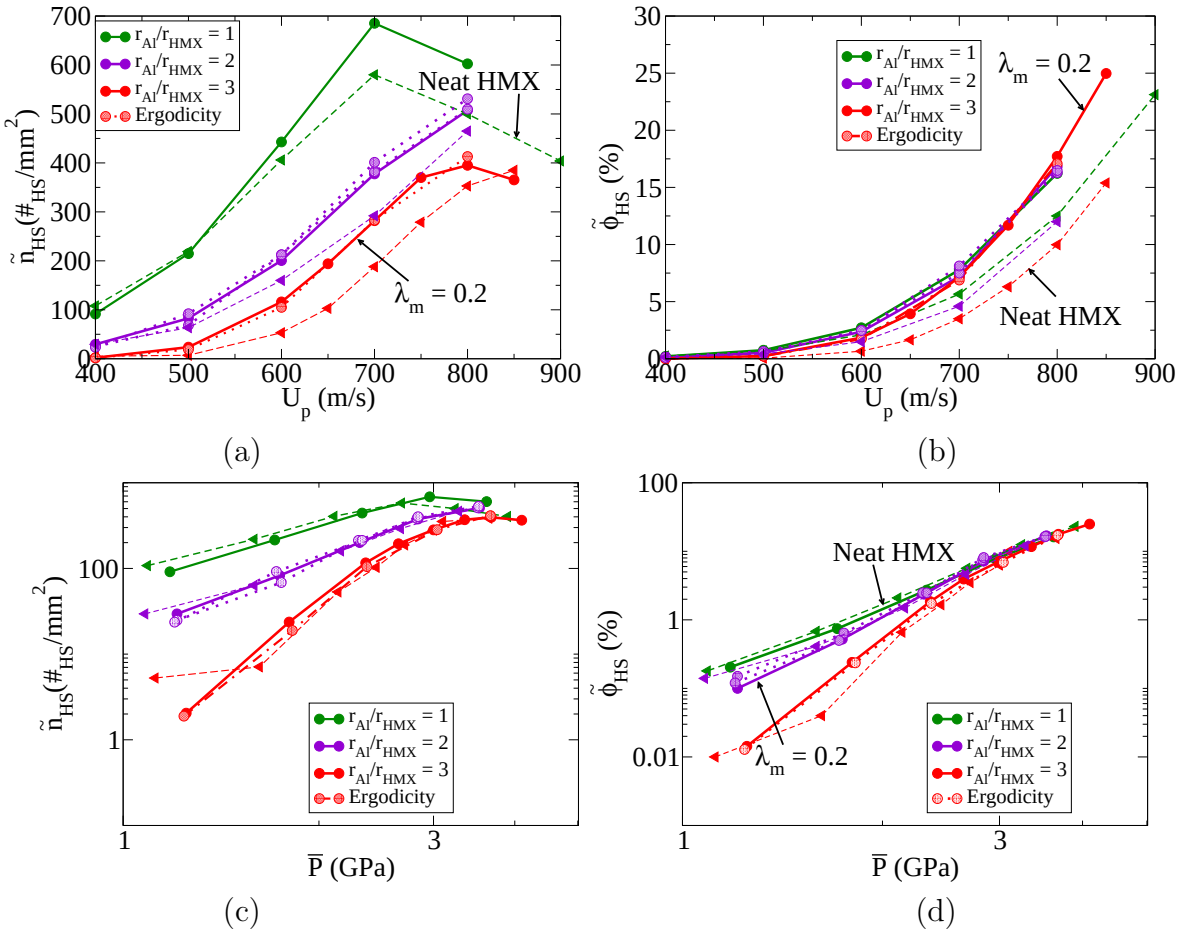

Figure 5.20: Overall hot-spot volumetric quantities expressed as a function of piston speed U_p and effective wave pressure $\bar{P}$ for meso-structures in Table 5.2: (a)$\tilde{n}_{HS} = f(U_p)$; (b)$\tilde{\phi}_{HS} = f(U_p)$; (c)$\tilde{n}_{HS} = f(\bar{P})$; (d)$\tilde{\phi}_{HS} = f(\bar{P})$.

particle size ratio $CR > 3$ has little effect on the hot-spot number density (Figure 5.10). As mentioned before, there are two plausible reasons for the decrease in hot-spot number density. First for $U_p < 600$ m/s a reduction in hot-spot number density is associated with a substantial decrease in hot-spot formation. At impacts speeds of $U_p < 600$ m/s, most of the hot-spots form due to frictional dissipation and/or frictionally induced plasticity arising due to surface tractions. Therefore, it is possible that the changes in the granular bed morphology due to the inclusion of large particles results in lowering of frictional dissipation within the meso-structure. However, for $U_p \geq 600$ m/s, the decrease in hot-spot number density is primarily due to hot-spot agglomeration in the vicinity of the large Al particle interfaces which results in fewer hot-spots with larger area. This is consistent with the predictions in

Figure 5.12, which shows an increase in average hot-spot size for meso-structures with large Al particles. Figure 5.20(b) shows the corresponding variations in $\tilde{\phi}_{HS}$ for various piston speeds. Figure 5.20(c) and (d) show the variations in $\tilde{n}_{HS}$ and $\tilde{\phi}_{HS}$ as a function of $\bar{P}$. Similar to predictions in Figure 5.20(a), a decrease in $\tilde{n}_{HS}$ is predicted with the inclusion of larger Al particles within the material. In Figure 5.20(d), at lower wave pressures $\bar{P} < 2.5$ which corresponds to $U_p < 600$ m/s, significant differences in $\tilde{\phi}_{HS}$ are also observed between the baseline meso-structure ($CR = 1$), and meso-structures consisting of large Al particles ($CR > 1$). As mentioned earlier, this is plausibly due to sensitivity of surface dissipative mechanisms to variations in granular bed morphology. However, at higher wave pressures $\bar{P} > 2.5$ GPa, the $\tilde{\phi}_{HS}$ curves tend to have only marginal differences between the meso-structures. Additionally, from Figure 5.20, it is evident that variations in particle clustering (material stochasticity) minimally affects the hot-spot volumetric quantities.

Figure 5.21 shows the variations in critical hot-spot number density and volume fraction as a function of U_p. Similar to predictions in Figure 5.20, the inclusion of large Al particles results in a significant decrease in critical hot-spot number density within the explosive component. It is important to note that for piston speeds of $U_p \leq 600$ m/s, no hot-spots

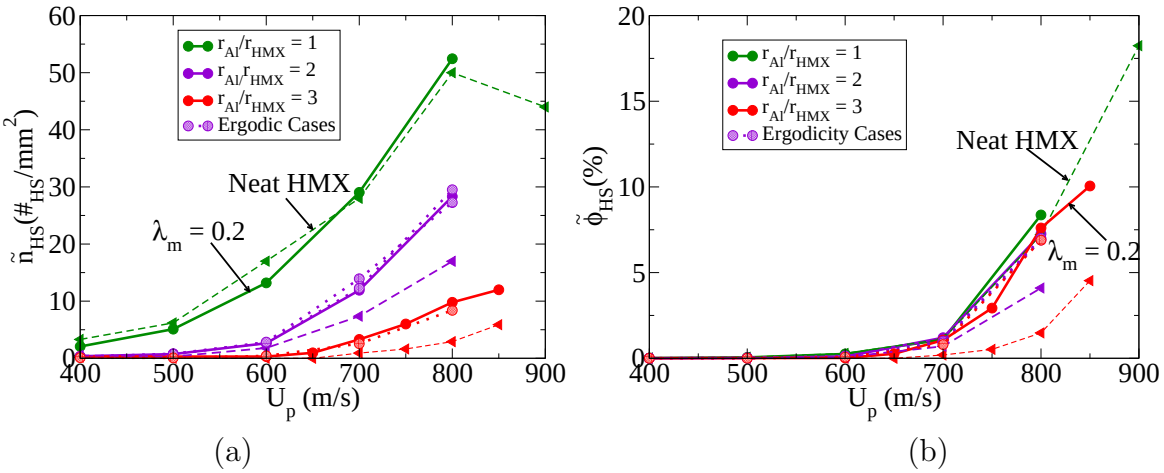

Figure 5.21: Critical hot-spot volumetric quantities expressed as a function of piston speed U_p for meso-structures in Table 5.2: (a) $\tilde{n}_{HS}$; (b) $\tilde{\phi}_{HS}$.

formed within the meso-structures EM 1 and EM 8 and few critical hot-spots (< 10) formed

within the meso-structures with $CR = 2$, to draw any statistically meaningful conclusions. A significant decrease in the critical hot-spots within these materials suggests that the inclusion of large Al particles may suppress the material sensitivity. The reason for the huge variations in hot-spot volumetric quantities especially at lower wave pressures due to the inclusion of large Al particles is not clearly understood. The sensitivity of surface dissipation to particle scale variations in the granular bed morphology is an important question that needs further analysis.

CHAPTER 6
EFFECTS OF MESO-STRUCTURAL STOCHASTICITY

Granular explosives with identical effective values of packing density (ϕ_s), composition (λ_m), particle sizes, and shapes can exhibit vastly different impact/shock responses due to differences in the spatial fluctuations of these properties at smaller scales. Small variations in granular bed structure can affect the stress transmission paths in material, and thereby result in disparate hot-spot fields within these materials. It is assumed that the heterogeneity occurs at meso-scale. Therefore, scales larger than the particle sizes are considered macro-scale in this study. In reality it is impossible to create two explosive formulations which are identical across all length scales. Therefore, experiments investigating the shock/impact response of granular explosives are typically performed on a number of explosive samples that are macroscopically similar, and the final predictions are based on the ensemble averages of these samples. A complete mathematical characterization of a random heterogeneous material is not possible due to the infinite number of variables involved in the problem [78]. A number of studies have tried to statistically characterize the microstructures of the granular materials, and have tried to correlate their effect on the macroscopic behavior of these material [7, 78].

As mentioned throughout this study, the simplest statistical description of a granular meso-structure is to define its effective volume fraction/packing density, component volume/mass fraction, effective particle size and particle shape. It is possible to use higher order statistical descriptors such as N point correlation functions to characterize spatial clustering of particles and/or different phases within the granular material. In this study, meso-structures are generated using a pseudo-gravity settling algorithm by randomly placing particles within a fixed domain. The random placement of particles can result in meso-

structures with identical macroscopic porosity, composition, particle size and shape but varying spatial fluctuations about these values at smaller scales.

The main purpose of this chapter is to investigate how the random seeding of particles within a fixed computational domain affects the macroscopic wave profiles and hot-spot fields in the resulting meso-structures. To this end, ten (10) meso-structures were generated with initial packing density of $\bar{\phi}_s \approx 76\%$. The particle sizes, shapes, and composition ($\lambda_m = 0.0$) across all the meso-structures were identical. The relevant details of the meso-structures are summarized in Table 6.1. Though the effective values of $\bar{\phi}_s$ are similar, the

Table 6.1: Summary of meso-structures considered in the study to investigate the effects of random seeding of particles on hot-spot fields.

Meso-Structure	$\bar{\phi}_s$	σ_{ϕ_s}	Transverse Width (mm) (L_T)	Avg.Size μm	Particle Shape
Ensemble 1	75.85 %	1.14 %	1.5	30	Hexagon:Circular-6:1
Ensemble 2	75.91 %	1.10 %	1.5	30	Hexagon:Circular-6:1
Ensemble 3	75.75 %	1.10 %	1.5	30	Hexagon:Circular-6:1
Ensemble 4	75.83 %	1.10 %	1.5	30	Hexagon:Circular-6:1
Ensemble 5	75.79 %	1.10 %	1.5	30	Hexagon:Circular-6:1
Ensemble 6	75.92 %	1.10 %	1.5	30	Hexagon:Circular-6:1
Ensemble 7	75.80 %	0.75 %	1.3	30	Hexagon:Circular-6:1
Ensemble 8	75.77 %	0.73 %	1.3	30	Hexagon:Circular-6:1
Ensemble 9	75.45 %	1.46 %	1.75	30	Hexagon:Circular-6:1
Ensemble 10	75.68 %	1.44 %	1.75	30	Hexagon:Circular-6:1

spatial fluctuations in ϕ_s varies between meso-structures leading to differences in the standard deviations of the property. Numerical experiments indicated that by increasing the transverse width of the computational domain, larger spatial fluctuations in porosity could be obtained within the meso-structure due to the limitations of the pseudo-gravity settling algorithm. Therefore, the transverse boundary dimensions (L_T) were varied between 1.3-1.75 mm as shown in Figure 6.1. These values of L_T allows us to vary the spatial fluctuations reasonably while maintaining domains that are sufficiently long to enable quasi-steady waves to develop. Additionally, varying L_T will enable us to test the effect of periodic boundary condition on the predicted results. Figure 6.2 shows the 1-D spatial ensemble average of $\bar{\phi}_s(x)$, along

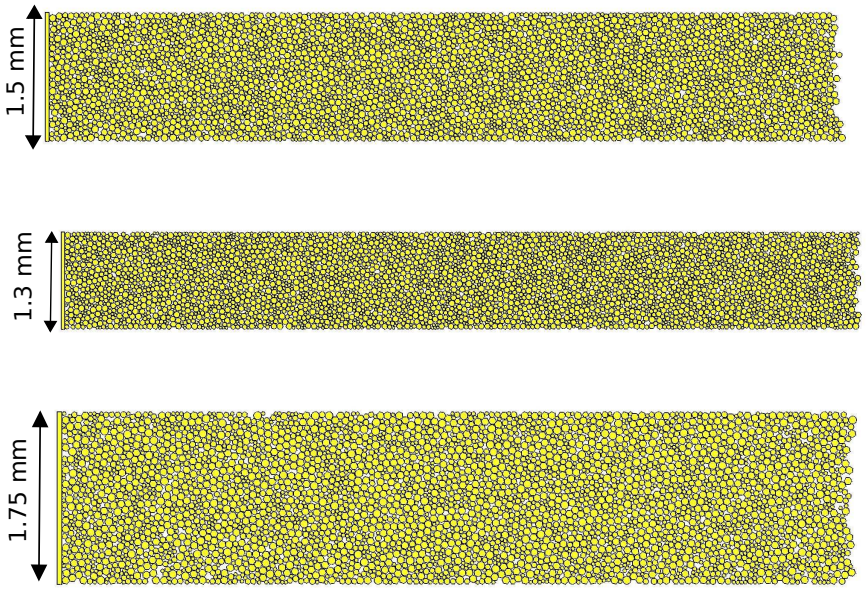

Figure 6.1: Representative meso-structures from Table 6.1 with different transverse boundary widths.

with the the maximum and minimum bounds for the meso-structures in Table 6.1. From Figure 6.2 it is evident that random seeding of particles leads to significant variations in spatial fluctuations of porosity between the meso-structures.

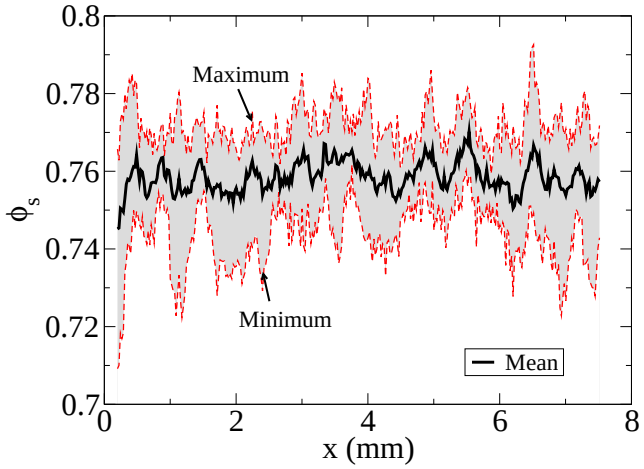

Figure 6.2: Spatial variations in packing density arising due to random seeding.

Hugoniot measurements/predictions are helpful in evaluating parameters used in multi-phase macro-scale models that investigate shock sensitivity of explosives at engineering scale ($O \approx cm\text{-}m$). Figures 6.3(a) and (b) summarize the predicted Hugoniots for all the meso-

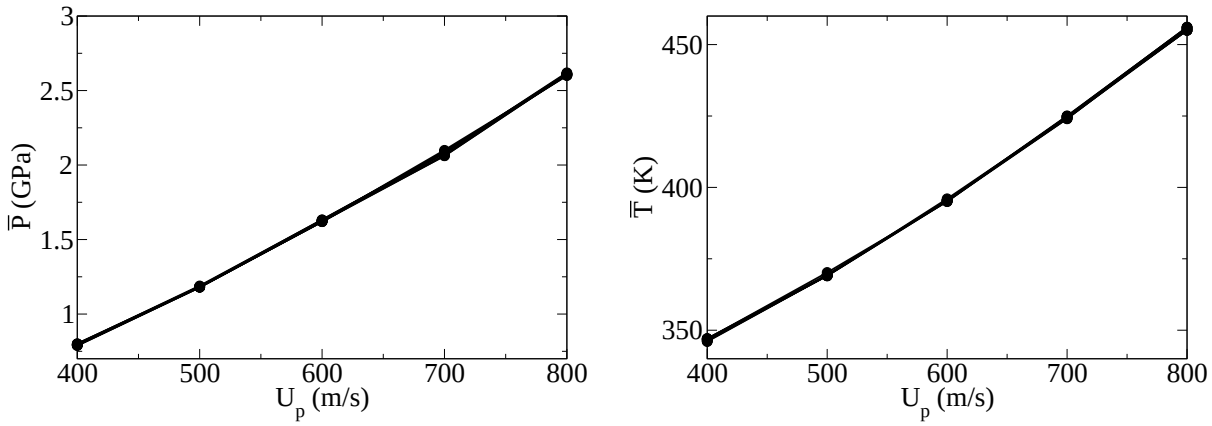

(a) (b)

Figure 6.3: Effective wave end states (Hugoniots) for meso-structures in Table 6.1: (a) $\bar{P}$-U_p; (b) $\bar{T}$-U_p.

structures in $\bar{P}$-U_p and $\bar{T}$-U_p planes. Here $\bar{P}$, and $\bar{T}$ are the effective quasi-steady pressure, and temperature behind the wave. From Figures 6.3(a) and (b) it is evident that the values of $\bar{P}$ and $\bar{T}$ are largely insensitive to spatial fluctuations in ϕ_s.

6.1 Overall Hot-spot Fields

As mentioned, random seeding of particles alters the granular bed leading to significant variations in stress chains within the material. Since hot-spots are likely to form in particles within these stress chains, random seeding of particles could affect the hot-spot fields significantly. Volume specific properties such as hot-spot number density and volume fraction are commonly used in macro-scale ignition and growth models, and therefore it is important to investigate the effects of random seeding on these variables. Again, the analysis considers both the overall hot-spot fields and the critical hot-spot fields. While the overall hot-spot field can affect the transition to detonation of the material, critical hot-spots represent potential ignition sites within the material and therefore influence the early time response of the shocked material.

Figures 6.4(a) and (b) summarizes the variation in the overall n_{HS} and ϕ_{HS} between meso-structures in Table 6.1 by providing the median, maximum and minimum values of these quantities. From Figure 6.4(a) it is observed that random seeding of particles has a small effect on the hot-spot number densities for all impact speeds. Additionally the

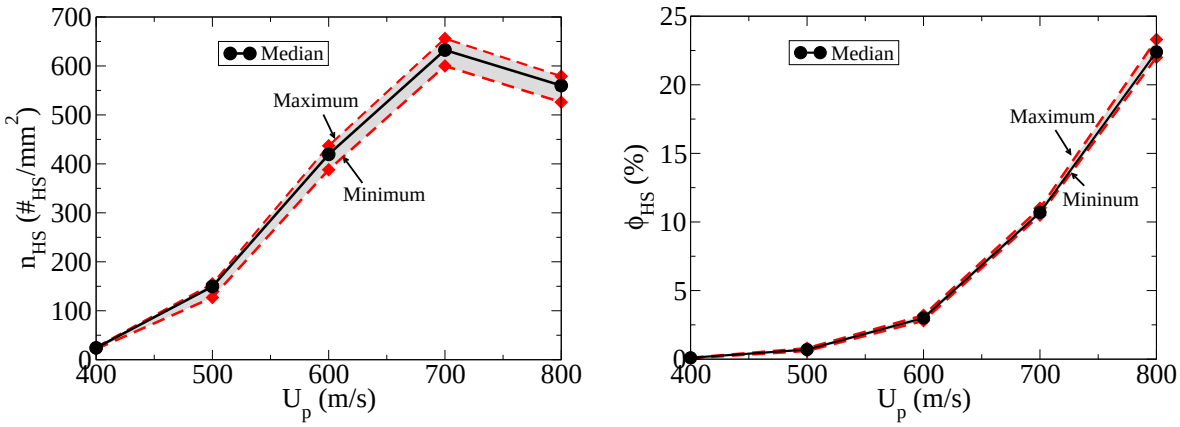

Figure 6.4: Boxplots illustrating the overall hot-spot volumetric properties for meso-structures in Table 6.1 as a function of impact speed: (a) Number density n_{HS}; (b) Volume fraction ϕ_{HS}.

variations in n_{HS} are found to increase monotonically with an increase in U_p. It is important to note that the larger variations in n_{HS} at higher impact speeds are primarily because of an increase in the number of small hot-spots (4-8 finite elements) that form near particle interfaces due to high pressure slip between the particles which are sensitive to fluctuations in the granular bed morphology resulting from random seeding. In Figure 6.4(b), smaller variations in ϕ_{HS} are predicted across the meso-structures for the entire range of piston speeds. This observation is consistent with the argument that most of the observed variations in n_{HS} are due to smaller hot-spot since these hot-spots do not contribute significantly to the hot-spot volume fraction.

Along with the number of hot-spots, the quantity that is most likely to determine the sensitivity of explosives is the spatial proximity of hot-spots. Hot-spots that are spatially clustered together can thermally interact behind the deformation wave and this may be potentially important for a global ignition even to occur.

Figures 6.5(a) and (b) give CDFs for $r_{s,s}$ distributions of the overall hot-spot fields corresponding to $U_p = 500$ and 800 m/s for all the meso-structures. From Figure 6.5(a), noticeable variations in the $r_{s,s}$ distributions exist for $U_p = 500$ m/s while at higher impact speed of $U_p = 800$ m/s the curves tend to coalesce. At $U_p = 500$ m/s, majority of hot-

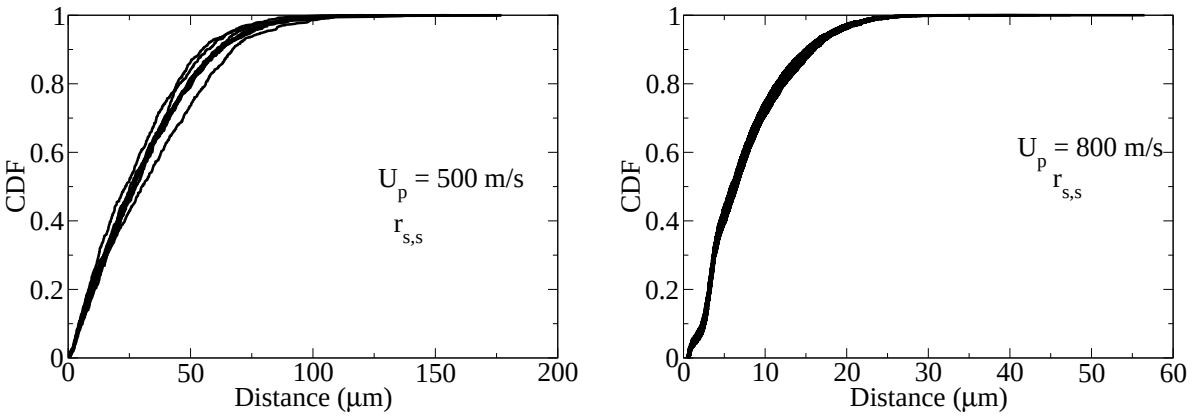

(a) (b)

Figure 6.5: Overall hot-spot surface to surface ($r_{s,s}$) nearest neighbor CDFs for meso-structures in Table 6.1: (a) $U_p = 500$ m/s; (b) $U_p = 800$ m/s.

spots form at the particle interfaces primarily due to localized plasticity and/or frictional dissipation, both of which are sensitive to particle scale fluctuations. The effective maximum and minimum $r_{s,s}$ values across the meso-structures are 34.09 μm and 27.32 μm respectively. These values are roughly about the mean particle radius. However, at higher impact speeds, hot-spots formation is due to significant plastic deformation of particles which affects much of the particle volume, and therefore it is largely insensitive to surface scale fluctuations. An increase in piston speed $U_p = 800$ m/s leads to smaller separation between hot-spots with the effective maximum and minimum $r_{s,s}$ values being 7.81 μm and 7.32 μm respectively.

6.2 Critical Hot-spot Fields

Figures 6.6(a) and (b) summarize the variations in critical hot-spot number density and volume fraction as a function of U_p. Similar to predictions for the overall hot-spot volumetric properties, varying spatial fluctuations between the meso-structures is found to have an effect on the critical hot-spot number density. Again, the variations are found to marginally increase with U_p. Since a hot-spot qualifies as *critical* based on the joint distribution of its area (size) and peak temperature, it is plausible that particle scale fluctuations can affect critical hot-spot fields because, the peak temperatures within a hot-spot are most likely to occur at the particle interfaces. Similarly the variations in the critical hot-spot volume fractions are predicted to marginally increase with an increase in U_p.

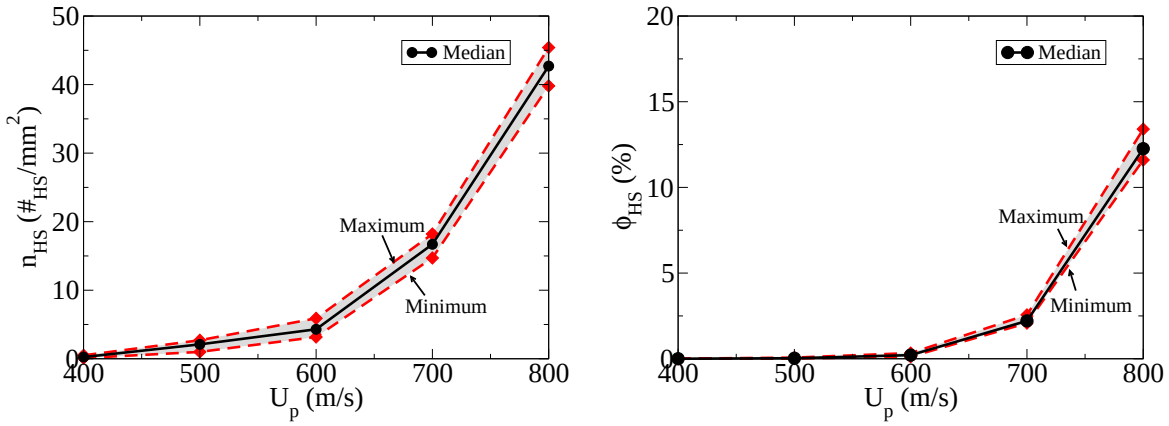

Figure 6.6: Boxplots illustrating the critical hot-spot volumetric properties for meso-structures in Table 6.1 as a function of impact speed: (a) Number density n_{HS}; (b) Volume fraction ϕ_{HS}.

As discussed before, the onset of chemical activity is likely to occur within hot-spots that have enough thermal inertia to overcome conductive losses. If such critical hot-spots are clustered within certain regions of the material, they can coalesce faster and assist in the formation of larger hot-spots that are chemically active. It is possible that non-linear interactions between a few critical hot-spots may eventually lead to a global ignition event. Figures 6.7(a) and (b) show the critical hot-spot $r_{s,s}$ distributions for all the meso-structures corresponding to impact speeds of $U_p = 500$ and 800m/s respectively. For an impact speed of $U_p = 500$ m/s, statistically significant variations in $r_{s,s}$ distributions is predicted. The maximum and minimum values of the average $r_{s,s}$ distances between the meso-structures are found to be 757.8 μm, and 271.7 μm respectively. Therefore, it is likely that materials with similar packing densities may yield significantly different impact/shock response at low speeds. However for an impact speed of $U_p = 800$ m/s, lower deviations are predicted in critical hot-spot $r_{s,s}$ distributions across meso-structures with maximum and minimum $r_{s,s}$ values of 52.9 μm and 47.6 μm respectively. Because substantially larger number of critical hot-spots are formed within the material at high impact speeds, the critical hot-spots fields are statistically similar across the meso-structure and their statistical measures are qualitatively similar to that of the overall hot-spot fields.

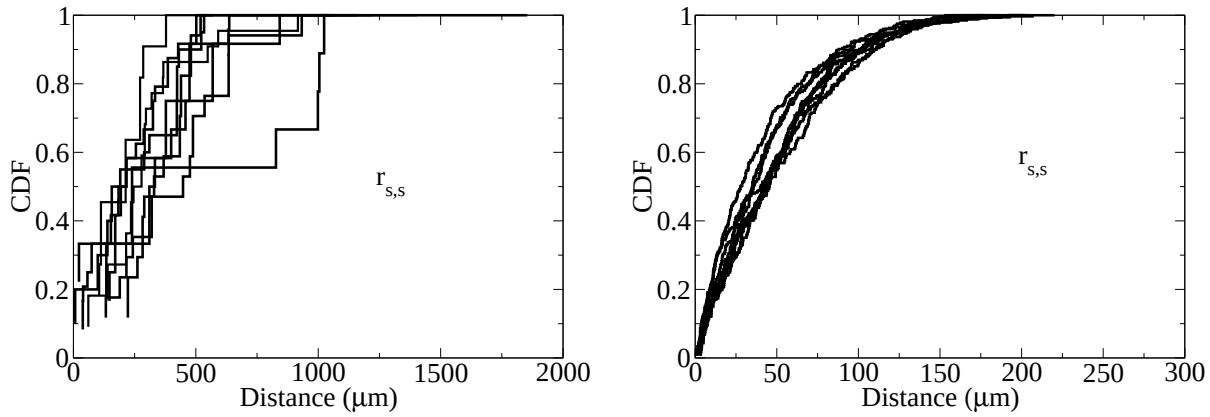

Figure 6.7: Critical hot-spot surface to surface ($r_{s,s}$) nearest neighbor CDFs for meso-structures in Table 6.1: (a) $U_p = 500$ m/s; (b) $U_p = 800$ m/s.

6.3 Effects of Transverse Boundary

In this study, periodic boundary conditions were imposed on the lateral boundaries as mentioned before. Periodic boundary conditions are routinely enforced to simulate a large system by modeling a small part in order to eliminate rigid wall/edge effects. In reality, interactions between rigid walls and the explosive particles (confinement) may be crucial in establishing impact sensitivity of the material due to frictionally induced tractions between particle-wall interfaces. Additionally, wave reflections from the rigid boundaries can amplify the pressures within the material resulting in enhanced plasticity within the material.

The dimensions of the transverse boundary may affect the hot-spot fields because it leads to larger spatial fluctions in porosity within the material. Since plastic pore collapse is a dominant heating mechanism, it is plauisble that large spatial fluctuations in porosity can result in enhanced dissipation within the material. As mentioned earlier, to investigate the effects of transverse boundary width on hot-spot fields, the transverse width of the domain was varied between $1.3 \leq L_T \leq 1.75$ mm. Figures 6.8(a) and (b) illustrate the effects of the transverse boundary width on the overall hot-spot number density and volume fraction respectively. From Figures 6.8(a) and (b) it is observed that the variations in lateral boundary dimension affects the hot-spot field marginally with higher variations in hot-spot number density predicted at higher impact speeds. Similarly, the critical hot-spot volumetric

properties are also found to vary minimally with variations in L_T as seen in Figures 6.9(a) and (b).

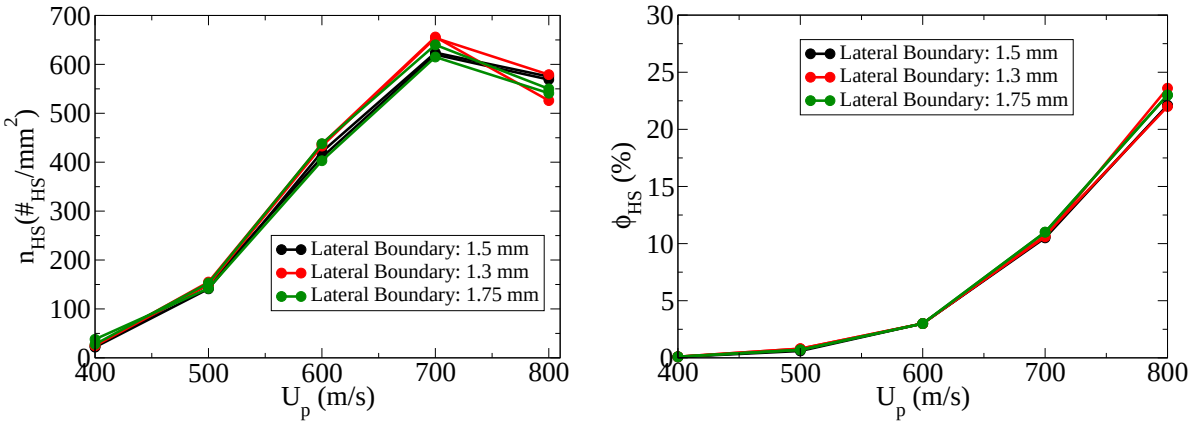

(a) (b)

Figure 6.8: Effects of lateral boundary dimensions on the overall hot-spot volumetric properties for materials with similar effective packing density $\bar{\phi}_s = 76\%$: (a) Number density n_{HS}; (b) Volume fraction ϕ_{HS}.

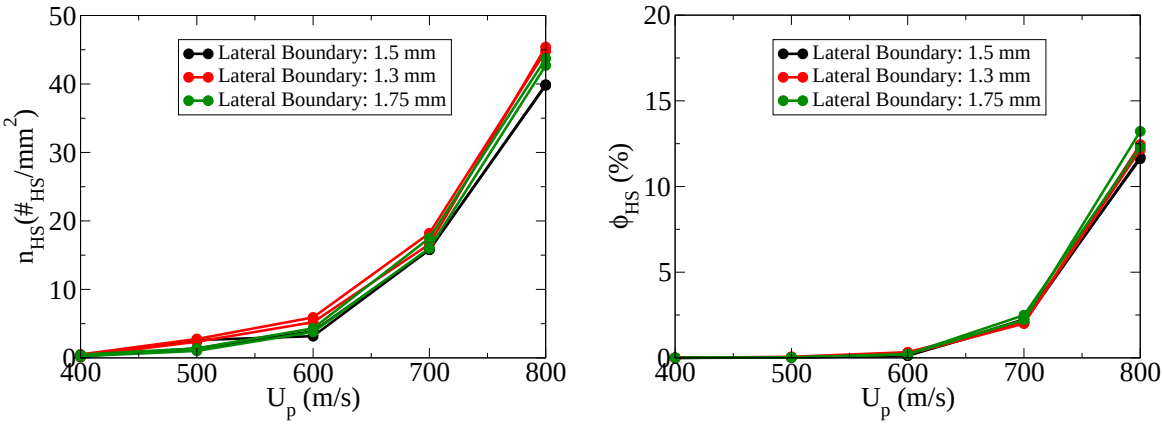

(a) (b)

Figure 6.9: Effects of lateral boundary dimensions on the critical hot-spot volumetric properties for materials with similar effective packing density $\bar{\phi}_s = 76\%$: (a) Number density n_{HS}; (b) Volume fraction ϕ_{HS}.

CHAPTER 7
CONCLUSIONS AND RECOMMENDATIONS

The main objective of this work was to characterize the effects of the initial meso-structure on deformation induced heating in granular explosives at particle scales ($O \approx 10 - 100\ \mu m$). In this study, the initial meso-structures are described by their effective packing densities $\bar{\phi}_s$, effective metal mass fractions λ_m, particle size and particle shape distributions. A 2-D, Lagrangian, combined FEM-DEM method originally formulated by Panchadhara and Gonthier [61] was extended to account for metal (Al) and explosive (HMX) mixtures with varying compositions and particle sizes. With regards to particle shapes, only minor variations were considered (Hexagonal or Circular). Emphasis was placed on characterizing how the variations in the initial meso-structures and wave strength (U_p = 400-800 m/s) affects the macro-scale wave profiles, and the hot-spot fields within the explosive component. A *Peaks over Threshold* approach was used to identify hot-spots within the material by filtering out the cooler explosive material in order to generate the hot-spot fields. The complex hot-spot fields resulted in hot-spots with varying shapes, sizes, intensity, and proximity. The distributions of these hot-spot features were described using multivariate probability density functions. Further, hot-spots that have the potential to quickly react behind the wave were identified (*critical hot-spots*), and the analysis was differentiated based on the overall hot-spot fields which can influence the hot-spot growth and coalescence rate which are important in terms of a global ignition event, and the critical hot-spot fields which are important for local ignition. Hot-spot volumetric properties such as hot-spot number density and volume fraction were obtained. The volumetric properties are important hot-spot parameters which are routinely used in the ignition and growth models to predict macro-scale shock response of explosives. Additionally, the hot-spot volumetric properties also provide information on the effective hot-spot frequency and mass flux rates induced

by the deformation waves. A preliminary methodology was outlined to estimate global ignition manifolds for various meso-structures based on the functional dependency of hot-spot mass flux on wave strength. In their current state, the ignition and growth models use ideal descriptions of hot-spot fields to estimate the detonation parameters since they do not account for the details of the meso-structures. The detailed characterization of the inert hot-spot fields from these meso-scale simulations can be used to advance the development of macro-scale ignition models. The following sections outline the specific conclusions from the relevant results chapters.

7.1 Effects of Porosity and Composition

In this chapter, the effects of porosity and composition $0 \leq \lambda_m \leq 0.2$ on both the macro-scale wave profiles, and the hot-spot fields were explored. To this end, three meso-structures with initial packing densities in the range of $0.678 \leq \bar{\phi}_s \leq 0.835$ were considered. Additionally, the macro-scale and particle scale (hot-spot) dissipation within the material were expressed as a function of the piston speed U_p, and wave pressure $\bar{P}$ since experiments routinely express the sensitivity of these materials as a function of these variables. Specific conclusions from this chapter are as follows.

7.1.1 Effective Wave Profiles

First, an increase in porosity $1 - \bar{\phi}_s$ resulted in larger dissipation within the meso-structure for a fixed U_p and/or $\bar{P}$ due to plastic pore collapse. Second, for a fixed porosity and U_p inclusion of Al enhanced the effective pressure $\bar{P}$ within the explosive component due to the high metal acoustic impedance which causes the reflection of acoustic energy at explosive-metal interfaces thereby enhancing the effective plastic work within the explosive particles. An increase in packing density and/or metal content resulted in marginally ($< 5\%$) larger wavespeeds within the material. Wave rise times which provide information on the thickness of the deformation wave were found to decrease with an increase in packing density and/or piston speed but were insensitive to variations in metal mass fraction. The predicted Hugoniots and wave rise times for neat HMX formulations agreed with experimen-

tally obtained Hugoniot curves and rise times for porous HMX with similar effective packing densities.

7.1.2 Hot-Spot Fields

For a fixed piston speed U_p, an increase in porosity was found to increase the average hot-spot size within the material due to enhanced dissipation. However, only marginal variations in hot-spot intensity were predicted due to variations in porosity, metal mass fraction or impact speed. Hot-spot area to perimeter (ζ) distributions indicate a larger number of planar hot-spots at low impact speeds $U_p < 600$ m/s, resulting from localized dissipation at the contact interfaces due to friction and/or frictionally induced plasticity. However, at high speeds $U_p \geq 600$ m/s, the hot-spots encompass larger volumes of the particle due to significant plasticity (Wave strength > Material strength). Hot-spot number density and volume fraction were found to increase behind the deformation wave with an increase in porosity and/or wave strength (U_p or $\bar{P}$). The hot-spot number density curves for all the meso-structures exhibit two regions. One associated with the hot-spot formation dominated phase which increases monotonically with an increase in piston speed or wave pressure, while the other is associated with hot-spot agglomeration phase which leads to a decrease in the hot-spot formation rates behind the deformation wave for strong waves ($U_p > 700$ m/s).

Though the effective plastic work in the explosive increased due to the inclusion of metal for the entire range of piston speeds and/or wave pressures, the overall hot-spot volumetric curves tend to exhibit a qualitatively different trend. For $U_p < 600$ m/s, the inclusion of metal leads to a decrease in hot-spot formation within the explosive due to the high thermal conductivity of the metal which absorbs most of the frictionally dissipated energy at the Al-HMX interfaces. However, for $U_p > 600$ m/s, an increase in the hot-spot number density and volume fraction are predicted due to enhanced pressures within the material. Though the hot-spot formation within the explosive component increases due to the inclusion of metal at $U_p > 600$ m/s, the average separation between the hot-spots was found to increase due to

dilution. Therefore, the inclusion of metal may delay the transition from local ignition events to a global ignition event for a given piston speed and/or wave pressure. Additionally, the metal may act as an energy sink, and restrict the rate of combustion within the materials by absorbing much of the energy released during reaction. On the contrary, if the metal begins to burn, it may enhance the combustion rates within the material due to exothermic energy release. Based on the inert meso-scale simulations, only the likelihood of global ignition within the materials can be predicted. To accurately describe the Shock to Detonation Transition (SDT) requires complex multiphase combustion analysis on the predicted hot-spot fields which is beyond the scope of this work. The variations in hot-spot number density, and volume fraction with the shock pressure/ input power were found to exhibit a power law dependency which is qualitatively similar to experimentally observed power law relations between shock pressure and time to detonation or run distance to detonation. The power-law fits indicate that though the rates of hot-spot formation increase for materials with higher packing densities, the overall hot-spot number density and volume fractions are lower than those of less dense material resulting in lower prefactor values. The critical hot-spot fields were found to be qualitatively similar to the overall hot-spot fields and therefore it is plausible to use just the overall hot-spot fields to describe the ignition response of the material.

7.1.3 Combustion Implication

The SDT of the HEs can be described as a multi-step process with the local ignition (critical hot-spot burning), and the global ignition (overall hot-spot growth and coalescence) being the preliminary steps for the transition to detonation of the material. Thermal explosion times (local ignition) were computed based on the critical hot-spot peak intensities to investigate the effects of porosity and composition on the local ignition of the material. Thermal explosion times indicate that few critical hot-spots have explosion times lower than the corresponding wave rise times suggesting that some reaction occurs quickly within the deformation wave. It is important to note that there are uncertainties associated with the

predicted hot-spot intensities since temperature independent material properties were used in this analysis. As such, the explosion times from this analysis may be quantitatively different from experimentally observed values. Packing density and composition were found to have only a marginal effect on the explosion times indicating that the material sensitivity may be strongly dependent on the overall hot-spot fields which govern the hot-spot growth and coalescence. As such, a simple methodology was outlined to estimate global ignition times/ignition manifolds based on the functional relationships between wave pressures and the overall hot-spot volumetric quantities. The ignition times were assumed to be inversely proportional to the hot-spot mass flux behind the deformation wave, and power-effluence curves were computed to provide ignition manifolds for each meso-structure. From the simple ignition analysis, few preliminary predictions were made. First, an increase in porosity leads to lower ignition times for a fixed wave pressure with much larger variations predicted at lower wave pressures. Additionally, for a fixed porosity and wave pressure, the inclusion of metal resulted in larger ignition. The predicted global ignition times have values lower than the corresponding wave rise times which indicates that for the range of piston speeds considered in this study, the energy released due to reaction is strongly coupled to the deformation wave, and therefore may further enhance the wave strength.

7.2 Effects of Particle Size

The effects of component particle size ratios ($CR = D_{Al}/D_{HMX}$) on the macro-scale wave profiles and the resulting hot-spot fields were characterized. Component size ratios in the range of $1 \leq CR \leq 6$ were considered. For all of the meso-structures considered in this chapter, the average size of the HMX particles D_{HMX} were similar and therefore the variations in CR were strictly due to the changes in the average Al (D_{Al}) particle size. Additionally, the number of large Al particles within the meso-structures were varied by altering the metal mass fractions ($0.0 \leq \lambda_m \leq 0.56$). With respect to the neat HMX meso-structures, CR refers to the size ratio between the large and small HMX particles. Meso-structure with a uniform particle size distribution and $CR = 1$ served as the baseline. Due

to the limitations of the gravity settling algorithm used to generate these meso-structure, minor variations in $\bar{\phi}_s$ ($< 2\%$) occurred between the meso-structures. Specific conclusions include the following.

7.2.1 Effective Wave Profiles

For values of $0.0 \leq \lambda_m \leq 0.2$,variations in CR were found to have a negligible effect on the effective wave end states, and most of the marginal differences in Hugoniot curves were due to the variations in the initial packing densities of these meso-structures. This observation is due to the fact that for $\lambda_m \leq 0.3$, the macro-scale compaction is primarily driven by the explosive-explosive contacts as meso-structures contain few large particles (< 2 % by number fraction). However, an increase in $\lambda_m = 0.56$ leads to an increase in the number of large particles with the material ($> 6\%$ by number fraction), and as such the macro-scale compaction dynamics is also influenced by the large particles wherein for a fixed piston speed, a monotonic increase in the effective pressure and the effective plastic work in the explosive is predicted with an increase in Al particle size.

7.2.2 Hot-Spot Fields

Al particle size and the corresponding metal mass fraction λ_m were found to affect the hot-spot fields substantially. First, for $U_p < 600$ m/s which corresponds to wave pressures below $\bar{P} < 2.5$ GPa, substantial differences in the overall hot-spot volumetric quantities were observed between the baseline metalized ($\lambda_m = 0.2$) meso-structure consisting of equally sized Al and HMX particles, and metalized meso-structures with component size ratios of $CR = 3$ and $CR = 6$ consisting of large Al particles. Though speculative at this juncture this observation is plausibly due to sensitivity of frictional dissipation to changes in granular bed morphology which arise due to the inclusion of large Al particles. However at higher impact speeds $U_p > 600$ m/s or wave pressures $\bar{P} > 2.5$ GPa, only marginal differences in the overall hot-spot volume fractions were observed between the meso-structures whereas larger differences in hot-spot number density were predicted. This observation is due to hot-spot agglomeration in the vicinity of the large Al-small HMX particle interfaces which

results in the creation of fewer hot-spots with larger area. For metalized meso-structures with a higher metal content $\lambda_m = 0.56$, the number of large Al particles increased within the meso-structure and this was found to enhance the hot-spot formation within the material due to hot-spot formation at the interface of the Al-HMX particle boundaries (impedance mismatch).

7.2.3 Material Stochasticity

Inclusion of large Al particles led to spatially non-homogeneous meso-structures due to clustering of large particles. Because, hot-spots form in the vicinity of the large Al and small HMX particle interfaces, particle clustering may affect the hot-spot fields. Hence, an additional meso-structure with $CR = 3$ and $\lambda_m = 0.2$ was considered in the analysis to investigate the effects of particle clustering on hot-spot fields. Also, the hot-spot number density and volume fraction curves exhibited a highly non-linear dependence on Al particle size especially at lower impact speeds $U_p < 600$ m/s or wave pressures ($\bar{P} < 2.5$ GPa) with larger number of hot-spots predicted in meso-structure with $CR = 1$ compared to meso-structures with $CR = 3$ or $CR = 6$. However, little differences in the hot-spot number density and volume fraction were predicted between the meso-structures with $CR = 3$ and $CR = 6$, for the entire range of piston speeds or wave pressures. Therefore, additional meso-structures with an intermediate component size ratio of $CR = 2$ were considered to investigate this potential non-linear dependency of hot-spot fields on Al particle size. Predictions indicate that spatial clustering of large particles has little effect on the qualitative or quantitative trends of hot-spot number densities and volume fraction. Additionally, the hot-spot number density and volume fraction curves for $CR = 2$ lies between that of meso-structures with $CR = 1$ and $CR = 3$ which suggests a non-linear dependency of hot-spot number densities and volume fraction on the Al particle size. The observed non-linear dependence of hot-spot fields on Al particle size especially at lower impact speeds $U_p < 600$ m/s is not clearly understood and requires additional analysis.

7.3 Effects of Meso-Structural Stochasticity

In this chapter, the variations in shock sensitivity of the material due to stochastic variations in the meso-structure were addressed. Stochastic variations in packing density and/or composition, particle sizes, and shapes can all significantly affect the shock response of the granular explosives. However, this chapter solely focused on quantifying the effects of stochastic variations in $\phi_s(x)$. To this end, ten (10) meso-structures with identical effective packing density $\bar{\phi}_s = 0.76$ but varying spatial distribution of packing density about the effective value were created by randomly seeding the explosive particles within the fixed domain. Metal mass fraction ($\lambda_m = 0.0$), particle size and shapes were identical across the meso-structures. Numerical experiments indicated that an increase in the transverse boundary width L_T resulted in larger spatial fluctuations in $\bar{\phi}_s$ due to the limitations of the pseudo-gravity settling algorithm. As such, values of L_T were varied between 1.3-1.75 mm. While stochastic variations in $\bar{\phi}_s$ had a negligible effect on Hugoniots, it was found to affect the hot-spot volumetric quantities marginally. Variations in hot-spot number density was found to increase with an increase in piston speed. On the contrary, smaller ($< 2\%$) variations in hot-spot volume fraction were predicted across the entire range of piston speed. This suggests that the observed variations in hot-spot number density are due to the formation of smaller hot-spots (4-7 FE) that form at the particle boundaries due to surface dissipation mechanisms such as friction and/or frictionally induced tractions that result in localized plasticity. Surface dissipative mechanisms are more likely to be to sensitive to stochastic variations in the meso-structure since small changes in the granular bed alters the contact mechanics significantly within the material. The nearest neighbor hot-spot distributions were found to vary significantly between the meso-structures at lower speeds $U_p < 600$ m/s, while lesser scatter was predicted at higher speeds. The critical hot-spot fields were found to exhibit similar qualitative trends as the overall hot-spot fields. The variations in the lateral boundary dimensions were found to affect the hot-spot statistics minimally.

7.4 Recommendations

As mentioned, the meso-scale model considered in this analysis uses ideal 2-D meso-structures with simplified physical model to investigate the shock sensitivity of granular explosives. Many modeling changes must be made to address shock sensitivity of explosives in further detail. The 2-D assumption can affect the results since greater stress concentration and frictional dissipation might arise in 3-D particle ensembles due to different packing arrangements. For example, for equally sized circular particles, a face centered cubic packing in 2-D results in a maximum of 6 contacts per particle, whereas 3-D spherical particles may have 12 contacts per particle plausibly leading to higher dissipation. Additionally, the predicted temperatures vary significantly within the HMX particles, and therefore it may not be appropriate to use temperature independent material properties. Incorporating temperature dependent material properties such as yield strength, and specific heat will lead to thermo-mechanical fields that are more quantitatively accurate. Brittle fracture of HMX particles has been observed in experiments when the solid explosives are subjected to impact. Fracturing of HMX particles may lead to enhanced sensitivity of the material. In their analysis of PBX, Barua et al. [8] found that fracture of HMX particles, and the subsequent frictional dissipation along the fractured surfaces was a significant heating mechanism within the explosive. Therefore, it may be necessary to include fracture within the meso-scale model. Hot-spot temperatures larger than the melting temperature of HMX were predicted in this analysis. In reality melting suppresses the hot-spot temperatures and leads to multiphase lubrication. Therefore, inclusion of melting within the model may be crucial in accurately predicting the material shock response. Most explosive formulations have small amounts of binders and oxidizers. The meso-scale model can be extended to include binder as an additional component.

REFERENCES

[1] MR Baer. Computational modeling of heterogeneous reactive materials at the mesoscale. In *AIP Conference Proceedings*, volume 505, page 27, 2000.

[2] MR Baer. Modeling heterogeneous energetic materials at the mesoscale. *Thermochimica acta*, 384(1):351–367, 2002.

[3] MR Baer, DK Gartling, and PE DesJardin. Probabilistic models for reactive behaviour in heterogeneous condensed phase media. *Combustion Theory and Modelling*, 16(1):75–106, 2012.

[4] MR Baer and JW Nunziato. A two-phase mixture theory for the deflagration-to-detonation transition (ddt) in reactive granular materials. *International journal of multiphase flow*, 12(6):861–889, 1986.

[5] SG Bardenhagen and JU Brackbill. Dynamic stress bridging in granular material. *Journal of applied physics*, 83(11):5732–5740, 1998.

[6] A Barua. Mesoscale computational prediction and quantification of thermomechanical ignition behavior of polymer-bonded explosives (pbxs). 2013.

[7] A Barua, S Kim, Y Horie, and M Zhou. Prediction of probabilistic ignition behavior of polymer-bonded explosives from microstructural stochasticity. *Journal of Applied Physics*, 113(18):184907, 2013.

[8] A Barua and M Zhou. A lagrangian framework for analyzing microstructural level response of polymer-bonded explosives. *Modelling and Simulation in Materials Science and Engineering*, 19(5):055001, 2011.

[9] JB Bdzil, R Menikoff, SF Son, AK Kapila, and DS Stewart. Two-phase modeling of deflagration-to-detonation transition in granular materials: A critical examination of modeling issues. *Physics of Fluids*, 11:378, 1999.

[10] DJ Benson and P Conley. Eulerian finite-element simulations of experimentally acquired hmx microstructures. *Modelling and Simulation in Materials Science and Engineering*, 7(3):333, 1999.

[11] DJ Benson, VF Nesterenko, and F Jonsdottir. Micromechanics of shock deformation of granular materials. In *AIP Conference Proceedings*, volume 370, page 603, 1996.

[12] JP Borg and TJ Vogler. Mesoscale calculations of the dynamic behavior of a granular ceramic. *International Journal of Solids and Structures*, 45(6):1676–1696, 2008.

[13] J Borne, J Mory, and F Schlesser. Reduced sensitivity rdx (rs-rdx) in pressed formulations: Respective effects of intra-granular pores, extra-granular pores and pore sizes. *Propellants, Explosives, Pyrotechnics*, 33(1):37–43, 2008.

[14] P Brousseau and CJ Anderson. Nanometric aluminum in explosives. *Propellants, Explosives, Pyrotechnics*, 27(5):300–306, 2002.

[15] PB Butler and H Krier. Analysis of deflagration to shock to detonation transition (dsdt) in porous energetic solid propellants. In *Proceedings of AGARD Conference on Energetic Propellants, Lisse, The Netherlands*, volume 367, pages 5–10, 1984.

[16] Françoise Chaitin-Chatelin and Valérie Frayssé. *Lectures on finite precision computations*, volume 1. Siam, 1996.

[17] Sunada Chakravarthy, Keith A Gonthier, and Rohan Panchadhara. Analysis of mesoscale heating by piston supported waves in granular metalized explosive. *Modelling and Simulation in Materials Science and Engineering*, 21(5):055016, 2013.

[18] MM Chaudhri. Stab initiation of explosions. *Nature*, pages 121–122, 1976.

[19] MC Chick. The effect of interstitial gas on the shock sensitivity of low density explosive compacts. In *Proceedings of the 4th Symposium (International) on Detonation, US Naval Ordnance Laboratory, Maryland*, pages 349–358, 1965.

[20] SG Cochran. Statistical treatment of heterogeneous chemical reaction in shock-initiated explosives. Technical report, California Univ., Livermore (USA). Lawrence Livermore Lab., 1980.

[21] PA Conley and DJ Benson. An estimate of the linear strain rate dependence of octahydro-1, 3, 5, 7-tetranitro-1, 3, 5, 7-tetrazocine. *Journal of Applied Physics*, 86(12):6717–6728, 1999.

[22] JI Copp and SE Napier. The sensitiveness of explosives. *Philosophical Transactions of the Royal Society*, 241:198–296, 1948.

[23] MW Crochet and KA Gonthier. A riemann problem solution methodology for a class of evolutionary mixture equations with an arbitrary number of components. *Applied Numerical Mathematics*, 76:145–165, 2014.

[24] H Czerski and WG Proud. Relationship between the morphology of granular cyclotrimethylene-trinitramine and its shock sensitivity. *Journal of Applied Physics*, 102(11):113515–113515, 2007.

[25] JJ Dick. Measurement of the shock initiation sensitivity of low density hmx. *Combustion and Flame*, 54(1):121–129, 1983.

[26] JK Dienes. Frictional hot spots and propellant sensitivity. In *Proceedings of Materials Research Society Symposium*, pages 373–383. Cambridge Univ Press, 1984.

[27] IPH Do and DJ Benson. Micromechanical modeling of shock-induced chemical reactions in heterogeneous multi-material powder mixtures. *International Journal of Plasticity*, 17(4):641–668, 2001.

[28] JE Field, NK Bourne, SJP Palmer, SM Walley, J Sharma, and BC Beard. Hot-spot ignition mechanisms for explosives and propellants [and discussion]. *Philosophical Transactions of the Royal Society of London. Series A: Physical and Engineering Sciences*, 339(1654):269–283, 1992.

[29] RB Frey. The initiation of explosive charges by rapid shear. Technical report, DTIC Document, 1980.

[30] J Gilbert. Characterizing impact induced hot-spot morphology in granular solid explosive. *Master of Science Thesis, Louisiana State University, Baton Rouge*, 2012.

[31] J Gilbert, S Chakravarthy, and KA Gonthier. Computational analysis of hot-spot formation by quasi-steady deformation waves in porous explosive. *Journal of Applied Physics*, 113(19):194901–194901, 2013.

[32] MF Gogulya, MN Makhov, A Yu Dolgoborodov, MA Brazhnikov, VI Arkhipov, and VG Shchetinin. Mechanical sensitivity and detonation parameters of aluminized explosives. *Combustion, Explosion and Shock Waves*, 40(4):445–457, 2004.

[33] KA Gonthier. Modeling and analysis of reactive compaction for granular energetic solids. *Combustion Science and Technology*, 175(9):1679–1709, 2003.

[34] KA Gonthier and CG Rumchik. *Technical Report ME-TSI-09*, 2007.

[35] DE Grady and ME Kipp. The growth of inhomogeneous thermoplastic shear. *Le Journal de Physique Colloques*, 46(C5):C5–291, 1985.

[36] RL Gustavsen, SA Sheffield, and RR Alcon. Low pressure shock initiation of porous hmx for two grain size distributions and two densities. In *AIP Conference Proceedings*, volume 370, page 851, 1996.

[37] Bryan F Henson, Blaine W Asay, Laura B Smilowitz, and Peter Dickson. Ignition chemistry in hmx from thermal explosion to detonation. In *AIP CONFERENCE PROCEEDINGS*, number 2, pages 1069–1072. IOP INSTITUTE OF PHYSICS PUBLISHING LTD, 2002.

[38] Y Horie and Y Hamate. A new approach to the reactive burn modeling of heterogeneous explosives. In *Materials Science Forum*, volume 465, pages 1–12. Trans Tech Publ, 2004.

[39] Y Horie, Y Hamate, D Greening, and T Dey. Reactive burn modeling of solid explosives with a statistical treatment of hot spots in two spatial dimensions. In *American Institute of Physics Conference Series*, volume 706, pages 989–992, 2004.

[40] Kenneth Langstreth Johnson and Kenneth Langstreth Johnson. *Contact mechanics*. Cambridge university press, 1987.

[41] J Kang, PB Butler, and MR Baer. A thermomechanical analysis of hot spot formation in condensed-phase, energetic materials. *Combustion and flame*, 89(2):117–139, 1992.

[42] RJ Karpowicz and TB Brill. The beta to delta transformation of hmx-its thermal analysis and relationship to propellants. *AIAA Journal*, 20(11):1586–1591, 1982.

[43] BA Khasainov, AA Borisov, BS Ermolaev, and AI Korotkov. Two-phase visco-plastic model of shock initiation of detonation in high density pressed explosives. In *7th Symposium (International) on Detonation, Annapolis, MD*, pages 435–447, 1981.

[44] ME Kipp. Modeling granular explosive detonations with shear band concepts. Technical report, Sandia National Labs., Albuquerque, NM (USA), 1985.

[45] DR Kumar, RK Kumar, and PK Philip. Simulation of dynamic compaction of metal powders. *Journal of applied physics*, 85(2):767–775, 1999.

[46] EL Lee and CM Tarver. Phenomenological model of shock initiation in heterogeneous explosives. *Physics of Fluids*, 23:2362, 1980.

[47] A Lefrancois, G Baudin, C Le Gallic, P Boyce, and JP Coudoing. Nanometric aluminum powder influence on the detonation efficiency of explosives. In *Proceedings of the 12th International Detonation Symposium*, pages 22–32, 2002.

[48] LD Libersky, AG Petschek, and PA Peterson. Calculation of reactive flow using smoothed particle hydrodynamics. In *Tenth Symposium (International) on Detonation*, pages 33395–12, 1993.

[49] CL Mader. Initiation of detonation by the interaction of shocks with density discontinuities. *Physics of Fluids*, 8:1811, 1965.

[50] CL Mader. Two dimensional homogeneous and heterogeneous detonation wave propagation. Technical report, Los Alamos Scientific Lab., N. Mex.(USA), 1976.

[51] SP Marsh. *Lasl Shock Hungoniot Data*, volume 5. University of California Pr, 1980.

[52] J Massoni, R Saurel, G Baudin, and G Demol. A mechanistic model for shock initiation of solid explosives. *Physics of Fluids*, 11:710, 1999.

[53] JM McAfee, B Asay, AW Campbell, and JB Ramsay. The deflagration-to-detonation transition in granular hmx. Technical report, Los Alamos National Lab., NM (USA), 1991.

[54] R Menikoff. Pore collapse and hot spots in hmx. In *AIP Conference Proceedings*, volume 706, pages 393–397, 2004.

[55] R Menikoff and MS Shaw. The surf model and the curvature effect for pbx 9502. *Combustion Theory and Modelling*, 16(6):1140–1169, 2012.

[56] Joe J Monaghan. Smoothed particle hydrodynamics. *Annual review of astronomy and astrophysics*, 30:543–574, 1992.

[57] H Moulard. Particular aspect of the explosive particle size effect on shock sensitivity of cast pbx formulations. In *Ninth Symposium (International) on Detonation*, pages 113291–7, 1989.

[58] A Munjiza and KRF Andrews. Penalty function method for combined finite-discrete element systems comprising large number of separate bodies. *International Journal for Numerical Methods in Engineering*, 49(11):1377–1396, 2000.

[59] A.A. Munjiza. *The Combined Finite-Discrete Element Method*. Wiley, 2004.

[60] Albert L Nichols III and Craig M Tarver. A statistical hot spot reactive flow model for shock initiation and detonation of solid high explosives. In *Twelfth International Symposium on Detonation, Office of Naval Research, San Diego, CA*, 2002.

[61] R Panchadhara. Meso-scale heating predictions for weak impact of granular energetic solids. *PhD Disseration, Louisiana State University, Baton Rouge, LA*, 2009.

[62] R Panchadhara and KA Gonthier. Mesoscale analysis of volumetric and surface dissipation in granular explosive induced by uniaxial deformation waves. *Shock Waves*, 21(1):43–61, 2011.

[63] Per-Olof Persson and Gilbert Strang. A simple mesh generator in matlab. *SIAM review*, 46(2):329–345, 2004.

[64] D Price. Effect of particle size on the shock sensitivity of porous he. *Journal of energetic materials*, 6(3-4):283–317, 1988.

[65] D Price and AR Clairmont. Deflagration to detonation transition behavior of aluminized hmx. *Propellants, Explosives, Pyrotechnics*, 4(6):132–136, 1979.

[66] CL Scott. Effect of particle size on shock initiation of petn, rdx, and tetryl. In *Proceedings of the Fifth Symposium (International) on Detonation*, page 259, 1970.

[67] LB Seely. A proposed mechanism for shock initiation of low-density granular explosives. Technical report, Los Alamos Scientific Lab., N. Mex., 1963.

[68] WL Seitz. Short-duration shock initiation of triaminotrinitribenzene (tatb). In *Proceedings of the American Physical Society, Topical Conference, Santa Fe, NM*, volume 18, page 531, 1983.

[69] J-M Senoner, Marta García, Simon Mendez, Gabriel Staffelbach, Olivier Vermorel, and Thierry Poinsot. Growth of rounding errors and repetitivity of large eddy simulations. *AIAA journal*, 46(7):1773–1781, 2008.

[70] RE Setchell. Grain-size effects on the shock sensitivity of hexanitrostilbene (hns) explosive. *Combustion and flame*, 56(3):343–345, 1984.

[71] SA Sheffield, RL Gustavsen, RR Alcon, RA Graham, and MU Anderson. Shock initiation studies of low density hmx using electromagnetic particle velocity and pvdf stress gauges. Technical report, Los Alamos National Lab., NM (United States), 1993.

[72] SA Sheffield, RL Gustavsen, and MU Anderson. Shock loading of porous high explosives. In *High-Pressure Shock Compression of Solids IV*, pages 23–61. Springer, 1997.

[73] X Song, Yi Wang, C An, X Guo, and F Li. Dependence of particle morphology and size on the mechanical sensitivity and thermal stability of octahydro-1, 3, 5, 7-tetranitro-1, 3, 5, 7-tetrazocine. *journal of hazardous materials*, 159(2):222–229, 2008.

[74] Josef Stoer and Roland Bulirsch. *Introduction to numerical analysis*. Springer, 1993.

[75] CM Tarver, SK Chidester, and AL Nichols. Critical conditions for impact-and shock-induced hot spots in solid explosives. *The Journal of Physical Chemistry*, 100(14):5794–5799, 1996.

[76] BC Taylor and LW Ervin. Separation of ignition and buildup to detonation in pressed tnt. In *Proceedings Sixth Symposium (International) on Detonation*, pages 3–10, 1976.

[77] VA Teselkin. Influence of the particle size of the components on the mechanical sensitivity of metallized high explosives. *Russian Journal of Physical Chemistry B, Focus on Physics*, 2(4):609–618, 2008.

[78] S Torquato. *Random heterogeneous materials: microstructure and macroscopic properties*, volume 16. Springer, 2002.

[79] RE Winter and JE Field. The role of localized plastic flow in the impact initiation of explosives. *Proceedings of the Royal Society of London. A. Mathematical and Physical Sciences*, 343(1634):399–413, 1975.

[80] F Zhang. Detonation of metalized composite explosives. In *Shock Wave Science and Technology Reference Library, Vol. 4*, pages 217–286. Springer, 2009.

APPENDIX

Best fit parameters for relevant Hugoniots and overall hot-spot volumetric curves for meso-structures considered in this study.

Table A.1: Parameter values for linear curve fits for D in m/s as a function of U_p in m/s for meso-structures A-C.

Meso-Structure	$D = c_1 U_p + c_2$
A ($\phi_s = 67.8\%$)	
Metalized HMX	c_1=2.28, c_2=296.03
Neat HMX	c_1=2.11, c_2=380.72
B ($\phi_s = 76.0\%$)	
Metalized HMX	c_1=2.24, c_2=683.96
Neat HMX	c_1=2.12, c_2 =715.22
C ($\phi_s = 83.5\%$)	
Metalized HMX	c_1= 2.10, c_2=1126.8
Neat HMX	c_1=1.94, c_2=1150.4

Table A.2: Parameter values for quadratic curve fits for $\bar{P}$ in GPa as a function of U_p in m/s for meso-structures A-C.

Meso-Structure	$P = c_1 U_p^2 + c_2 U_p + c_3$
A ($\phi_s = 67.8\%$)	
Metalized HMX	c_1=1.5×10^{-6}, $c_2 = 0.002$, $c_3 = -0.416$
Neat HMX	c_1=1.76×10^{-6}, $c_2 = 0.0015$, $c_3 = -0.362$
B ($\phi_s = 76.0\%$)	
Metalized HMX	c_1=1.35×10^{-6}, $c_2 = 0.0034$, $c_3 = -0.690$
Neat HMX	c_1=1.64×10^{-6}, $c_2 = 0.0027$, $c_3 = -0.5543$
C ($\phi_s = 83.5\%$)	
Metalized HMX	c_1=1.92×10^{-6}, $c_2 = 0.003$, $c_3 = -0.6629$
Neat HMX	c_1=1.21×10^{-6}, $c_2 = 0.0039$, $c_3 = -0.6700$

Table A.3: Parameter values for power law fits for effective plastic work $\bar{W}_{pe}$ in KJ/kg as a function of effective wave pressure $\bar{P}$ in GPa for meso-structures A-C.

Meso-Structure	$\bar{W}_{pe} = c\bar{P}^m$
A ($\phi_s = 67.8\%$)	
Metalized HMX	m=1.10, c=121.04
Neat HMX	m=1.03, c=116.76
B ($\phi_s = 76.0\%$)	
Metalized HMX	m=1.10, c=73.04
Neat HMX	m=0.9811, c =77
C ($\phi_s = 83.5\%$)	
Metalized HMX	m= 1.09, c=49
Neat HMX	m=1.07, c=48.9

Table A.4: Parameter values for power law fits between overall hot-spot volumetric properties as a function of effective wave pressure $\bar{P}$ in GPa for meso-structures A-C.

Meso-Structure	$n_{HS} = c\bar{P}^m$	$\phi_{HS} = c\bar{P}^m$
A ($\phi_s = 67.8\%$)		
Metalized HMX	m=1.26, c=478.24	m=2.78, c=3.59
Neat HMX	m=1.09, c=575.45	m=2.56, c=4.54
B ($\phi_s = 76.0\%$)		
Metalized HMX	m=1.77, c=223.59	m=3.62, c=0.75
Neat HMX	m=1.65, c =301.92	m=3.16, c=1.22
C ($\phi_s = 83.5\%$)		
Metalized HMX	m=2.31, c=61.43	m=3.96, c=0.09
Neat HMX	m=1.99, c=88.87	m=3.82, c=0.12

Table A.5: Parameter values for linear curve fits for D in m/s as a function of U_p in m/s for meso-structures EM 1-EM 6.

Meso-Structure	$D = c_1 U_p + c_2$
EM 1 ($\phi_s = 83.7\%$)	
Metalized HMX	c_1=2.001, c_2=1170.1
Neat HMX	c_1=1.9217, c_2=1172.1
EM 2 ($\phi_s = 83.0\%$)	
Metalized HMX	c_1=2.117, c_2=1136.7
Neat HMX	c_1=1.96, c_2 =1179.2
EM 3 ($\phi_s = 83.5\%$)	
Metalized HMX	c_1= 2.10, c_2=1126.8
Neat HMX	c_1=1.94, c_2=1150.4
EM 4 ($\phi_s = 84.6\%$)	
Metalized HMX	c_1=2.5, c_2=1125.9
Neat HMX	c_1=1.98, c_2=1203.2
EM 5 ($\bar{\phi}_s = 85.9\%$)	
Metalized HMX	c_1=2.33, c_2=1209.2
Neat HMX	c_1=1.99, c_2=1226.6
EM 6 ($\phi_s = 83.5\%$)	
Metalized HMX	c_1=2.35, c_2=1148.7
Neat HMX	c_1=1.94, c_2=1150.4

Table A.6: Parameter values for quadratic curve fits for $\bar{P}$ in GPa as a function of U_p in m/s for meso-structures EM 1- EM 6.

Meso-Structure	$P = c_1 U_p^2 + c_2 U_p + c_3$
EM 1 ($\phi_s = 83.7\%$)	
Metalized HMX	c_1=3.21×10^{-6}, $c_2 = 0.002$, $c_3 = -0.150$
Neat HMX	c_1=1.83×10^{-6}, $c_2 = 0.003$, $c_3 = -0.48$
EM 2 ($\phi_s = 83.0\%$)	
Metalized HMX	c_1=2.65×10^{-6}, $c_2 = 0.002$, $c_3 = -0.122$
Neat HMX	c_1=3.37×10^{-6}, $c_2 = 0.0007$, $c_3 = -0.196$
EM 3 ($\phi_s = 83.5\%$)	
Metalized HMX	c_1=1.92×10^{-6}, $c_2 = 0.003$, $c_3 = -0.6629$
Neat HMX	c_1=1.21×10^{-6}, $c_2 = 0.0039$, $c_3 = -0.6700$
EM 4 ($\phi_s = 84.6\%$)	
Metalized HMX	c_1=4.14×10^{-6}, $c_2 = 0.003$, $c_3 = -0.365$
Neat HMX	c_1=4.2×10^{-7}, $c_2 = 0.005$, $c_3 = -0.859$
EM 5 ($\phi_s = 85.9\%$)	
Metalized HMX	c_1=2.57×10^{-6}, $c_2 = 0.0055$, $c_3 = -0.937$
Neat HMX	c_1=-2.38×10^{-6}, $c_2 = 0.0056$, $c_3 = -0.9635$
EM 6 ($\phi_s = 83.5\%$)	
Metalized HMX	c_1=2.57×10^{-6}, $c_2 = 0.004$, $c_3 = -0.9500$
Neat HMX	c_1=1.21×10^{-6}, $c_2 = 0.0039$, $c_3 = -0.6700$

Table A.7: Parameter values for power law fits for effective plastic work $\bar{W}_{pe}$ in KJ/kg as a function of effective wave pressure $\bar{P}$ in GPa for meso-structures EM 1-EM 6.

Meso-Structure	$\bar{W}_{pe} = c\bar{P}^m$
EM 1 ($\phi_s = 83.7\%$)	
Metalized HMX	m=1.06, c=52.3
Neat HMX	m=1.11, c=45.52
EM 2 ($\phi_s = 83.0\%$)	
Metalized HMX	m=1.14, c=48.16
Neat HMX	m=1.07, c =51.09
EM 3 ($\phi_s = 83.5\%$)	
Metalized HMX	m= 1.09, c=49.61
Neat HMX	m=1.08, c=47.54
EM 4 ($\phi_s = 84.6\%$)	
Metalized HMX	m= 1.03, c=55.9
Neat HMX	m=1.08, c=43.55
EM 5 ($\phi_s = 85.9\%$)	
Metalized HMX	m= 1.02, c=55.45
Neat HMX	m=1.10, c=38.65
EM 6 ($\phi_s = 83.5\%$)	
Metalized HMX	m=1.12, c=43.55
Neat HMX	m=1.08, c=47.54

Table A.8: Parameter values for non-linear power law fits for overall hot-spot volumetric properties as a function of effective wave pressure $\bar{P}$ in GPa for meso-structures EM 1-EM 6. Note: Meso-structures EM3, EM 6 , EM 4 (Neat) and EM 5 (Neat) exhibit linear variations in the hot-spot volumetric properties with $\bar{P}$.

Meso-Structure	$n_{HS} = 10^{(a\log(P)^2+b\log(P)+c)}$	$\phi_{HS} = 10^{(a\log(P)^2+b\log(P)+c)}$
EM 1 ($\phi_s = 83.7\%$)		
Metalized HMX	a=-8.14, b =10.32, c=-0.64	a=-5.52, b=10.30, c=-2.81
Neat HMX	a=-10.21, b=12.96 , c=-1.42	a=-10.64, b=15.62, c=-4.20
EM 2 ($\phi_s = 83.0\%$)		
Metalized HMX	a=-15.52, b=17.04, c=-2.13	a=-8.74, b=13.63, c=-3.62
Neat HMX	a=-7.50, b=9.90, c =-0.53	a=-3.82, b=8.67, c=-2.42
EM 3 ($\phi_s = 83.5\%$)		
Metalized HMX (Linear)	m=2.31, c=61.43	m=3.96, c=0.09
Neat HMX (Linear)	m=1.99, c=88.87	m=3.89, c=0.12
EM 4 ($\phi_s = 84.6\%$)		
Metalized HMX	a=-7.19, b=9.02, c=-0.13	a=-5.98, b=9.30, c=-2.06
Neat HMX (Linear)	m=4.64, c=1.61	m=5.49, c=0.01
EM 5 ($\phi_s = 85.9\%$)		
Metalized HMX	a=-3.09, b=5.77, c=0.28	a=-3.81, b=7.72, c=-2.00
Neat HMX (Linear)	m=3.77, c =2.95	m=5.05, c=0.01
EM 6 ($\phi_s = 83.5\%$)		
Metalized HMX (Linear)	m=2.93, c=22.96	m=4.53, c=0.04
Neat HMX (Linear)	m=1.99, c=88.87	m=3.82, c=0.12

VITA

Sunada SN Chakravarthy is from the city of Bengaluru, in India. He completed his Bachelor of Engineering degree in mechanical engineering from Visveswaraya Technological University in 2007. In Fall 2007, he enrolled as a graduate student in the department of mechanical engineering at Louisiana State University. He is a candidate for the Ph.D degree in Mechanical Engineering to be awarded in August 2014. After graduation, he plans to work in industry.